Search for Invisible Neutron Decay in the SNO+ Water Phase

By

Morgan Andrew David Askins

Dissertation

Submitted in partial satisfaction of the requirements for the degree of

Doctor of Philosophy

in

Physics
with an Emphasis on Nuclear Science

in the

Office of Graduate Studies

of the

University of California

Davis

Approved:

Robert Svoboda, Chair

S. Mani Tripathi

Emilija Pantic

Committee in Charge

2018

Abstract

Search for Invisible Neutron Decay in the SNO+ Water Phase

Baryon number violation is an important observation needed to be made in order to understand the apparent asymmetry between baryons and anti-baryons in the universe. This dissertation sets a limit on the invisible decay of the neutron to three leptons using the SNO+ water phase data as a means to constrain one of the many possible solutions to this problem. The data set contains 11.068 live days of unblinded data, and is used to set a partial lifetime for the neutron of 1.05×10^{29} years at 90% C.L. using a profile likelihood fit to the signal and background. Systematic errors from data cleaning, reconstruction, and side-band analysis are accounted for when performing the fit. The ultimate physics goal of SNO+ is to search for neutrinoless double beta decay through the decay of ^{130}Te to determine the nature of neutrino mass. To reach this goal, SNO+ must be filled with liquid scintillator, which is distilled on site, and is doped with ^{130}Te. To progress towards this final phase of SNO+, a Bismuth-Polonium α/β coincidence counter (Scout) was built to assess the cleanliness of the distillate for Uranium and Thorium content.

Acknowledgments

Completing a dissertation is a significant time investment which is only made possible through the sound advice and continual support of those around me.

First and foremost I would like to thank my advisor, Robert Svoboda, for allowing me to work on this project and providing copious support and advice along the way. Much of the knowledge I have gained along the way is thanks to the wisdom of both Marc Bergevin and Christopher Grant, both of whom were post-docs while I was working on my dissertation.

I would also like to thank the scientists from Lawrence Livermore National Laboratory for the opportunity to work on the Watchman / Watchboy project where I was able to get hands on experience with detector electronics. I would especially like to thank Steven Dazeley and Nathaniel Bowden with whom I worked with in building the Watchboy detector.

For a large scale like SNO+, every aspect of the experiment is a group effort involving many individuals. Without the constant push forwards by every member of the collaboration this project would never have completed. I would like to give special thanks to the scintillator commissioning team—Mark Hodak, Steven Back, and Paul LaRochelle—who helped make my stay in Sudbury pleasant and productive.

Finally, I would like to thank all of my friends and family which helped me every step of the way.

Contents

List of Figures

List of Tables

Chapter 1

Physics Beyond the Standard Model

At the center of modern particle physics is the Standard Model, which has strong predictive capabilities and a satisfying mathematical model, but has some deficiencies which can only be fulfilled with a more complete theory in which the Standard Model is a suitable low energy approximation. This ranges from explaining phenomenon such as neutrino oscillations, which requires a neutrino mass mechanism to be present, to understanding the large differences in interaction strengths between the fundamental forces—known as the hierarchy problem [28]. The Standard Model itself does not explain the existence of particle quantum numbers and contains at least 19 arbitrary parameters—many of which are particle masses [29]. The observation of three families of particles in both the hadronic and leptonic sector also presents a mystery without a direct solution—known as the family problem. For these reasons alone, there are many extensions and theoretical replacements to the Standard Model proposed which seek to answer these remaining questions. There is however a catch to formulating a new theory or extending the current model, which comes in the form of new interactions and symmetries. Supersymmetry for example presents a scenario in which fine tuning is reduced through the introduction of many new particles at higher energy scales. With the introduction of new fermions and gauge bosons, new interaction channels become theoretically possible though suppressed at the energy scales of current experiments. The following chapter provides an overview of the Standard Model as well as mechanisms by which the Standard Model can be extended to produce new phenomena, namely proton decay and Majorana neutrinos.

1.1 The Standard Model

The Standard Model of particle physics, as a mathematical framework, describes the interaction between particles and three of the four fundamental forces. These three forces are the weak nuclear force, the strong nuclear force, and the electromagnetic force. Gravity is not explained by the Standard Model, and its inclusion into a consistent quantum theory is an entire field of research on its own. The Standard Model is a quantized gauge field theory which is Lorentz invariant, renormalizable, and is comprised of the direct product of the group which describes quantum chromodynamics SU(3) and that which describes the electroweak interaction SU(2) × U(1) [30].

1.1.1 Fermions, Gauge Bosons, and the Higgs Mechanism

Without modification, the Standard Model can be described using the Lagrangian density, shown in equation 1.1, which contains all possible dimension 4, renormalizable operators.

$$\mathcal{L} = i\bar{\psi}_i\bar{\sigma}^\mu D_\mu\psi_i - \frac{1}{4}F^a_{\mu\nu}F^{a\mu\nu} + \lambda^{ij}\psi_i\psi_j\Phi^{(c)} + h.c. + |D_\mu\Phi|^2 - V(\Phi) \tag{1.1}$$

The convention taken is summing over (i, j) generations of fermions and summing over (μ, ν) space-time variables. The first term, $i\bar{\psi}_i\bar{\sigma}^\mu D_\mu\psi_i$, describes how fermions (ψ) interact with the gauge boson fields through the covariant derivative (D_μ). The second term, $\frac{1}{4}F^a_{\mu\nu}F^{a\mu\nu}$, describes the propagation and self-interaction of gauge bosons (a) for each gauge field $F_{\mu\nu}$. The third term, $\lambda^{ij}\psi_i\psi_j\Phi^{(c)} + h.c.$, couples fermions with the Higgs field Φ to provide mass to the fermions. The addition of the Hermitian conjugate mirrors this process to anti-fermions. The fourth term, $|D_\mu\Phi|^2$, couples the Higgs field with other gauge bosons, which in the Standard Model provides mass to the $W^\pm$ and Z bosons. The final term, $V(\Phi)$, is the Higgs potential providing mass to the Higgs boson as well as leading to spontaneous symmetry breaking. The requirement of a renormalizable theory guarantees that the theory remains consistent at various energy scales. This is important to have because otherwise there is a cutoff energy Λ at which normally calculable quantities—such as scattering amplitudes—diverge. As will be discussed in later sections, this condition may be relaxed by assuming that the theory is actually an effective field theory, which must produce new physics prior to Λ [31]. The Standard Model is built on the local gauge

symmetry group,

$$\mathrm{SU}(3)_C \times \mathrm{SU}(2)_L \times \mathrm{U}(1)_Y, \tag{1.2}$$

where C, L, and Y denote color, left-handed chirality, and the weak hypercharge respectively [32].

1.1.1.1 Bosons

$\mathrm{SU}(3)_C$ contains the field strength tensor $\boldsymbol{G}_{\mu\nu}$ which gives rise to 8 gluons, the mediators of the strong interaction. $\mathrm{SU}(2)_L$ and $\mathrm{U}(1)_Y$ contain the W^a_μ (a=1,2,3) and B_μ gauge bosons respectively, which through the Higgs mechanism give rise to the $W^\pm$, Z^0, and γ bosons [33]. The production and interactions of these fields with one another are given by their field strength tensors in equation 1.1,

$$-\frac{1}{4}F^a_{\mu\nu}F^{a\mu\nu} = -\frac{1}{4}B_{\mu\nu}B^{\mu\nu} - \frac{1}{8}tr(\boldsymbol{W}_{\mu\nu}\boldsymbol{W}^{\mu\nu}) - \frac{1}{2}tr(\boldsymbol{G}_{\mu\nu}\boldsymbol{G}^{\mu\nu}) \tag{1.3}$$

The field strength tensor, as the name implies, describes the strength of the fields in spacetime through the covariant derivative of the vector potential. For example, in classical electromagnetism the field strength tensor is defined as

$$F_{\mu\nu} = \begin{bmatrix} 0 & -E_x/c & -E_y/c & -E_z/c \\ E_x/c & 0 & -B_z & B_y \\ E_y/c & B_z & 0 & -B_x \\ E_z/c & -B_y & B_x & 0 \end{bmatrix} \tag{1.4}$$

which is related to the vector potential by

$$F_{\mu\nu} = \partial_\mu A_\nu - \partial_\nu A_\mu + ig[A_\mu, A_\nu], \tag{1.5}$$

where in a gauge group where the vector potentials commute (Abelian), the third term vanishes. The physical $W^\pm$ and Z^0 are massive vector fields which are related to the gauge fields through the weak mixing angle—also called the Weinberg angle.

$$\begin{aligned} Z_\mu(x) &= W^3_\mu(x)\cos\theta_w - B_\mu(x)\sin\theta_w, \\ A_\mu(x) &= W^3_\mu(x)\sin\theta_w + B_\mu(x)\cos\theta_w, \\ W^+_\mu(x) &= \frac{W^1_\mu(x) + iW^2_\mu(x)}{\sqrt{2}}, \\ W^-_\mu(x) &= \frac{W^1_\mu(x) - iW^2_\mu(x)}{\sqrt{2}}, \end{aligned} \tag{1.6}$$

where A_μ is the vector potential of the electromagnetic force, giving rise to the photon. The weak mixing angle gives rise to a measurable mass ratio between the $W^\pm$ and Z boson [30],

$$\frac{M_W^2}{M_Z^2} = \cos^2\theta_w \approx 0.77 \tag{1.7}$$

Finally there is the scalar boson (Higgs), which through the spontaneous symmetry breaking of $SU(2) \times U(1)$, allows for gauge boson and fermion masses in the theory.

1.1.1.2 Fermions

Due to the work of Glashow, Weinberg, Salam, and Ward [34] [35] [36], the fundamental fermions can be introduced in a way that satisfies their known interaction with the gauge bosons. The fermion fields are broken into separate left-handed and right-handed chiral components, of which the left-handed components couple with the weak interaction as SU(2) doublets, and the right-handed components are SU(2) singlets [32]. The result is a theory of the weak interaction in which only left-handed fermion states interact with the SU(2) gauge bosons. The fermion states are defined as [33],

$$\begin{pmatrix}\nu_e \\ e^-\end{pmatrix}_L, e_R^-, \begin{pmatrix}u \\ d\end{pmatrix}_L, u_R, d_R \tag{1.8}$$

Notably there is no right-handed state for the neutrino, which would be sterile under the gauge groups of the Standard Model—ν_R has no color, no weak isospin, and is chargeless. The fundamental particle interactions are described in the Standard Model Lagrangian (1.1) through the dynamical term,

$$i\bar{\psi}_i\bar{\sigma}^\mu D_\mu\psi_i, \tag{1.9}$$

where ψ_i are the appropriate fermion fields summing over the i generations. All of the known fundamental fermions and gauge bosons (including the Higgs boson) are shown in figure 1.1.

1.1.1.3 The Higgs Mechanism

Under the Standard Model, mass terms of the form $\bar{\psi}\psi$ are forbidden in order to preserve gauge invariance. This comes from the representation of the left and right handed states

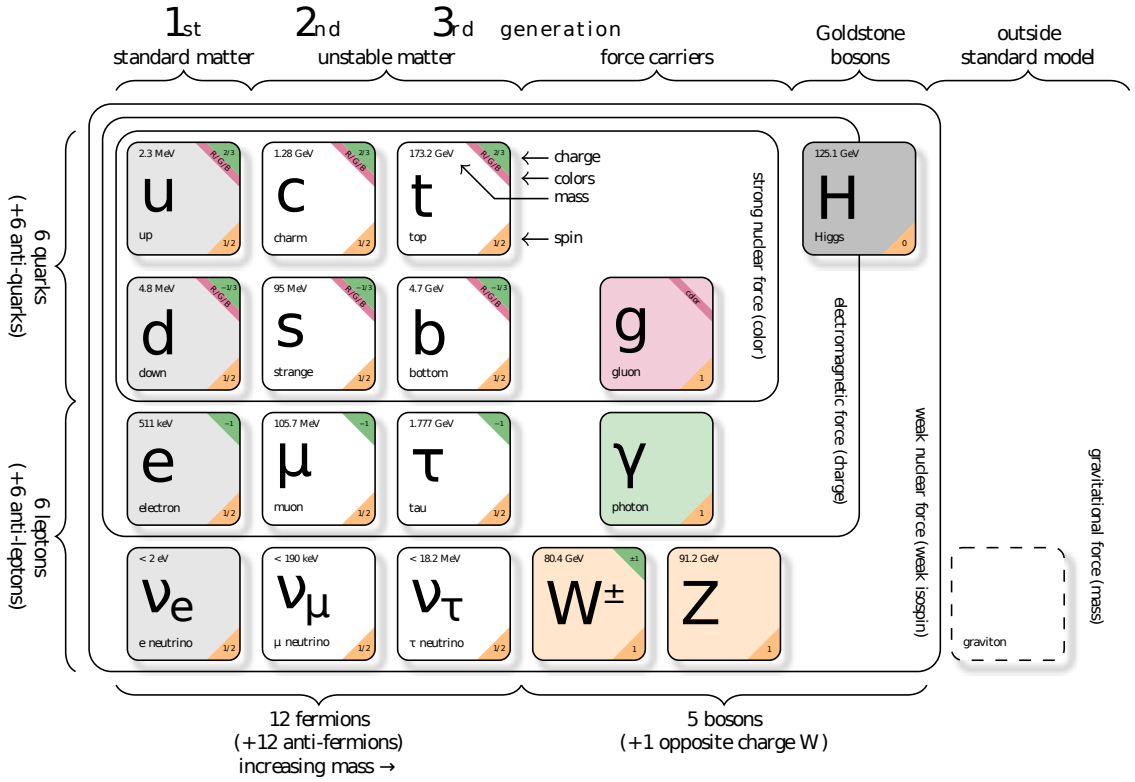

Figure 1.1: Overview of the Standard Model particles including the three generations of fermions, the gauge bosons, and the Higgs boson [1].

which transform differently under SU(2), namely that of left-handed SU(2) doublets and right-handed SU(2) singlets [32]. Thus,

$$\bar{\psi}\psi = \bar{\psi}_L\psi_R + \bar{\psi}_R\psi_L \tag{1.10}$$

is not gauge invariant. Experimental evidence has shown that the fermions, the $W^{\pm}$, and Z^0 bosons have mass, so a new mechanism was introduced by Englert, Brout, Higgs, Guralnik, Hagen, and Kibble [37] [38] [39], which introduces a scalar spin-0 field that transforms as an SU(2) doublet,

$$\Phi(x) = \begin{pmatrix} \phi^+(x) \\ \phi^0(x) \end{pmatrix} \tag{1.11}$$

where $\phi^+(x)$ is a charged complex scalar field and $\phi^0(x)$ is a neutral complex scalar field. The benefit of adding such a field to the Lagrangian is that, unlike a nonzero spin

vector field or fermion, a spin-zero field can have a nonzero value in the vacuum and still be invariant under spatial rotation. This value is called the *vacuum expectation value*, denoted $\langle\Phi\rangle$. Since the vacuum is chargeless, then ϕ^+ must be zero in the vacuum state giving us [32]

$$\langle\Phi\rangle = \frac{1}{\sqrt{2}}\begin{pmatrix}0\\v\end{pmatrix}, \tag{1.12}$$

which spontaneously breaks the $\mathrm{SU}(2)_L \times \mathrm{U}(1)_Y$ but preserves $\mathrm{SU}(3)_C \times \mathrm{U}(1)_Q$ [33].

$$\mathrm{SU}(3)_C \times \mathrm{SU}(2)_L \times \mathrm{U}(1)_Y \rightarrow \mathrm{SU}(3)_C \times \mathrm{U}(1)_Q \tag{1.13}$$

The value v comes from the choice of the potential in equation 1.1, such that $V(\Phi)$ is the simplest possible renormalizable potential,

$$V(\Phi) = -\mu^2\Phi^\dagger\Phi + \lambda(\Phi^\dagger\Phi)^2 \ ; \ \lambda > 0 \tag{1.14}$$

with a minimum at

$$v \equiv \sqrt{\frac{\mu^2}{\lambda}}. \tag{1.15}$$

As a result, fermion mass terms can be introduced via the coupling of the Higgs field to standard fermions as shown in equation 1.1,

$$\lambda^{ij}\psi_i\psi_j\Phi, \tag{1.16}$$

where λ^{ij} is the Yukawa matrix which couples the fermions to the Higgs field. Due to this Yukawa term, even though the Higgs field provides a means to give mass to each of the fermions, the theory cannot predict these masses because the elements of this matrix are free parameters (thus each fermion mass is a free parameter of the theory). Mass is provided to the Higgs boson via $V(\Phi)$ and to the $W^\pm$ and Z^0 bosons through the dynamical term $|D_\mu\Phi|^2$. Table 1.1 summarizes the Standard Model gauge charges of the fermions and Higgs boson. As a means to write the Lagrangian in a more transparent way, one can rewrite the Higgs field in the so-called unitary gauge, in which the physical states appear explicitly [40].

$$\Phi(x) = \frac{1}{\sqrt{2}}\begin{pmatrix}0\\v + H(x)\end{pmatrix}, \tag{1.17}$$

		I	I_3	Y	Q
lepton doublet	$L_L \equiv \begin{pmatrix}\nu_L \\ e_L\end{pmatrix}$	$1/2$	$1/2$ $-1/2$	-1	0 -1
lepton singlet	e_R	0	0	-2	-1
quark doublet	$Q_L \equiv \begin{pmatrix}u_L \\ d_L\end{pmatrix}$	$1/2$	$1/2$ $-1/2$	$1/3$	$2/3$ $-1/3$
quark singlet	u_R d_R	0	0	$4/3$ $-2/3$	$2/3$ $-1/3$
Higgs doublet	$\phi(x) \equiv \begin{pmatrix}\phi^+(x) \\ \phi^0(x)\end{pmatrix}$	$1/2$	$1/2$ $-1/2$	$+1$	1 0

Table 1.1: Eigenvalues of the weak isospin I, its third component I_3, hypercharge Y, and electric charge $Q = I_3 + Y/2$ of the fermion and Higgs states.

where the field $H(x)$ describes the physical Higgs boson obtained by the excitation of the neutral Higgs field above the vacuum. The dynamical term becomes

$$D_\mu(x)\Phi(x) = \frac{1}{\sqrt{2}}\begin{pmatrix} i\frac{g}{\sqrt{2}}W_\mu(x)[v + H(x)] \\ \partial_\mu H(x) - \frac{ig}{2\cos\theta_W}Z_\mu(x)[v + H(x)]\end{pmatrix}, \tag{1.18}$$

which exposes the explicit gauge boson mass terms,

$$m_W = \frac{gv}{2} \qquad m_Z = \frac{gv}{2\cos\theta_W} \tag{1.19}$$

and the fermion-Higgs couplings take an explicit form coupling right-handed and left-handed chiral fields

$$i\bar{\psi}_i\bar{\sigma}^\mu D_\mu\psi_i = -\left(\frac{v + H(x)}{\sqrt{2}}\right)\left\{\sum_{i=u,c,t}\lambda^{ij}\bar{f}_j f_j + \sum_{i=d,s,b}\lambda^{ij}\bar{f}_j f_j + \sum_{i=e,\mu,\tau}\lambda^{ij}\bar{f}_j f_j,\right\} \tag{1.20}$$

resulting in fermion masses related to the Yukawa matrix elements and the vacuum expectation value as

$$m_f = \frac{\lambda v}{\sqrt{2}}. \tag{1.21}$$

The Standard Model does a very good job at explaining most observables in particle physics, but to incorporate the exceptions to this model—neutrino oscillations, and dark

matter for example—new observables must be found which hint at physics beyond the Standard Model. The following sections give reason why searches for nucleon decay and the Majorana nature of the neutrino are important in revealing new physics.

1.2 Neutrino Mass

Despite early evidence for massless neutrinos, experiments such as Super Kamiokande [41] and SNO [42] have proven definitively that neutrinos have mass. In fact the neutrinos are each made up of a linear combination of very small mass eigenstates, which differ in scale from the other leptons by several orders of magnitude. As a means of adding mass to neutrinos, two types of neutrino masses will be discussed. A Dirac mass, which follows the same procedure as for the other fermions via the introduction of a right-handed neutrino state, and a Majorana mass, which comes from allowing a neutrino to act as its own anti-particle.

1.2.1 Dirac Mass

The simplest method of giving mass to neutrinos is to input a right-handed neutrino ν_R into the Standard Model which would then give the neutrino a mass through the Higgs mechanism. Such a model is called the *minimally extended Standard Model* [32]. Measurements of the neutrino mass imply sub-ev level masses, which would require that the Yukawa coupling of Higgs to neutrinos be very small—resulting in a fine-tuning of the Yukawa matrix for neutrino elements as compared to charged lepton elements. The eigenvalues of the gauge charges of such a neutrino would be,

		I	I_3	Y	Q
neutrino singlet	ν_R	0	0	0	0

making ν_R seemingly sterile, as it has no interaction with any of the gauge fields of the Standard Model.

1.2.1.1 Mixed Mass States

When discussing the Standard Model in previous sections, the quark mixing matrix was skipped over; however, it is now relevant to discuss this mixing as a related phenomenon can occur when adding neutrino mass to the Standard model. In equation 1.1 the term giving mass to the fermions $\lambda^{ij}\psi_i\psi_j\Phi^{(c)}$, contains the 3 x 3 matrix λ^{ij} which is in general non-diagonal. However it is possible to introduce a transformation V which diagonalizes

λ^{ij} through a bi-unitary transformation,

$$\lambda^{'ij} = V_L^\dagger \lambda^{ij} V_R, \tag{1.22}$$

where $\lambda^{'ij}$ is diagonal. The fermion fields are defined as

$$\begin{aligned} \psi_i^{'} &= V^\dagger \psi \\ \psi_R^{'} &= V_R^\dagger \psi_R \\ \psi_L^{'} &= V_L^\dagger \psi_L \end{aligned} \tag{1.23}$$

which are plugged back into the Lagrangian effectively diagonalizing the mass mixing matrix.

$$\bar{\psi}_{iR}^{'} \lambda^{'ij} \psi_{jL}^{'} \Phi = \bar{\psi}_{iL} V_L \ (V_L^\dagger \lambda^{ij} V_R) V_R^\dagger \psi_{jR} \Phi \tag{1.24}$$

With only a single right-handed doublet then it is possible to perform this operation and end up with leptons without mass mixing—mass eigenstates are equivalent to gauge interaction (flavor) eigenstates. On the other hand, when there are multiple right-handed states—as is the case in the quark sector—it is not possible to simultaneously diagonalize the Yukawa matrix in general. The convention is to diagonalize the charged leptons, leaving the Yukawa matrix for neutrinos non-diagonal, thereby causing mixing and oscillations which will be discussed in further detail later [30]. Written in the unitary gauge, the lepton mass component from equation 1.20 of the Lagrangian becomes:

$$\mathcal{L}_{leptons} = -\left(\frac{v + H(x)}{\sqrt{2}}\right) \sum_{i=e,\mu,\tau} \left\{ \lambda^{il} \bar{l}_{iL} l_{iR} + \sum_{j=1,2,3} \lambda^{i\nu} \bar{\nu}_{il} V_{ij} \nu_{jR} \right\}, \tag{1.25}$$

where the mixing matrix is chosen in such a way that the charged lepton masses are diagonalized and the neutrino masses are mixed [32].

1.2.2 Majorana Mass

The distinction between a Dirac mass and a generic description of mass comes from the fact that there is a second solution to the Dirac equation in the case where a particle and it's anti-particle are indistinguishable. Consider the field ψ which is a solution to the Dirac equation [43]

$$(i\gamma^\mu \partial_\mu - m)\psi = 0 \tag{1.26}$$

which can be split into left-handed and right-handed components

$$\psi = \psi_L + \psi_R, \tag{1.27}$$

resulting in two coupled equations for the left-handed and right-handed chiral fields

$$\begin{aligned} i\gamma^\mu \partial_\mu \psi_L &= m\psi_R, \\ i\gamma^\mu \partial_\mu \psi_R &= m\psi_L. \end{aligned} \tag{1.28}$$

In the case of a massless particle these equations become decoupled and ψ_L and ψ_R become *Weyl spinors* and the whole field exhibits chiral symmetry [1] [43]. Majorana [44] proposed a two-component Weyl spinor be used to represent a massive particle under special circumstances—requiring equation 1.28 to maintain chiral symmetry. The solution was that if ψ_L and ψ_R were related by the Majorana condition

$$\psi_R = \xi \mathcal{C} \bar{\psi}_L^T, \tag{1.29}$$

where $\mathcal{C}$ is the charge conjugation matrix, and ξ is an arbitrary phase factor ($|\xi|^2 = 1$), then a massive Weyl state could exist [32]. By performing the appropriate re-phasing the phase factor ξ is eliminated yielding the relation

$$\psi = \psi_L + \psi_R = \psi_L + \mathcal{C}\bar{\psi}_L^T = \mathcal{C}\bar{\psi}^T. \tag{1.30}$$

To interpret this, especially in the case of the neutrino field, the charge conjugation operation must be defined. The charge conjugation matrix $\mathcal{C}$ is defined with the following properties [43]

$$\begin{aligned} \mathcal{C}\gamma_\mu^T \mathcal{C}^{-1} &= -\gamma_\mu, \\ \mathcal{C}^\dagger &= \mathcal{C}^{-1}, \\ \mathcal{C}^T &= -\mathcal{C} \end{aligned} \tag{1.31}$$

and the field ψ transforms as

$$\psi(x) \to \psi^C(x) = \chi_C \mathcal{C}\bar{\psi}^T(x), \tag{1.32}$$

[1] The left and right handed components of the field transform independently under a gauge transformation. $\psi_L \to e^{i\theta_L}\psi_L$ and $\psi_R \to \psi_R$, and vice versa. This symmetry is broken with the introduction of a mass term $m\bar{\psi}\psi$.

where χ_C is the intrinsic charge parity of the field. For interactions which maximally violate this symmetry (the weak interaction for example), this intrinsic parity can be chosen arbitrarily—unity is a nice choice. In which case,

$$\psi = \psi^C, \tag{1.33}$$

implying that a massive field can be represented as a 2-component chiral field in the case where that field can violate charge conjugation symmetry. The electromagnetic field explicitly cannot do this, so it is not possible for charged leptons (or quarks) to be Majorana fields; however, the neutrino can satisfy this condition. A consequence of a Majorana neutrino is that a mass term can be constructed via the Higgs mechanism which is does not require the introduction of a right-handed sterile neutrino. This follows from the lepton-Higgs coupling via [32]

$$\mathcal{L}_5 = \frac{g}{\Lambda}(\psi_L^T \sigma_2 \phi)\mathcal{C}^\dagger(\phi^T \sigma_2 \psi_L) \tag{1.34}$$

where σ_2 is the generator of SU(2) (Pauli matrices). This term will generate a neutrino mass through the usual electroweak symmetry breaking, though is itself non-renormalizable as it is dimension 5. This can be rewritten in the unitary gauge as,

$$\mathcal{L}^M_{\text{mass}} = \frac{1}{2}\frac{gv^2}{\Lambda}\nu_L^T \mathcal{C}^\dagger \nu_L, \tag{1.35}$$

where the neutrino mass picks up a quadratic dependence on the vacuum expectation value as well as a suppression from the scale factor Λ.

1.2.3 Dirac-Majorana Mixing

Previously the Majorana and Dirac mass terms where introduced individually; however, the two can both contribute in combination to give the full neutrino mass, with an extra caveat. The Majorana mass term introduced in equation 1.35 assumes there is only the left-handed neutrino from the Standard Model. Adding in a right-handed neutrino, as is required to incorporate a Dirac mass term, will also generate a right-handed Majorana mass. The full neutrino mass components of the Lagrangian becomes the sum of these components, taking the form:

$$\mathcal{L}_{\nu\ \text{mass}} = \frac{1}{2} m_L \nu_L^T \mathcal{C}^\dagger \nu_L + \frac{1}{2} m_R \nu_R^T \mathcal{C}^\dagger \nu_R - m_D \bar{\nu}_R \nu_L + h.c. \tag{1.36}$$

Through a set of transformations, where the neutrino fields are defined through the column vector:

$$N_L = \begin{pmatrix} \nu_L \\ \mathcal{C}\bar{\nu}_R^T \end{pmatrix} = \begin{pmatrix} \nu_L \\ \nu_R^C \end{pmatrix}, \tag{1.37}$$

the mass Lagrangian can be rewritten as a single matrix term,

$$\mathcal{L}_{\nu \text{ mass}} = \frac{1}{2} N_L^T \mathcal{C}^\dagger M N_L \tag{1.38}$$

where the symmetric mass matrix is defined as:

$$M = \begin{bmatrix} m_L & m_D \\ m_D & m_R. \end{bmatrix} \tag{1.39}$$

When diagonalized by a unitary matrix U the Lagrangian is simplified to a Majorana term with two mass eigenstates m_1 and m_2, which are mixed states of the left and right handed chiral states,

$$\begin{aligned} \mathcal{L}_{\nu \text{ mass}} &= -\frac{1}{2} \sum_{k=1,2} m_k \bar{\nu}_k \nu_k, \\ \nu_L &= U_{11}\nu_{1L} + U_{12}\nu_{2L}, \\ \nu_R^C &= U_{21}\nu_{1L} + U_{22}\nu_{2L}. \end{aligned} \tag{1.40}$$

Such a mechanism would allow neutrinos to oscillate to sterile right-handed states via the mixing matrix U [45].

1.2.3.1 See-saw Mechanism

Of the possible values of m_L, m_R, and m_D, there is a specific combination that naturally produces a small neutrino mass as well as local gauge symmetry of the Standard Model. The difference between the two Majorana contributions is that the purely left-handed mass term contains a pair of SU(2) doublet neutrino states, and therefore does not conserve the symmetry SU(2) $\times$ SU(1), whereas the purely right-handed mass term has SU(2) singlets and is symmetric under Standard Model gauge transformations. This motivates a choice of $m_L = 0$ in order to eliminate that term from the Lagrangian. Furthermore, because the Dirac mass comes about in a similar manner to the leptons and quarks, its mass should be similar to the other fermions, and at the very least, less than the spontaneous symmetry breaking scale. Finally, the remaining Majorana mass term is the result of some higher

energy theory at the scale Λ, so it is free to have a very large mass (it is not protected by the electroweak symmetry breaking scale as the other fermions are). The conditions that follow are

$$m_L = 0 \qquad m_R \gg m_D. \tag{1.41}$$

One finds that upon applying this condition, the physical mass states m_1 and m_2, which are related to m_R and m_D by

$$m_1 \simeq \frac{m_D^2}{m_R}, \qquad m_2 \ \simeq m_R. \tag{1.42}$$

Such a choice forces the left-handed active neutrino state ν_L to comprise mostly of the small m_1 state while the right-handed sterile neutrino ν_R would have a very large mass—likely near the GUT scale—while naturally avoiding fine tuning of the Yukawa coupling [46] [45]. A heavy sterile neutrino would decay very quickly under the standard model to its light components; however, models with keV scale right-handed neutrino models would provide a constituent of warm dark matter. The contribution of warm dark matter to the total dark matter mass of the universe is predicted to be small with current measurements favoring a predominantly cold dark matter universe [47] [48].

1.2.4 Neutrino Oscillations

Due to the importance of neutrino oscillation experiments in solidifying the existence of neutrino mass, an overview of the mechanisms involved will be given here. Neutrino oscillations themselves do not play an important role in proton decay, and exist regardless of the Dirac-Majorana nature of neutrinos. Neutrino oscillations were first proposed by Pontecorvo [49] in analogy with $K^0 - \bar{K}^0$ oscillations, which manifest from the mass difference of quarks. In a similar fashion to quarks, the neutrino mass states and neutrino interaction (flavor) states are related through a unitary transformation which denoted V—the Pontecorvo-Maki-Nakagawa-Sakata (PMNS) matrix [49] [50].

$$|\nu_\alpha\rangle = \sum_k V_{\alpha k}^* \, |\nu_k\rangle \quad \text{and} \quad |\nu_k\rangle = \sum_\alpha V_{\alpha k} \, |\nu_\alpha\rangle \tag{1.43}$$

where α represents the three flavor eigenstates $(\nu_e, \nu_\mu, \nu_\tau)$, and k represents the three mass eigenstates (ν_1, ν_2, ν_3). This distinction is important because however the Lagrangian

is constructed, the diagonalization of the Yukawa matrices for both charged lepton and neutrino mass will inevitably cause a non-diagonal charged current interaction in the dynamical term [32]. For three families of neutrinos, the mixing matrix V can be represented as a 3x3 unitary matrix, of which any orthogonal $n \times n$ unitary matrix has $\frac{n(n-1)}{2}$ independent parameters. The usual way to represent this matrix is through three angles of rotation ($\theta_{23}, \theta_{13}, \theta_{12}$ and three phase factors ($\delta_{cp}, \phi_2, \phi_3$) [51].

$$V = \begin{bmatrix} 1 & 0 & 0 \\ 0 & c_{23} & s_{23} \\ 0 & -s_{23} & c_{23} \end{bmatrix} \begin{bmatrix} c_{13} & 0 & s_{13}e^{-i\delta_{cp}} \\ 0 & 1 & 0 \\ -s_{13}e^{-i\delta_{cp}} & 0 & c_{13} \end{bmatrix} \begin{bmatrix} c_{12} & s_{12} & 0 \\ -s_{12} & c_{12} & 0 \\ 0 & 0 & 1 \end{bmatrix} \begin{bmatrix} 1 & 0 & 0 \\ 0 & e^{i\phi_2/2} & 0 \\ 0 & 0 & e^{i\phi_3/2} \end{bmatrix} \tag{1.44}$$

where c_{ij} denotes $\cos\theta_{ij}$ and s_{ij} denotes $\sin\theta_{ij}$. The phase space factor δ_{cp} is a measure of the level at which the weak interaction violates charge-parity symmetry, and ϕ_2 and ϕ_3 are Majorana phase factors—which play no role in neutrino oscillations.

Unlike the quarks, neutrinos exist in nature as bare particles, and thus have the opportunity to traverse over long distances based on their momentum. Since an interaction must produce a neutrino in a fixed flavor eigenstate (as required by the gauge interaction vertex), the neutrino is not itself in a mass eigenstate. The mass eigenstate is an eigenstate of the Hamiltonian $\mathcal{H}$ whose eigenvalue is given by the total energy of the neutrino,

$$\mathcal{H} \left|\nu_k\right\rangle = E_k \left|\nu_k\right\rangle , \tag{1.45}$$

with eigenvalues,

$$E_k = \sqrt{\vec{\mathbf{p}}^2 + m_k^2}. \tag{1.46}$$

Classical quantum mechanics will tell us that the time evolution operator on the neutrino will obey Schrödinger's equation, and because the lepton flavor states are not eigenvalues of the Hamiltonian, the superposition of these flavor states will interfere.

$$i\frac{\mathrm{d}}{\mathrm{d}t}\left|\nu_k(t)\right\rangle = \mathcal{H}\left|\nu_k(t)\right\rangle , \tag{1.47}$$

whose plane wave solution,

$$\left|\nu_k(t)\right\rangle = e^{-iE_k t}\left|\nu_k\right\rangle , \tag{1.48}$$

leads to neutrino oscillations in the flavor eigenstates by substitution with equation 1.43 [32]:

$$|\nu_\alpha(t)\rangle = \sum_k V^*_{\alpha k} |\nu_k(t)\rangle = \sum_k V^*_{\alpha k}(e^{-iE_k t} \sum_\beta V_{\beta k} |\nu_\beta\rangle). \tag{1.49}$$

The transition probability—the probability that a neutrino of flavor α is measured as flavor β as a function of time—is determined by finding the expectation value of the final wavefunction [32],

$$P_{\alpha\to\beta}(t) = |\langle\nu_\beta|\nu_\alpha(t)\rangle|^2 = \sum_{kj} V^*_{\alpha k} V_{\beta k} V_{\alpha j} V^*_{\beta j} \exp\Big(-i(E_k - E_j)t\Big). \tag{1.50}$$

In the ultra relativistic limit[2] the energy difference term can be reduced to information relevant to detection experiments [51]

$$P_{\alpha\to\beta}(t) = |\langle\nu_\beta|\nu_\alpha(t)\rangle|^2 = \sum_{kj} V^*_{\alpha k} V_{\beta k} V_{\alpha j} V^*_{\beta j} \exp\left(-i\frac{\Delta m^2_{kj} L}{2E}\right), \tag{1.51}$$

which is the quintessential neutrino oscillation formula which can be compared to data to determine the elements of the oscillation matrix V. Since the bare PMNS matrix itself is not an easy observable, the transition probability $P_{\alpha\to\beta}$ is left as the best observable.

1.2.4.1 Oscillation Experiments

In an effort to quantify the elements of the neutrino mixing matrix, many experiments have been performed which focus on particular regions of the mixing matrix via measurements of the neutrino transition probability (equation 1.51), or conversely the survival probability $P_{\alpha\to\alpha}(t)$. Contained in the transition probability is information on the mixing angles from the products of the PMNS matrix as well as information on the neutrino mass differences from the expectation value of the time evolution operator.

Note that there is not a direct measurement of any particular mass state, but rather the differences in mass states, giving no information on the neutrino absolute mass from oscillation experiments. Furthermore, the sign of the mass differences is not known, leaving to possible mass orderings as shown in figure 1.2.

[2] $E_k \approx E + m^2_k/(2E)$ where E is taken as the same to first order for both states. The difference becomes $E_k - E_j = (m^2_k - m^2_j)/(2E) \equiv (\Delta m^2_{kj})/(2E)$. Likewise $t \approx L$, where L is distance traversed, since the neutrinos are moving near c.

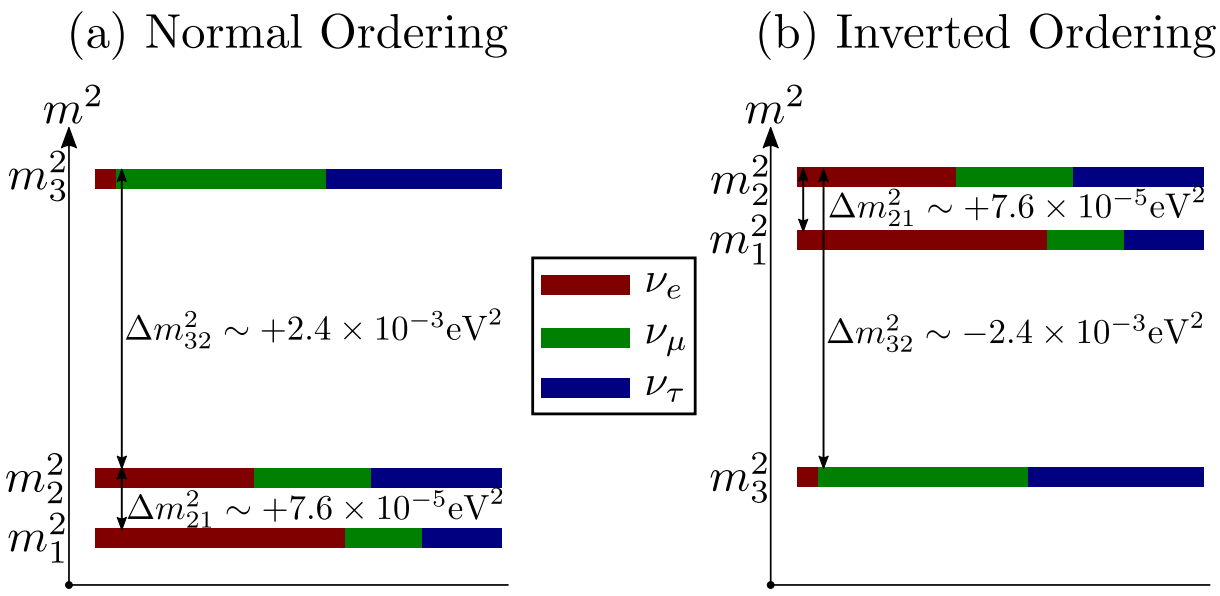

Figure 1.2: Neutrino mass ordering for the normal and inverted schemes [2].

Experiment	Dominant	Important
Solar Experiments	θ_{12}	$\Delta m^2_{21}, \theta_{13}$
Reactor LBL	Δm^2_{21}	θ_{12}, θ_{13}
Reactor SBL	θ_{13}	$\lvert\Delta m^2_{3l}\rvert$
Atmospheric Experiments	θ_{23}	$\lvert\Delta m^2_{3l}\rvert, \theta_{13}, \delta_{cp}$
Accelerator LBL ν_μ Disappearance	$\lvert\Delta m^2_{3l}\rvert, \theta_{23}$	
Accelerator LBL ν_e Appearance	δ_{cp}	$\theta_{13}, \theta_{23}, \text{sign}(\Delta m^2_{3l})$

Table 1.2: Importance of experiments in the contribution to neutrino oscillation parameters showing both the dominant parameter of interest, as well as secondary contributions (labeled Important). Shown above is the difference in Long Baseline (LBL) and Short Baseline (SBL) experiments. [21]

The primary natural sources of neutrinos come from solar neutrinos which are created in the interior of the sun through nuclear fusion, and atmospheric neutrinos which come from high-energy cosmic rays. Human made sources of neutrinos are the result of nuclear fission reactors and accelerator experiments which can produce neutrino beams at tunable energies and distances. Each of these sources is key in isolating components of the mixing matrix as shown in table 1.2.

1.2.4.2 Solar Neutrinos

Solar neutrinos are created during nuclear fusion processes predominantly through the *pp* chain and the CNO cycle resulting in,

$$4p \rightarrow {}^{4}\mathrm{He} + 2\nu_e + 2e^{+}, \tag{1.52}$$

with various energy spectra depending on the particular fusion process as shown in figure 1.3. Solar neutrino measurements made by the SNO experiment [52] and Super-Kamiokande [53] (as well as many others) were key in the discovery of neutrino oscillations and in determining the mixing parameters θ_{12} and Δm^2_{12}. The SNO experiment in particular was able to distinguish ν_e solar neutrinos from the other flavors by comparing charged current interactions, which are flavor specific, to neutral current and scattering interactions,

$$\begin{aligned} \nu_e + d &\rightarrow p + p + e^{-} \\ \nu_x + d &\rightarrow p + n + \nu_x \\ \nu_x + e^{-} &\rightarrow \nu_x + e^{-} \end{aligned} \tag{1.53}$$

which provided direct evidence for neutrino flavor oscillations [54]. As will be discussed in a later section, solar neutrinos act as a background to SNO+ during the search for invisible nucleon decay due to their broad spectrum (particularly the ${}^{8}B$ neutrinos which are the predominant source of solar neutrinos above 5 MeV) [55].

1.2.4.3 Atmospheric Neutrinos

Atmospheric neutrinos are the result of high-energy cosmic rays bombarding the upper atmosphere producing hadronic showers. The pions from the hadronic showers decay via,

$$\pi^{-} \rightarrow \mu^{-} + \nu_\mu \text{ and } \pi^{+} \rightarrow \mu^{+} + \bar{\nu}_\mu \tag{1.54}$$

which then further decay to

$$\mu^{-} \rightarrow e^{-} + \nu_e \text{ and } \mu^{+} \rightarrow e^{+} + \bar{\nu}_e, \tag{1.55}$$

resulting in the production of ν_μ, $\bar{\nu}_\mu$, ν_e, and $\bar{\nu}_e$. Atmospheric neutrinos have a variable baseline which is ideal for an oscillation experiment. Downward going neutrinos (short

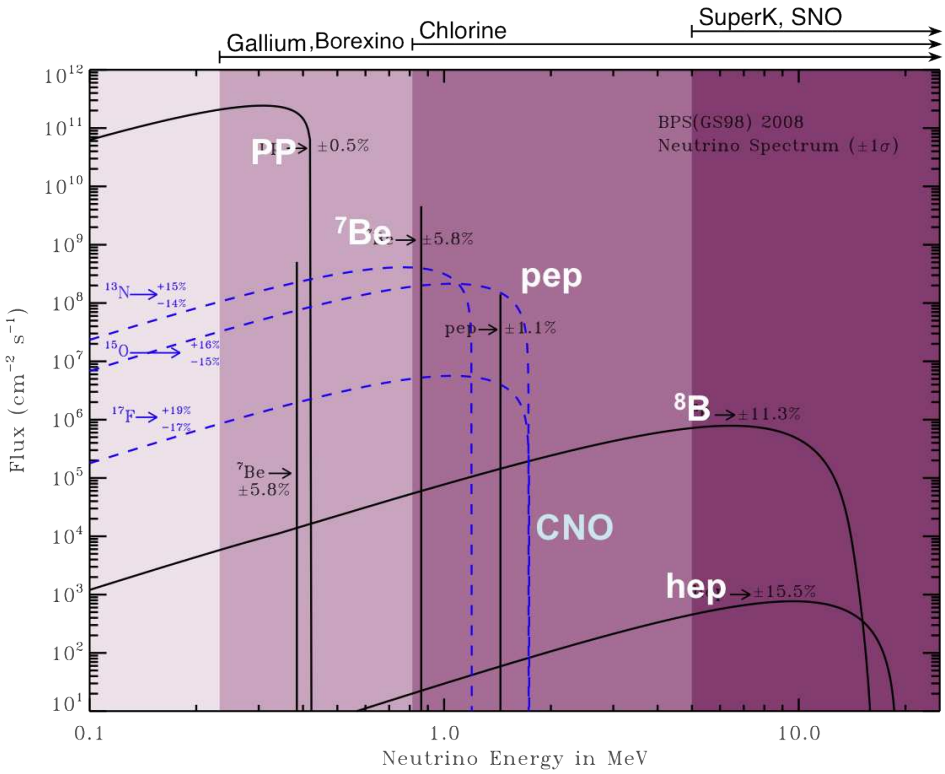

Figure 1.3: Solar neutrino spectrum with expected detector sensitivities using the Standard solar model [3].

baseline) can be compared with the expected rate of upward going neutrinos (long baseline) to determine the transition probability $P_{\mu\to\tau}$ (and to a lesser extent $P_{e\to\tau}$) to find the oscillation parameters from ν_μ and ν_e to ν_τ. Both ν_e, and ν_μ can be detected through the charged current interaction [32]

$$\nu_l + N \to l^- + X, \quad \bar{\nu}_l + N \to l^+ + X, \tag{1.56}$$

which for an experiment with the ability to distinguish muons from electrons, provides a measurement of the mixing angles θ_{13} and θ_{23}. The Super-Kamiokande detector was able to measure the ratio of the neutrino flux, $(\nu_\mu + \bar{\nu}_\mu)/(\nu_e + \bar{\nu}_e)$, which resulted in an up/down deficit of $0.54^{+0.06}_{-0.05}$ with respect to unity (a more than 6σ effect), confirming the neutrino oscillation hypothesis [56].

1.2.4.4 Reactor Neutrinos

Nuclear fission reactors produce many $\bar{\nu}_e$ through β^- decay of heavy, neutron rich isotopes such as ^{235}U, ^{238}U, ^{239}Pu, and ^{241}Pu.

$$ {}^{A}_{Z}X \rightarrow {}_{Z-1}{}^{A}Y + \bar{\nu}_e + e^-, \tag{1.57} $$

Reactor anti-neutrinos are an ideal candidate for the measurement of the transition probability of $\bar{\nu}_e$, $P_{e\rightarrow X}$, to either ν_μ or ν_τ due to their narrow ($\sim$ 10 MeV) emission spectrum (figure 1.4). Furthermore, the baseline can be controlled precisely by choice of experimental location, so it is possible to probe (and separate) the two oscillations through multiple experiments with fixed L/E. The KamLAND experiment, located in the Kamioka mine in the Japanese Alps, measured the disappearance of reactor $\bar{\nu}_e$ from a large number of nearby nuclear power reactors with long baseline (of order 100 km). Results from this experiment set strong experimental bounds on Δm^2_{21} with dependence on θ_{12}, and θ_{13} [57]. Short baseline reactor experiments, such as the Daya-Bay experiment [58] and Double Chooz [53], lead to a global fit of θ_{13} given in table 1.3.

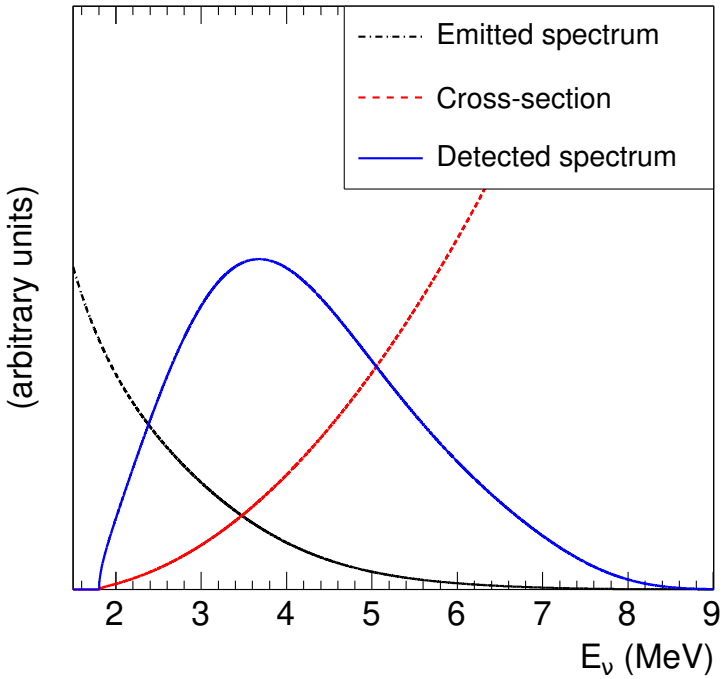

Figure 1.4: Sample reactor anti-neutrino energy spectrum convolved with the inverse beta decay cross section [4].

1.2.4.5 Accelerator Neutrinos

Despite the abundance of naturally occurring neutrino sources, neutrinos are also produced through accelerator facilities using a similar mechanism as atmospheric neutrinos. Pion and muon facilities can produce a tuned source of ν_e, $\bar{\nu}_e$, ν_μ, and $\bar{\nu}_\mu$ with tight timing windows (bunches) aimed at neutrino detectors at fixed distance. The current generation of long-baseline neutrino experiments consists of T2K, Minos/Minos+, and Noνa. The three experiments together have put constraints on θ_{23} and Δm^2_{23} through measurements of neutrino oscillations $\nu_e \leftrightarrow \nu_\mu$ and $\bar{\nu}_e \leftrightarrow \bar{\nu}_\mu$ (figure 1.5)[59]. T2K primarily focuses on ν_e appearance from the J-Parc accelerator facility in Tokai, Japan, to Super-Kamiokande at a distance of 295 km [60]. Minos and Noνa both use the NuMI beam coming from Fermilab, with baselines of 735 km and 810 km respectively [61] [60]. Both T2K and Noνa are situated off-axis from their respective neutrino beams which lowers the overall neutrino number of neutrino interactions per bunch, but creates a narrower energy spectrum of incident neutrinos. In contrast MINOS is directly in line with the Fermilab neutrino beam. Beyond just measuring the oscillation angles, accelerator experiments have some sensitivity to the mass ordering and δ_{cp}, giving rise to future experiments such as DUNE—which will also be based out of Fermilab, with a far detector at 1300 km [62]. DUNE will measure both $\nu_\mu \rightarrow \nu_e$ and $\bar{\nu}_\mu \rightarrow \bar{\nu}_e$ which will show signs of an asymmetry in the case where $\delta_{CP} \neq \pi$ or 0. Due to matter effects (which differ for neutrinos and antineutrinos) the oscillation probabilities further change as the effective mass splittings change due to the matter potential. At long baselines the matter effects dominate the asymmetry giving DUNE a very good sensitivity to the mass ordering.

1.2.4.6 Oscillation Parameter Global Fit

Various neutrino sources have provided strong constraints on the neutrino oscillation parameters as shown in table 1.3. Notably, future experiments will focus on determining if neutrinos are CP violating (and if so by how much) through the measurements of δ_{cp} as well as determining the mass ordering. It may be also possible to measure the absolute neutrino masses through experiments such as KATRIN through precision measurements of the tritium beta decay end point [63].

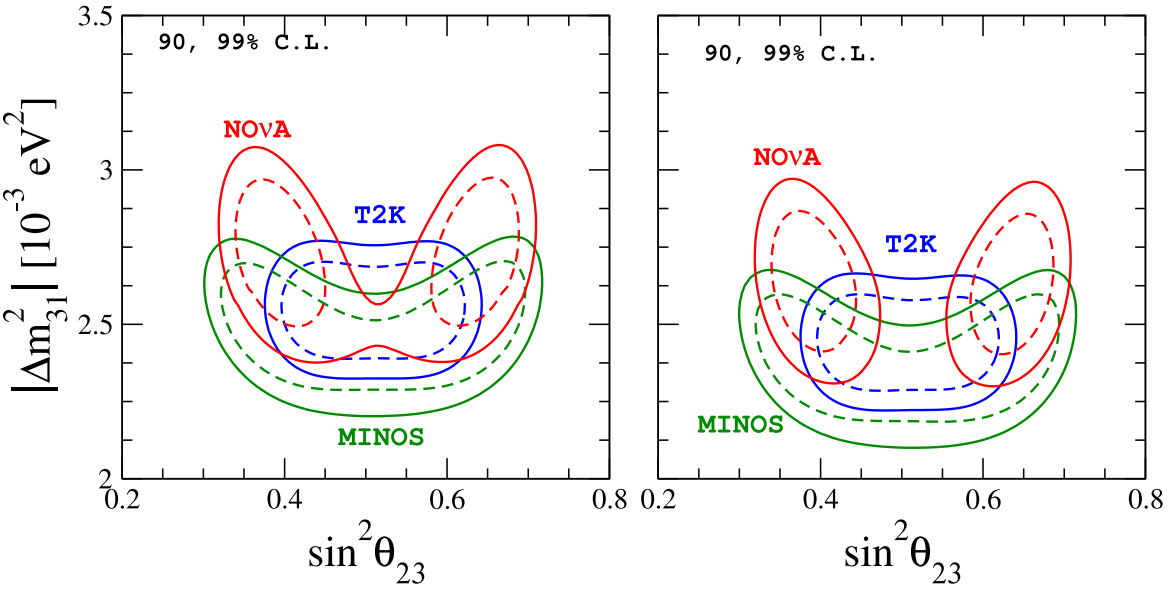

Figure 1.5: Allowed regions for the neutrino oscillation parameters Δm^2_{31} and $\sin^2\theta_{23}$ for the normal (left) and inverted (right) mass ordering. Contours show the 90% and 99% confidence interval [5].

Parameter	best fit $\pm$ 1σ (NO)	best fit $\pm$ 1σ (IO)
$\Delta m^2_{21}[10^{-5}\text{eV}^2]$	7.56 ± 0.19	SAME
$\lvert\Delta m^2_{31}\rvert[10^{-3}\text{eV}^2]$	2.55 ± 0.04	2.49 ± 0.04
$\sin^2\theta_{12}/10^{-1}$	$3.21^{+0.18}_{-0.16}$	SAME
$\theta_{12}/^\circ$	$34.5^{+1.1}_{-1.0}$	SAME
$\sin^2\theta_{23}/10^{-1}$	$4.30^{+0.20}_{-0.18}$	$5.96^{+0.17}_{-0.18}$
$\theta_{23}/^\circ$	41.0 ± 1.1	50.5 ± 1.0
$\sin^2\theta_{13}/10^{-2}$	$2.155^{+0.090}_{-0.075}$	$2.140^{+0.082}_{-0.085}$
$\theta_{13}/^\circ$	$8.44^{+0.18}_{-0.15}$	$8.41^{+0.16}_{-0.17}$
δ_{cp}/π	$1.40^{+0.31}_{-0.20}$	$1.44^{+0.26}-0.23$

Table 1.3: Global fit to neutrino oscillation parameters [5].

1.2.5 Neutrinoless $\beta\beta$ Decay

The exact nature of neutrino mass has little bearing on neutrino oscillations; however, the observation of neutrinoless $\beta\beta$ decay would be a smoking gun for the existence of Majorana neutrinos. The normal β decay mechanism—shown in figure 1.6—involves the

charge current interaction which converts a down type quark into an up type quark via the exchange of a virtual W^- boson. Emitted from this process is an e^- and an electron $\bar{\nu}_e$.

Due to the nature of this process, as well as the inability to observe the emitted neutrino,

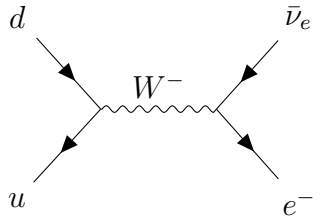

Figure 1.6: Feynman diagram of β-decay.

there is an apparent spectrum to emitted electrons. Consequently this was observed by James Chadwick [64] and lead to the prediction of the neutrino by Wolfgang Pauli [65].

In nature quarks are only found bound within protons and neutrons in relative abundance—or at the very least bound in short lived mesons. Even when bound in a neutron the lifetime is only 880.3 seconds [30]. For a stable nucleus the energy that could be emitted by a neutron (or a proton for that matter) must be greater than the difference in nuclear binding energies between the initial and final state nuclei, otherwise the nucleon cannot overcome the nuclear potential holding the nucleus together and the process is forbidden. It is possible, for a select few nuclei, that a single instance of beta decay is energetically disallowed but the energy difference for two simultaneous beta decays is allowed. Both for reference and relevance to the SNO+ experiment, the decay scheme for ^{130}Te is shown in figure 1.8. The Feynman diagram for neutrinoless double β-decay is shown in figure 1.7.

This type of decay scheme provides a unique opportunity to look for physics beyond the Standard Model via the decay of some ordinary isotopes. Due to the nature of beta decay, one would expect the emission of double beta decay to be a pair of electrons and a pair of anti-neutrinos associated with those electrons. While this will always be the dominant mode of decay, it is possible for Majorana neutrinos to act as a mediator in the interaction and virtually annihilate, leaving a final state of only the two electrons. From

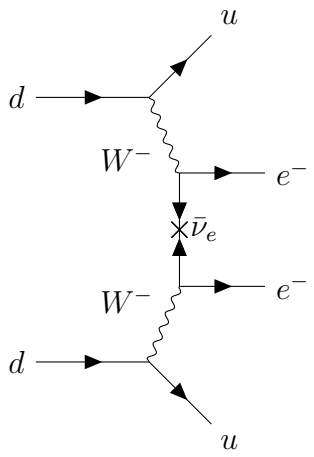

Figure 1.7: Feynman depicted neutrinoless double β-decay $0\nu\beta\beta$, where the anti-neutrinos effectively cancel one-another (forming a propagator).

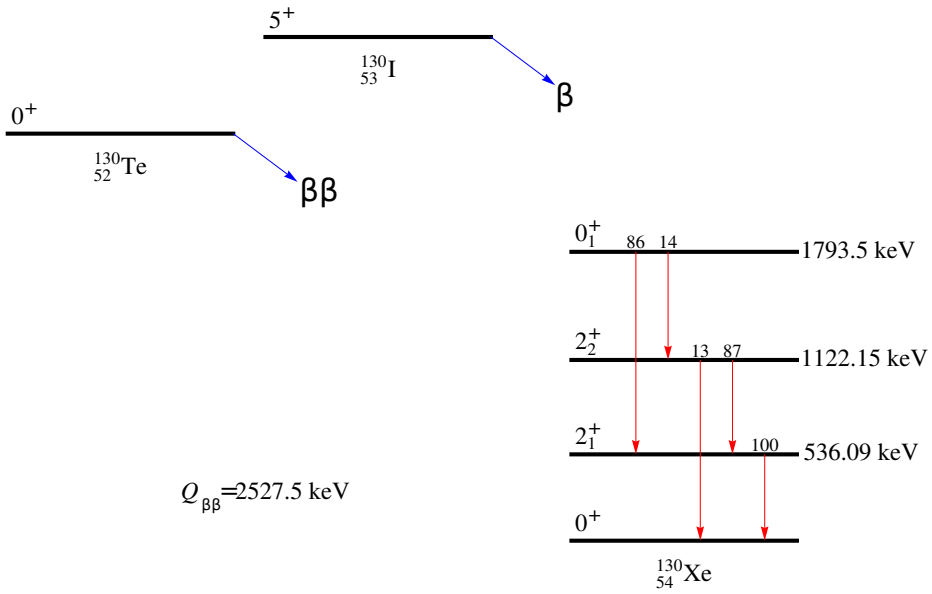

Figure 1.8: ^{130}Te decay scheme showing the energetically forbidden β decay transition to ^{130}I but the allowed $\beta\beta$ decay transition to ^{130}Xe, including the Q-value of the reaction and the emitted γ of the nuclear transitions [6] [7].

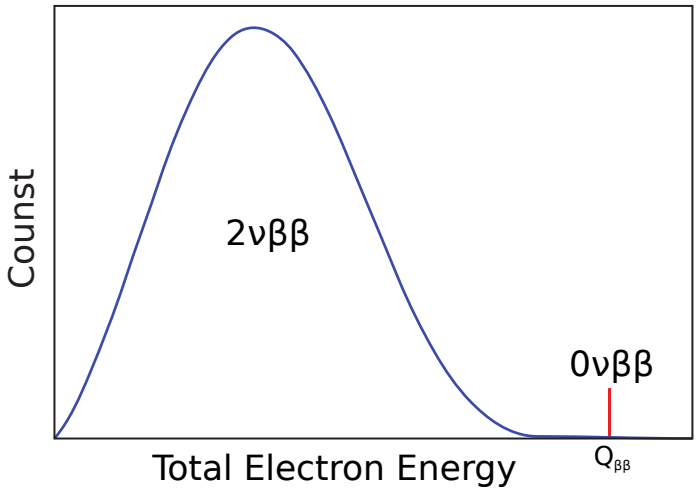

Figure 1.9: Schematic comparing $2\nu\beta\beta$ spectrum to $0\nu\beta\beta$ mono-energetic peak [8].

the standpoint of a detector—where only the electrons can be measured—this corresponds to a mono-energetic signal as opposed to the usual spectrum one associates with measuring two parts of a 5 body decay as is demonstrated in figure 1.9.

1.2.5.1 Determining $m_{\beta\beta}$

Experimentally all one has to do is measure the rate of events at the $\beta\beta$ endpoint to determine the lifetime for that particular process; however, turning a lifetime into the Majorana neutrino mass is often non-trivial. Considering the contribution of the mass term to the Lagrangian, and noting that the PMNS matrix defined in neutrino oscillations is the matrix which diagonalizes the neutrino mass component, one finds [66]:

$$\langle m_{\beta\beta} \rangle = \left| \sum_j m_j V_{ej}^2 \right|, \tag{1.58}$$

where the electron-flavor components of the mass mixing matrix are summed over. One aspect of the effective neutrino mass which is very important, is that the expression is proportional to V_{ej}^2 and not $|V_{ej}|^2$, so the phase factors ϕ_2 and ϕ_3 in the mixing matrices contribute to the value of $\langle m_{\beta\beta} \rangle$. These phases are often called the Majorana phases [66], and cannot be constrained through oscillation measurements. Due to this, the values of these phases must float when assigning confidence bands on $m_{\beta\beta}$. The phase space for the $m_{\beta\beta}$ for current global oscillation parameters are drawn out in figure 1.10 where the width

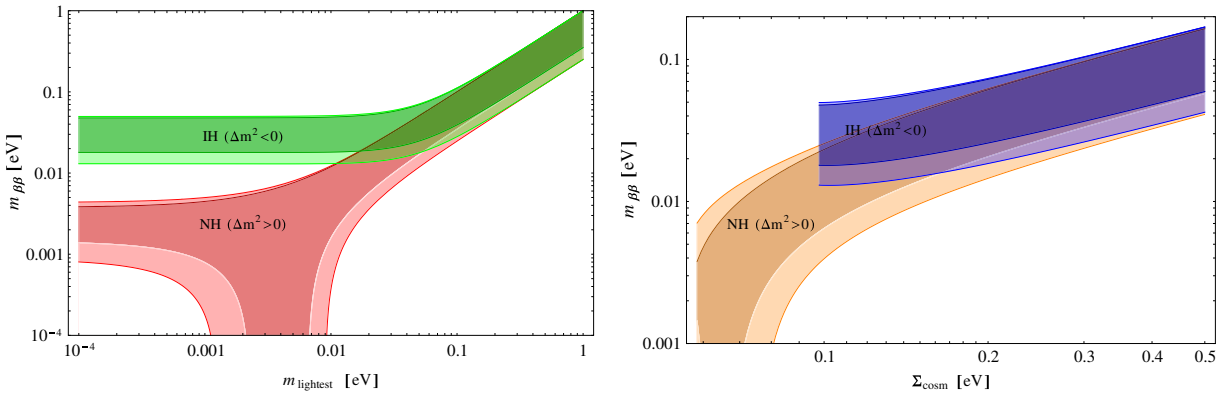

Figure 1.10: Predictions of $m_{\beta\beta}$ from oscillations as a function of lightest neutrino mass (left) and cosmological mass (right), with the shaded regions representing 3σ uncertainties on the known oscillation parameters [9].

of the darker region of the bands comes from the unknown value of the Majorana phases, and the lighter shaded region gives the 3σ uncertainties on the oscillation parameters. Notice that the phase space for the normal and inverted ordering become distinguishable for very small $m_{\beta\beta}$, and in fact only in the inverted ordering can the Majorana neutrino mass be positively excluded.

$\beta\beta$ decay is a nuclear process which requires proper calculation of nuclear structure and dynamics in order to translate from an observable quantity—such as decay rate—into the parameter of interest ($m_{\beta\beta}$). A general formulation of the half-life for a particular nuclear decay can be made by invoking Fermi's golden rule with an extra modification to account for new physics[8],

$$[t^{1/2}]^{-1} = G_{0\nu}|\mathcal{M}|^2|f(m_i, V_{ei})|^2, \tag{1.59}$$

where $G_{0\nu}$ is the exactly calculable phase space integral, $\mathcal{M}$ is the nuclear matrix element which describes the transition from the initial to final nuclear states, and $f(m_i, V_{ei})$ is some function which describes the new physics which allows for this process. Using the simple light neutrino model [66],

$$f(m_i, V_{ei}) = \langle m_{\beta\beta} \rangle \,, \tag{1.60}$$

$m_{\beta\beta}$ can be calculated for a measured value of $t^{1/2}$ given $G_{0\nu}$ and $\mathcal{M}$.

Calculations of the phase space integral, first done by Primakoff [67] then Haxton [68]

Isotope	Isotopic Abundance (%)	$Q_{\beta\beta}$ [MeV]	$G_{0\nu}$ (10^{-15}yr^{-1})
^{48}Ca	0.187	4.263	24.9
^{76}Ge	7.8	2.039	2.34
^{82}Se	9.2	2.998	10.1
^{96}Zr	2.8	3.348	20.3
^{100}Mo	9.6	3.035	15.7
^{116}Cd	7.6	2.813	16.6
^{130}Te	34.08	2.527	14.1
^{136}Xe	8.9	2.459	14.6
^{150}Nd	5.6	3.371	62.0

Table 1.4: Phase space factor for various common $\beta\beta$ decay isotopes [22].

in the non-relativistic case, involve integration over all possible energies and angles of the leptons emitted in the decay [22]. With modern techniques applied by Stoica [69] yielding improvements to the analytic values for the phase-space integrals—especially for heavier nuclei. Numerical values of $G_{0\nu}$ are given in table 1.4 along with the double beta decay endpoint for various candidate isotopes.

The nuclear matrix element is often a bit more complicated to calculate in that the results are heavily model dependent. In principle one only needs to find the overlap between the initial and final state wavefunctions $|\langle\psi_i|\psi_f\rangle|$. In practice this involves mapping out all possible transitions between the two complex multi-body systems which involve both Fermi and Gamow-Teller transitions [3]. Several models exist for calculating the nuclear matrix elements of which the leading models are the *Interacting Shell Model*, the *Quasiparticle Random Phase Approximation*, and the *Interacting Boson Model* [8]. Calculations and the variation of these models is shown in figure 1.11 for various candidate isotopes. While the nuclear matrix element for the $2\nu\beta\beta$ does not directly contribute to the $0\nu\beta\beta$ matrix element, it does offer a means to validate the methods used to calculate

[3] Fermi transitions are vector transitions which have no change in total angular momentum. Gamow-Teller transitions are axial-vector transitions which allow for a total angular momentum change of ±1 or 0, but forbid transitions from $0 \rightarrow 0$ spin states. [70]

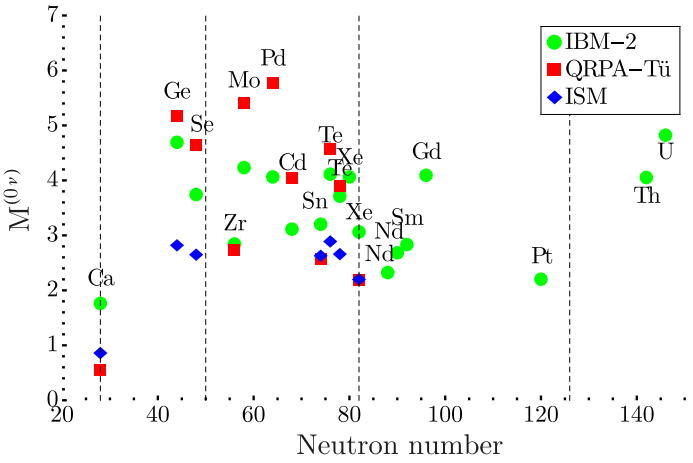

Figure 1.11: Comparison of nuclear matrix elements for various candidate isotopes using IBM-2 [10], QRPA [11], and ISM [12] from [10]. For ^{130}Te $\rightarrow$ ^{130}Xe, the results are IBM-2: 3.70, QRPA: 3.89, and ISM:2.65.

the matrix elements for a particular nucleus, and can be validated through the $2\nu\beta\beta$ spectral measurement and lifetime.

1.2.5.2 $\beta\beta$ Experiment Limits

There are a variety of detectors that have been designed and run with the intent of measuring $0\nu\beta\beta$ decay, each offering distinct advantages. Broadly speaking these can be grouped into highly sensitive detectors (in terms of resolution) with often smaller target masses, and very large detectors with poor energy resolution but a large target mass. SNO+ would be in the latter of the two categories, which is a favorable type of detector if your goal is to merely discover $0\nu\beta\beta$, but would struggle to make a precision measurement of $m_{\beta\beta}$. Experiments also tend to be grouped together by their target isotope, since any uncertainties in the nuclear matrix element and phase space factor are correlated across these experiments and so they can be compared directly. In order to directly compare results with SNO+, CUORE-0 is the leading experiment for ^{130}Te with current limits of $T^{0\nu}_{1/2} > 2.7 \times 10^{24}$ years at 90% confidence level, which for a range of nuclear matrix elements, sets a limit of $m_{\beta\beta} < 270 - 760$ meV [71]. The strongest limit on $m_{\beta\beta}$ is set by the KamLAND-Zen collaboration with a limit of $m_{\beta\beta} < 61 - 165$ meV using the isotope ^{136}Xe [72].

1.3 Nucleon Decay

There have been many proposed extensions to the Standard Model that can explain neutrino mass, the hierarchy problem, and other anomalies which require modification of the Standard Model. Many of these theories have either been ruled out, or have had their phase-space for discovery reduced substantially; however, to motivate and describe the history of the search for nucleon decay, they will be described here briefly. Of particular interest are theories which can predict phenomena that have observable effects even at energies that can be reached by modern detectors. One such phenomena is nucleon decay through non-Standard Model modes. One consequence of requiring the Standard Model to be almost correct, is that any additions must be made in a way in which corrections are very small, meaning for proton decay the lifetime would need to be very long. Luckily protons come rather cheap and it is feasible to gather many of them together in a single detector and watch for decays to happen. First though, lets motivate such a search through reasonable theoretical models.

1.3.1 Grand Unification

It is always possible to add more gauge fields into the Lagrangian, which in turn introduces more gauge bosons. The idea of grand unification is that the individual gauge fields seen at low energy are actually the subset of a larger group which only manifests as a single unified gauge at very high energy [73] [74]. This is immediately enticing because it says that Nature is in fact just a single symmetry group whereby all physical phenomena can be derived. By enforcing such a condition one finds that SU(5) is the smallest group which contains $\mathrm{SU}(3) \times \mathrm{SU}(2) \times \mathrm{U}(1)$ as a subgroup [75] —which is required so that the theory can be spontaneously broken to recover the Standard Model. Such a unification would then have to be spontaneously broken (just as before), at some "GUT" scale as well as in the usual way via the Higgs mechanism.

$$\mathrm{SU}(5) \rightarrow \mathrm{SU}(3)_C \times \mathrm{SU}(2)_L \times \mathrm{U}(1)_Y \rightarrow \mathrm{SU}(3)_C \times \mathrm{U}(1)_Q \tag{1.61}$$

1.3.1.1 SUSY and non-SUSY SU(5) and SO(10)

Depending on the particular model for the grand unification, the gauge coupling converge at different energies, but are always well beyond modern detector limits. For example, minimal SU(5) expects a GUT scale around 10^{16} GeV [76]. In the case of SU(5), there would be $5^2 - 1 = 24$ gauge bosons, which would naturally lead to the decay of the proton with an accidental B-L symmetry [76]. Such a Standard or so-called flipped SU(5) model [77] predicts a proton decay dominated by $p \to e^+\pi^0$ and $p \to \mu^+\pi^0$. One may wonder how such a decay could happen if the Standard Model normally conserves baryon and lepton number, but it turns out that both of these are accidental symmetries of the model. An accidental symmetry is one that is not imposed directly by the gauge choice, but rather is the consequence of imposing gauge invariance and renormalizability with a given particle content [78]. For minimal Supersymmetric SU(5) [79], predicted decay modes involve pseudo-scalar bosons and anti-leptons [80]

$$p \to \bar{\nu}_i K^+,\ \bar{\nu}_i \pi^+,\ e^+ K^0,\ \mu^+ K^0,\ e^+\pi^0,\ \mu^+\pi^0,\ e^+\eta,\ \mu^+\eta;\ i = e,\ \mu,\ \tau \tag{1.62}$$

in the case of Supersymmetric SU(5) the dominate decay mode becomes $p \to \bar{\nu}_i K^+$. Similarly an SO(10) model would predict similar channels for proton decay, but the branching ratios would change such that the two most dominant channels would be $p \to \pi^0 e^+$ and $p \to \pi^0 \bar{\nu}$ [81] [82]. If proton decay via charged modes were to be discovered, then the actual branching ratio would allow us the ability to rule-out and favor certain models.

1.3.2 Effective Field Theory

As a means to understand physics beyond the Standard Model without requiring a specific model in mind, one can use an effective field theory to parameterize the unknown terms in terms of some energy cutoff Λ. This allows for the introduction of non-renormalizable operators into the Standard Model Lagrangian with the understanding that these terms are only valid in the low energy limit (much less than the energy scale Λ of the theory) [78].

$$\mathcal{L}_{full} = \mathcal{L}_H(\phi_H, \phi_L) + \mathcal{L}(\phi_L), \tag{1.63}$$

where ϕ_H are fields describing particles with masses larger than Λ, while ϕ_L are lighter fields. An effective theory, which is equivalent to $\mathcal{L}_{full}$ at low energy, can be defined as

$$\mathcal{L}_{eff} = \mathcal{L}(\phi_L) + \sum_k \frac{C_i}{\Lambda^{k-4}} \mathcal{O}_i^{(k)}(\phi_L) \tag{1.64}$$

where C_i is a dimensionless coefficient and $\mathcal{O}_i^{(k)}$ are local operators of mass dimension k [78]. It is now possible to add non-renormalizable operators to the Lagrangian with the knowledge that the effective Lagrangian L_{eff} is only valid at low energies and must be replaced with a full Lagrangian in order to be valid at higher mass. Dimension 5 and dimension 6 operators can now be added to the Standard Model—with the assumption that these terms must be suppressed—and should be the first hint of physics beyond the Standard Model. For dimension 5, there turns out to be a single operator which is invariant under the Standard Model gauge symmetry [78]:

$$\mathcal{L}_5 = -\frac{C_5^{ij}}{\Lambda} \frac{v^2}{2} (\bar{\nu_L^i})^c \nu_L^j, \tag{1.65}$$

which is a Majorana mass term for left-handed neutrinos. At dimension 6 one finds many more operators become available, though the ones of interest are those related to breaking accidental symmetries of the Standard Model—that would allow experimental observations of those operators. Included in these are operators of the form [28] [83]

$$\frac{qqql}{\Lambda^2}, \tag{1.66}$$

which allow for the transition from baryon to lepton with a global $U(1)_{B-L}$ symmetry, leading to the decay of the proton.

1.3.3 Extra Dimensions

Another mechanism proposed for completing the Standard Model is the introduction of extra dimensions in some form or another. These extra dimensions can either behave exactly as the usual spacial dimensions or have more limiting effects. Such theories date back to the 1920's with work by Kaluza and Klein [84] [85], with introduction of a single extra spacetime coordinate. This idea evolved into more complicated forms such as string theory, where such dimensions were compactified at a scale close to the Planck

scale, making them not observable at experimental levels [30]. Universal extra dimension theories developed in which all fields propagated in the extra dimensions, but further restrictions by Arkani-Hamed, Dimopoulos and Dvali [86] showed that if you can restrict these fields to only allow gravity to propagate through, then you could both explain the weakness of gravity and produce observables at the TeV scale. Another model is the Randall-Sundrum model [87] in which a five-dimensional Anti-de Sitter spacetime could be warped in such a way that the extra dimension was universal, but due to its geometry, would still explain the weakness of gravity and also have a compactification scale in the TeV range [88]. Extra dimension theories are also not constrained to a particular gauge, and are often postulated on unified gauge fields or minimal extensions to the Standard Model each predicting various decays at observable energy scales. Of particular interest (especially to this dissertation) are those which predict the decay of protons via modes which are normally suppressed in 4-dimensional gauge theories.

1.3.3.1 Invisible Decay Models

Consider the model presented by Mohapatra and Perez-Lorenzana [89] in which a 6-dimensional universal extra dimension model with a low scaling parameter (Λ) is consistent with small neutrino mass, suppressed proton decay, and local $B - L$ symmetry. Suppression of proton decay through standard modes such as $p \to e^+\pi^0$ are required due to the large experimental limits already set. If one tries to suppress these modes through the same scale factor, then that scale factor must be large (GUT scale); however, in a 6-dimensional universal model–where all the Standard Model fields reside on all dimensions, proton decay is suppressed with a TeV scale factor [90]. This occurs because the extra space-time dimensions provide a new U(1) symmetry under which the Standard Model fermions are "charged". As is shown in [91], a 6-dimensional model based on the gauge group $\mathrm{SU}(2)_L \times \mathrm{U}(1)_{I3R} \times \mathrm{U}(1)_{B-L}$ compactified[4] on a T^2/Z_2[5] orbifold produces

[4]Compactifying a dimension forces that dimension to have finite length (thus the compactness) by having either physical cutoffs or periodicity

[5]T^2 is the two dimensional Torus, and Z_2 is the discrete rotation (cyclic) group of order 2.

the above effects while also introducing new interesting decay modes:

$$\begin{aligned} n &\to \nu\bar{\nu}_s\bar{\nu}_s, \\ n &\to \pi^0\nu_e\bar{\nu}_s\bar{\nu}_s, \\ n &\to \pi^+e^-\bar{\nu}_s\bar{\nu}_s, \\ p &\to \pi^+\nu_e\bar{\nu}_s\bar{\nu}_s. \end{aligned} \tag{1.67}$$

The above are a consequence of the symmetry of the orbifolds under $B-L$, such that the full symmetry is actually $3\Delta B + \Delta L_{sm} + \Delta L_{\nu_s} = 0$ where L_{sm} are lepton flavor numbers under the Standard Model and L_{ν_s} are the sterile neutrino flavors. From this symmetry it is clear that the lowest order terms must involve 3 quarks and 3 leptons. Here a sterile right-handed neutrino ν_s is required in order to provide mass in accordance with neutrino oscillation experiments. Majorana mass terms under this model are forbidden due to the local $B-L$ symmetry, leaving us only with a Dirac mass term. Furthermore terms of the form $(\psi_L\phi)^2/\Lambda$ forbidden (which for a non-GUT Λ would predict a heavy neutrino), leaving us with [89],

$$\frac{\lambda}{\Lambda^5}\psi_L^T C^{-1} N_L \phi(\chi^*)^2, \tag{1.68}$$

where N_L is the singlet field corresponding to the sterile neutrino, λ is the Yukawa coupling, ψ_L is the usual lepton doublet, ϕ is the Higgs doublet, and χ is a new Higgs singlet (under $\mathrm{U}(1)_{B-L}$). By forbidding the lower dimensional Lagrangian terms, the dimension 9 operator left over can have a small mass scale ($\Lambda \sim 1-10$ TeV) which results in a naturally small neutrino mass [6].

1.3.4 Nucleon Decay Detection

Proton and nucleon decay provide a unique look into physics beyond the Standard Model by probing the low energy effects of high scale processes or possible low-scale compactification. Detecting such a rare process requires experiments which can look for decays over a long integration time while also having a very large sample size to measure with. Decay processes for GUT scale interactions ($\Lambda \sim 10^{16}$ GeV) are suppressed by the scale

[6] For $\Lambda = 10-100$ TeV $\sim 10^3 v$, one finds a neutrino mass roughly $m_\nu \sim 10^{-(10 \text{ to } 15)} v \sim$ eV without requiring fine-tuning of the Yukawa coupling to neutrinos, where $v = 246$ GeV is the vacuum expectation value [30].

factor and would thus cause the proton lifetime to be in the range 10^{30} to 10^{36} years depending on the particular model [74]. In order to reach into this range of sensitivity, one requires a very large detector that can run for a very long time with minimal backgrounds that could mimic the signal. Due to these requirements, neutrino detectors also make for very good nucleon decay detectors as they often satisfy this very condition. The Super-Kamiokande detector, for example, is a water Cherenkov detector containing 50 ktons of pure water (very large), is located at a depth of 2700 meters water equivalent (low background), and has been running since 1996 (long time)[92]. Their current limit on proton decay via the charged modes one would expect from SU(5) and SO(10) models are [53],

$$\begin{aligned} \tau(p \to e^+\pi^0) &> 1.6 \times 10^{34}\text{years}, \\ \tau(p \to \mu^+\pi^0) &> 7.7 \times 10^{33}\text{years}, \end{aligned} \tag{1.69}$$

as well limits on trilepton modes decay schemes [93],

$$\begin{aligned} \tau(p \to e^+\nu\nu) &> 1.7 \times 10^{32}\text{years}, \\ \tau(p \to \mu^+\nu\nu) &> 2.2 \times 10^{32}\text{years}, \end{aligned} \tag{1.70}$$

to 90% confidence level. Each of the charged modes with theory predicted ranges are shown on figure 1.12. These decays deposit a large amount of energy due to the mass differences involved ($p - e = 937.8$ MeV, $p - \mu = 832.6$ MeV, ν is negligible [30]) making them easily detectable and higher in energy than radioactive backgrounds (though susceptible to muon backgrounds). To look for "invisible" modes of nucleon decay a different approach is required. Note here the term invisible is used to remark on the amount of kinetic energy deposited within a detector, which for a decay like $n \to 3\nu$ is effectively zero due to the difficulty in measuring the neutrinos. In the case of a single neutron decaying in vacuum via this mode there would not be a measurable signature; however, if the decay occurs in the nucleus of an atom, then the de-excitation of the daughter nucleus would present a measurable signal, though that signal would be of order MeV due to being a purely nuclear physics process. There have been three searches for such a signal, starting with Borexino [94] and SNO [95] and finally the KamLAND [96] setting the best limits on both,

$$\tau(n \to \text{invisible}) > 5.8 \times 10^{29}\text{ years}, \tag{1.71}$$

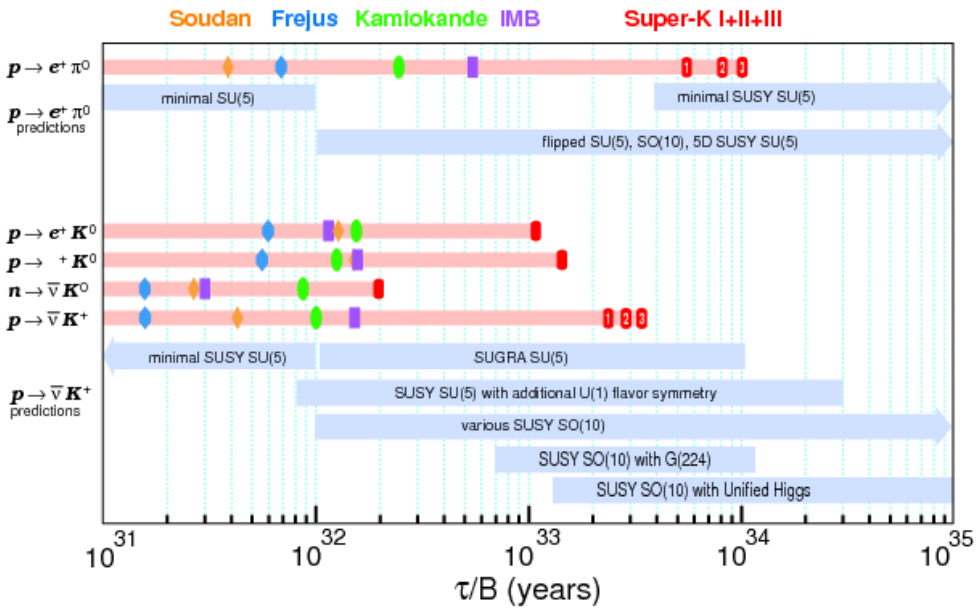

Figure 1.12: Overview of the status of charged proton decay modes with theoretically predicted bounds [13].

and

$$\tau(nn \to \text{invisible}) > 1.4 \times 10^{30} \text{ years}, \tag{1.72}$$

at 90% confidence level. SNO further went on to exclude

$$\tau(p \to \text{invisible}) > 2.1 \times 10^{29} \text{ years}, \tag{1.73}$$

with each of the measurements being done in a theory agnostic way.

Detection of invisible mode neutron decay relies on the nuclear physics of the deexcitation of the daughter nucleus in the decay. In water, this process may occur in the Oxygen nucleus, converting $^{16}\text{O} \to {}^{15}\text{O}$. This requires knowledge of all of the dominant nuclear levels and their branching ratios in order to determine a lifetime. To be consistent with the same measurement made by SNO [95] , the same branching ratios are used which were calculated by H. Ejiri [23], summarized in table 1.5. Decays which are directly to ground state are of no interest due to the lack of an observable signal; however, two decays to excited states would be observable. The first, and most important, is the decay of a neutron from the $P_{3/2}$ shell, leaving the remaining ^{15}O in an excited state which deexcites through the emission of a 6.18 MeV γ. This mode has a branching ratio

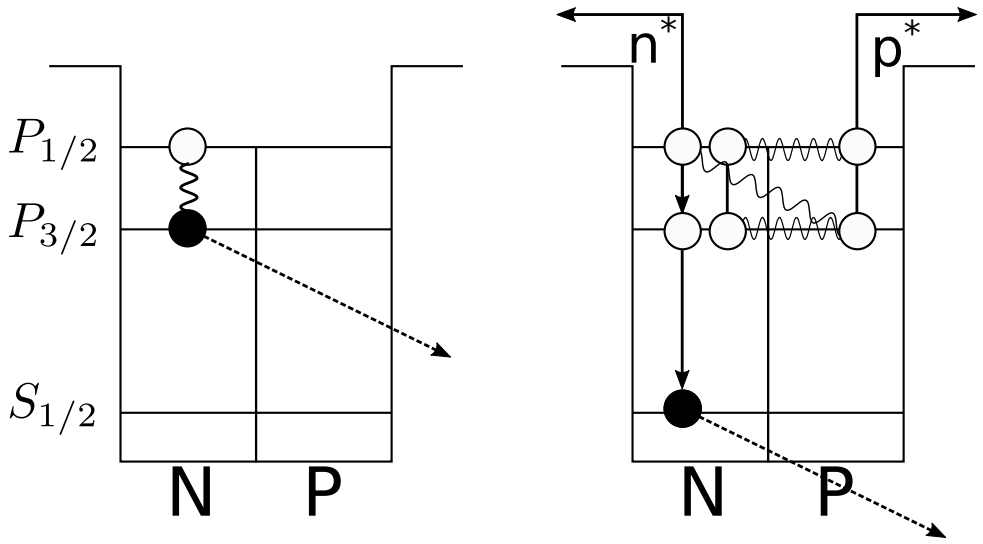

Figure 1.13: Deexcitation scheme for a neutron hole in ^{15}O for the γ emitting modes. The left mode emits a 6.18 MeV γ and the right mode emits a 7.03 MeV γ.

Hole	Residual	States	(k)	E_γ	E_p	E_n	B(k)
$(p_{1/2})_n^{-1}$	g.s.	$\frac{1}{2}^-$	^{15}O	0	0	0	0.25
$(p_{3/2})_n^{-1}$	6.18	$\frac{3}{2}^-$	^{15}O	6.18	0	0	0.44
$(s_{1/2})_n^{-1}$	g.s	1^+	^{14}N	0	~ 24	0	0.02
$(s_{1/2})_n^{-1}$	7.03	2^+	^{14}N	7.03	~ 17	0	0.02
$(s_{1/2})_n^{-1}$	g.s.	$\frac{1}{2}^-$	^{13}C	0	$\sim 14.5 + 1.6$	0	0.01
$(s_{1/2})_n^{-1}$	g.s.	0^+	^{14}O	0	0	~ 18	0.02
$(s_{1/2})_n^{-1}$	g.s.	$\frac{1}{2}^-$	^{13}N	0	2.0	~ 11.5	0.02
$(j)_n^{-1}$	others			$\leq 3-4$			0.22

Table 1.5: Table of ^{16}O invisible neutron decay schemes take from H. Ejiri [23].

of 44%, providing the best sensitivity to neutron decay. The second decay mode has a branching ratio of 2%, giving a small but non-negligible contribution. The second mode is a decay from the $S_{1/2}$ shell followed by a proton emission leaving an excited state of ^{14}N which emits a 7.03 MeV γ. A diagram of these two deexcitation modes is shown in figure 1.13. The sum of these two signals is the signature used to search for this decay mode in SNO+.

Chapter 2

SNO+ Detector

As the name would suggest, SNO+ is an upgrade to the previously existing SNO experiment. There are quite a few major benefits to the reuse of an existing detector (other than the obvious monetary savings), which include familiarity with the electronics and known sources of backgrounds. The SNO detector was originally filled with heavy water (D_2O) as a target volume with light water shielding. SNO+ aims to first fill with light water and then with ^{130}Te doped liquid scintillator, so modifications to the original detector were required in order to accommodate the new materials. Additionally modifications to the SNO electronics and data acquisition hardware were made in order to improve the sensitivity to $0\nu\beta\beta$ and prepare for the increased light output and event rate of liquid scintillator.

2.1 Detector Description

The SNO+ detector is designed to look for rare events which are expected to either occur at a very low rate or not at all. Rare event searches require a detector which has very low background rates and well understood background signals in order to successfully extract the signal. This is achieved through the use of large volumes of buffer regions to provide shielding from external radiation, clean materials within the detector to minimize internal radiation, and deep underground facilities to shield from cosmic rays. The experiment will begin by using water as the primary medium before filling with liquid scintillator for the second phase. The initial water fill provides measurements of the background rates independent of the scintillator as well as characterization of detector components which can be used to estimate the background contributions during the tellurium loaded scintillator phase.

2.1.1 SNOLAB

The SNO+ experiment is located at SNOLAB, which was originally designed to hold the SNO experiment but has since expanded to be a general purpose underground laboratory which is home to PICO, DEAP-3600, HALO, SNO+, MiniClean, and soon to be SuperCDMS [97]. The lab is located in the Vale Creighton mine, near Sudbury, Ontario, at a depth of 2070 meters. At this depth the rate of cosmic muons is reduced from 1.67×10^{-2} $\mu/\text{cm}^2/\text{s}$ at the surface to 3.1×10^{-10} $\mu/\text{cm}^2/\text{s}$ [98]. At this rate, the number of muons going through the detector volume is around 3 per hour. The SNOLAB facilities also provides a clean environment and space for the detector, its electronics, as well as room for a distillation plant to process the liquid scintillator. By maintaining a high level of cleanliness through the construction and running of the detector, background radiation from Uranium and Thorium daughters present in the mine dust is reduced.

2.1.2 Detection Media

The multi-phase design of SNO+ requires understanding the detector response with both water and liquid scintillator, which each have their own advantages and disadvantages described below. The largest difference, which required the above mentioned electronics

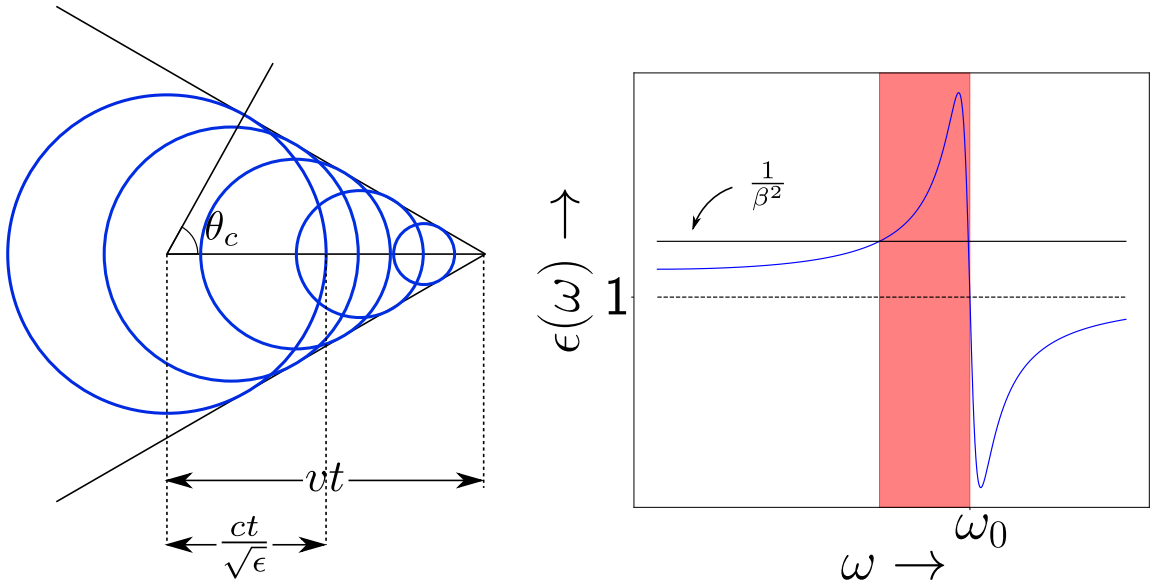

Figure 2.1: **Left:** Cherenkov radiation showing the formation of a shock front from spherical wavepackets emitted by a particle moving at velocity $v > c/\sqrt{\epsilon}$. **Right:** Frequency dependence of the dielectric constant, with the shaded region satisfying the Cherenkov condition $\epsilon(\omega) > \beta^{-2}$. Figure drawn based on results from [14].

upgrades, is the nearly two orders of magnitude difference in light-yield between them. One major benefit to this design is that the data and characteristics of the water phase (which should match SNO data very well in terms of detector response) can be used as a means to characterize the detector independent of the scintillator data.

2.1.2.1 Water

During the first phase of the experiment, SNO+ was filled with ultra pure water in both the Acrylic Vessel and the cavity. The primary means of detection in water is through Cherenkov radiation, whereby a charged particle moving at a speed faster than the speed of light in a particular medium produces ionizing radiation in a well defined pattern and frequency. This process can be explained through classical relativistic electrodynamics by considering the energy loss of a particle through a medium whose density effects cause coherent light emission (described by the dielectric constant $\epsilon(\omega)$). One finds that the energy loss in matter is given by [14],

$$\left(\frac{\mathrm{d}E}{\mathrm{d}x}\right)_{b>a} = -ca\mathrm{Re}\int_0^\infty B_3^*(\omega)E_1(\omega)\,\mathrm{d}\omega\,, \tag{2.1}$$

where the impact parameter b is larger than the hard collision distance a, and $B_3(\omega)$ and $E_1(\omega)$ are functions of modified spherical Bessel functions. In the limit $\beta^2 > 1/\epsilon(\omega)$ which is equivalent to,

$$v > \frac{c}{\sqrt{\epsilon(\omega)}}, \tag{2.2}$$

one finds that equation 2.1 simplifies to

$$\left(\frac{\mathrm{d}E}{\mathrm{d}x}\right)_{rad} = \left(\frac{ze}{c}\right)^2 \int_{\epsilon(\omega)>(1/\beta^2)} \omega\left(1 - \frac{1}{\beta^2\epsilon(\omega)}\right) \mathrm{d}\omega\,, \tag{2.3}$$

giving an expression for the energy loss of a relativistic charged particle where e electron charge and z is the total number of charge (1 for an electron, -1 for a proton, -2 for an α, etc.). A key characteristic of Cherenkov radiation is that the emission spectrum is not flat, but rather peaked at higher frequency below the region where $\epsilon(\omega) > \beta^{-2}$, which for water causes the radiation to be peaked in the blue-violet regime. When accounting for resonant absorption and anomalous dispersion one finds that the dielectric constants dependence on ω,

$$\epsilon \propto \frac{\omega_0^2 - \omega^2}{(\omega_0^2 - \omega^2)^2 + \gamma\omega^2}, \tag{2.4}$$

where ω_0 is the resonance, and γ is a small damping term. This is illustrated on the right side of figure 2.1. The second key characteristic of Cherenkov radiation is that due to the fixed speed of light, the particle emitting the Cherenkov radiation is creating a shock front of light producing the well known Cherenkov angle as shown in figure 2.1. The angle at which this light is emitted is given by the Cherenkov angle θ_c,

$$\cos\theta_c = \frac{1}{\beta\sqrt{\epsilon}}, \tag{2.5}$$

which for a light particle (such as an electron) moving through water ($\beta \sim 1$ and $\epsilon \sim n^2$ where n is the refractive index) one finds the Cherenkov angle,

$$\theta_c = 41.4^\circ \quad \text{(water)}. \tag{2.6}$$

In a physics experiment it is simplest to measure the sum of the entire spectrum by counting the total number of photons detected. From the total light yield one is able to estimate the energy of the incident particle, and due to the shape of the Cherenkov

radiation, one can further determine the direction the particle was traveling. This strong directionality is a huge advantage in favor of water Cherenkov detectors. The energy loss given in equation 2.3 can be transformed into a total photon emission count by substituting $\frac{\mathrm{d}E}{\mathrm{d}x} = \frac{\mathrm{d}N}{\mathrm{d}x}\hbar\omega$ where N is the number of emitted photons. For a charged particles moving through matter, the energy loss due to Cherenkov radiation is a subdominant effect, where the Bethe equation [30] (which includes loss due to collisions) predicts the majority of the energy loss. For an electron in the range of nuclear interactions, energy loss is dominated by ionization, and one finds that an electron in the 1-10 MeV range will travel roughly 0.5 cm / MeV, emitting ~ 100 photons per MeV as Cherenkov radiation.

2.1.2.2 Scintillation

The primary advantage of scintillation light over Cherenkov radiation is a much higher total light-yield. A liquid scintillator can often emit up to 10,000 photons per MeV of deposited energy from an electron, which correlates directly into a better energy resolution at the cost of directional information. The basic mechanism behind organic scintillators arises from transitions in the energy level structure of single molecules. Light emission from molecules is broken into two regimes: fluorescence, and phosphorescence. Fluorescence occurs through the deexcitation of electron singlet states, which are short-lived states that produce prompt light. Phosphorescence occurs when the molecule undergoes inter-system crossing, converting excited singlet states into triplet states, which must decay to the ground state (singlet) through a forbidden transition. The result is a phosphorescence emission which can be significantly delayed as compared to fluorescence. Scintillator experiments ideally choose compounds which have a short lived triplet state, one which is only slightly longer than the fluorescence transition, in order to improve timing resolution and avoid event pileup from late light[1]. As shown in figure 2.2, the energy levels for organic molecules can be broken into singlet state transitions $S_0, S_1, ...$ with small energy splittings from molecular vibrational modes, denoted $S_0 0, S_0 1, ...$ Vibrational modes can transfer kinematically from molecule to molecule as well as become activated through absorption or most importantly, through the excitation of charged parti-

[1] Late light is emitted slowly after the initial excitation due to long-lived excited states of the molecule.

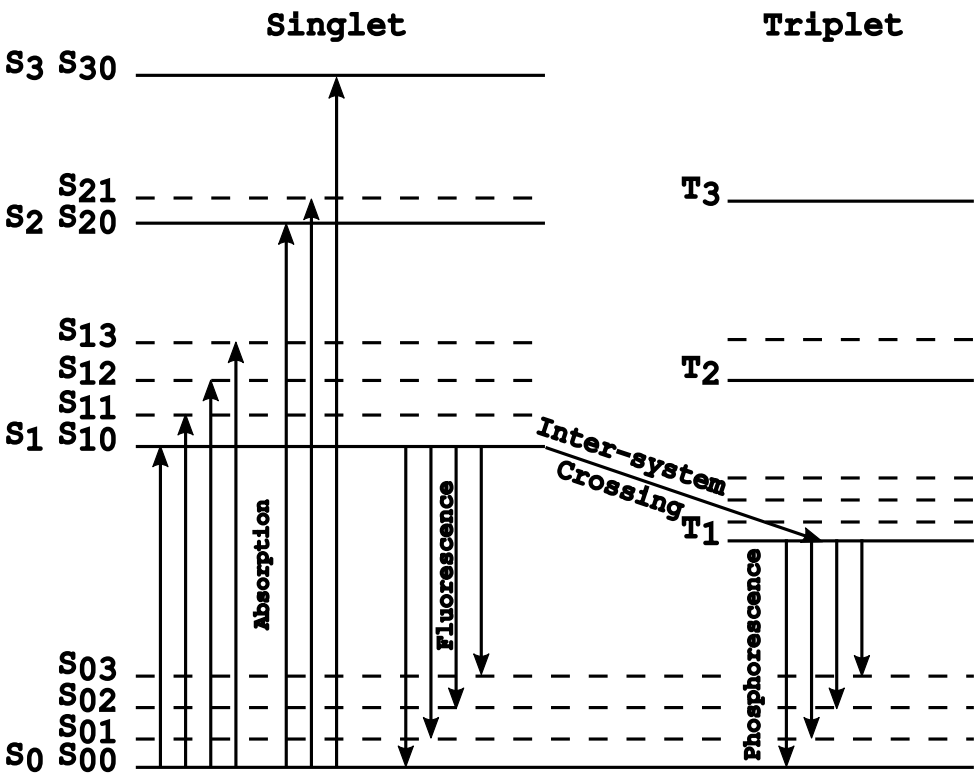

Figure 2.2: Example energy levels of an organic molecule depicting the difference in absorption, fluorescence, and phosphorescence lines from [15].

cles passing by. Ultimately this allows the excitation of the molecules through the transfer of kinetic energy from charged particles, which is then emitted as light through fluorescence and phosphorescence. In many materials the absorption spectrum and the emission spectrum overlap; however, in materials generally referred to as scintillators, the deexcitation to vibrational modes allows the molecule to emit light which is of lower energy than the molecules absorption lines, allowing for the scintillation light to pass through unhindered. The deexcitation time can easily be modeled with a decay equation in terms of the lifetime τ of the state as:

$$I = I_0 e^{-t/\tau}, \tag{2.7}$$

of which the integral of the intensity I would give you information on the total energy absorbed by the scintillator (and thus the energy deposited by the incident particle). Unfortunately the efficiency of the conversion from deposited energy to light emission is reduced by other possible de-excitation modes available to the molecule which do not

produce light, referred to as quenching. The term quenching is a catch-all used to group together all non-light producing processes, which are often caused by impurities in the scintillator, and loss of energy due to heat. Birk's law gives an empirical formula for the energy loss of an incident particle through a scintillator, taking into account the scintillator efficiency A, and quenching effects through Birk's constant k_B [99],

$$\frac{\mathrm{d}S}{\mathrm{d}r} = \frac{A\frac{\mathrm{d}E}{\mathrm{d}r}}{1 + k_B\frac{\mathrm{d}E}{\mathrm{d}r}} \tag{2.8}$$

One of the best ways to overcome quenching is by making the scintillation modes extremely favorable by the introduction of an efficient scintillator (often called the fluor) into a mix of bulk solvent. The bulk solvent will absorb the incident energy of the particle, then quickly transfer the energy to the efficient scintillator, which will then emit the light as fluorescence and phosphorescence. The secondary benefit of using a small quantity of fluor in a bulk solvent is that self absorption in the material is, which typically only occurs on the fluor, is highly suppressed by the low abundance [100] [101].

The SNO+ liquid scintillator consists of linear alkylbenzene (LAB) as a bulk solvent which is mixed with 2,5-diphenyloxazole (PPO) at a ratio of 2 g PPO per liter of LAB. This particular mixture was chosen for several reasons. Compared to some other liquid scintillator solvents, LAB is relatively safe with a low toxicity and has a high auto-ignition temperature ($229°C$ [102]), which is ideal when attempting to purify underground. LAB also comes with very little impurities straight from the manufacturer, easing the burden on the purification system. As a scintillating medium, the mixture of LAB and PPO has both an ideal timing profile with a short lived triplet state, and a long attenuation length. Measurements of the timing profile for both α and β particles were measured and fit using three exponentials individually convolved with a Gaussian,

$$\sum_{i=1}^{3} A_i \exp\left(\frac{x}{t_i} + \frac{0.25}{\sigma t_i^2}\right)\sqrt{\frac{\pi}{4\sigma}}\left[1 + \mathrm{Erf}\left(\sqrt{\sigma}\left(-x - \frac{0.5}{t_i\sigma}\right)\right)\right] \tag{2.9}$$

where A_i is an overall scaling factor, t_i is the timing component for time x, and σ is the timing resolution (determined to be 1.9 ns for this measurement). Given these parameters,

	Oxygenated α	Oxygenated e^-	Deoxygenated α	Deoxygenated e^-
t_1 (ns)	4.4 ± 0.2	4.3 ± 0.3	3.2 ± 0.2	4.6 ± 0.3
t_2 (ns)	20 ± 1	16 ± 1	18 ± 1	18 ± 1
t_3 (ns)	178 ± 10	166 ± 11	190 ± 10	156 ± 9
A_1	520 ± 6	768 ± 12	794 ± 7	753 ± 14
A_2	59 ± 3	59 ± 4	53 ± 3	61 ± 3
A_3	3.3 ± 0.1	0.8 ± 0.1	12.6 ± 0.2	2.2 ± 0.1
R_1 (%)	55	75	44	71
R_2 (%)	28	22	16	22
R_3 (%)	17	3	41	7

Table 2.1: Summary of timing results oxygenated and deoxygenated LAB+PPO liquid scintillator for α and e^- from [24] using a three exponential fit to the timing profile given in equation 2.9.

the relative contribution of each component is

$$R_i = \frac{A_i t_i}{\sum_{i=1}^{3} A_i t_i}. \tag{2.10}$$

Table 2.1 summarizes the results of the fit for LAB. When accounting for all efficiencies (including detector efficiencies, optical properties, and scintillation efficiencies) the signal per MeV for an electron is predicted to be about 520 detected photons in detector simulations [103]. As will be discussed in a later chapter, a key ingredient in achieving this goal is the SNO+ distillation plant which was built underground adjacent to the detector itself.

2.1.3 Detector Description

The key component of SNO+ is a 12m diameter, 5.5cm thick acrylic sphere which holds the primary detection volume—referred to as the Acrylic Vessel (AV). In phase I of the experiment, this volume will be filled with ultra pure water, which will subsequently be displaced by pure liquid scintillator and then doped with ^{130}Te which undergoes $\beta\beta$ decay. Figure 2.3 illustrates the primary components of the detector relative the SNO+ cavity.

The Acrylic Vessel is held in place by a set of hold-up and hold-down ropes. The

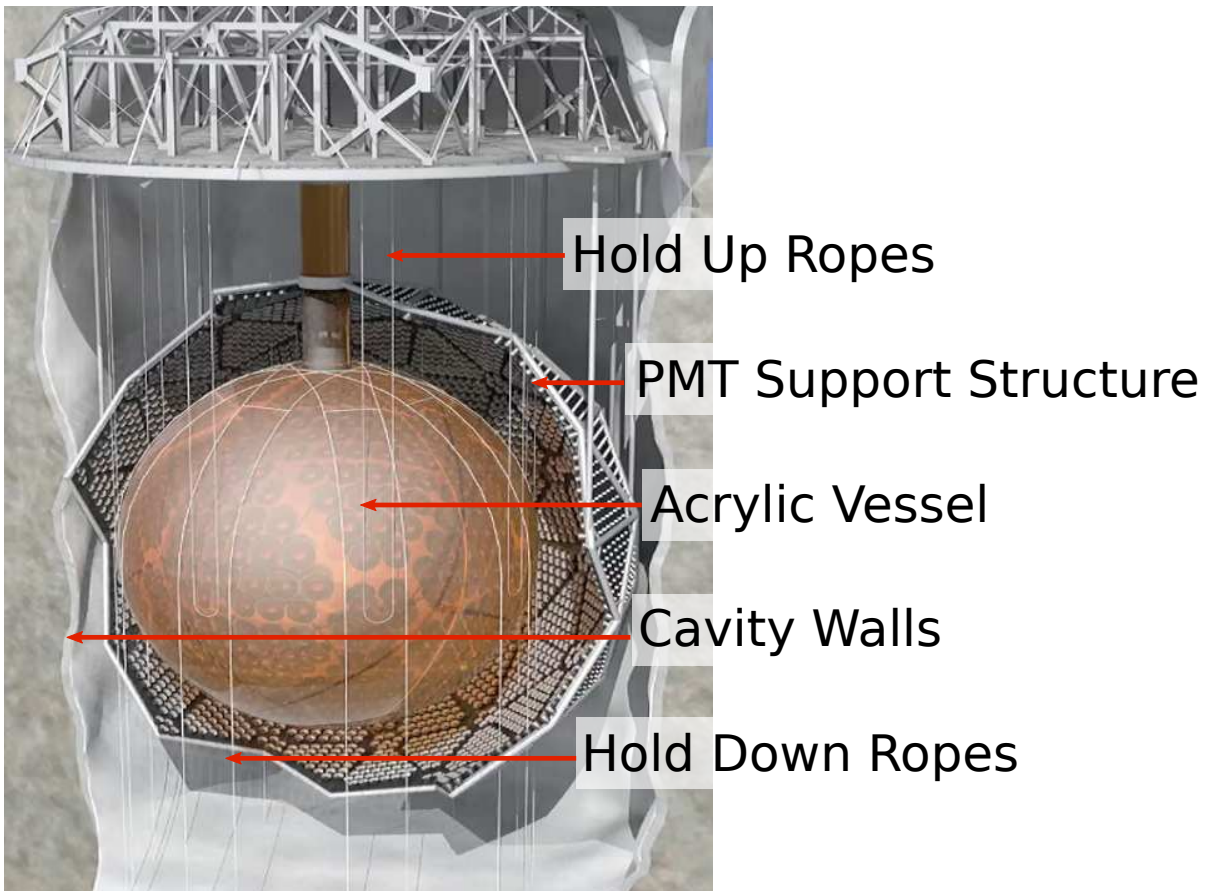

Figure 2.3: Digital rendering of the SNO+ detector [16].

hold-up ropes were initially in SNO because the density of D_2O was such that the vessel would sink in the surrounding light water. SNO+ will fill the Acrylic Vessel with liquid scintillator which has a density near 0.86 g/cm^3, requiring additional hold-down ropes to keep it from floating.

Outside of the Acrylic Vessel is a photomultiplier tube support structure at a radius of ∼8.9 m, which holds in place 9438 20 cm diameter Hamamatsu R1408 photomultiplier tubes (PMT) on a geodesic stainless steel support structure. The PMTs are used to measure the light output of the primary detection medium by detecting and counting single photons. The photons interact with the glass surface of the photomultipliers, which are coated with a photosensitive compound, emitting an electron. The photomultiplier tube consists of a series of dynodes each held at subsequently decreasing potential, and as the electron is accelerated along this potential it smashes into each dynode causing

a shower of electrons to be emitted. This subsequent multiplication of the number of electrons at each dynode will result in an overall gain on the initial electron count of 10^7 (for SNO+ PMTs). The charge deposited by the electrons in this way is readout by the detector electronics and is used in determining the total light within the detector.

Photons emitted by a physics process are not guaranteed to be detected due to loss through physical processes (such as absorption and scattering) as well as detector related effects. To start, the photomultipliers have a somewhat spherical surface and must be packed together at a similar distance from the center of the detector. Both because the cost of PMTs is very high, and perfect packing is difficult to achieve, gaps exist between individual PMTs which can allow photons to escape. The percentage of photons, emitted isotropically within the detector, which would make contact with a PMT photocathode is defined as the photocoverage. The total photocoverage is constrained by the geometry of the detector and how tightly the PMTs can be packed to fit that geometry.

In SNO+ the PMTs are arranged such that the total photocoverage is 31% [104]. As a means to boost the total number of detected photons, 27 cm diameter light concentrators were designed to fit around each PMT. The concentrators consist of 18 pieces of thin dielectric-coated aluminum sheets surrounding the PMT and are curved to deflect photons towards the center of the photocathode. The use of concentrators helps to increase the total photocoverage to an effective 54% after accounting for concentrator reflectivity. In SNO+ this effective photocoverage is expected to decrease as the concentrators degrade over time. Finally, the conversion process of photon to detected signal has an efficiency of around 15% which reduces the total effective coverage to 8%. The PMT support structure resides within an excavated cavity within SNOLAB holding an additional 7 k-tonnes of ultra-pure water shielding. The overburden from the rock provides 5890 ± 94 m.w.e. shielding from cosmic rays, with a measured muon rate of 63 muons/day/8.3m radius circular area [103].

2.1.4 Instrumentation

Photons generated by physics events within the detector will interact with the photocathode of PMTs producing electrons in the PMT base. This signal generated within the

PMTs is then recorded via the detector electronics and digitized with the data acquisition hardware. The purpose of the detector electronics is to record the total charge deposited at each PMT as well as the arrival time of that charge relative to a global clock. This information is used to reconstruct physics events based on the deposited charge and timing of each detected photon within the detector by comparing the results to Monte Carlo simulations.

The SNO+ electronics are adapted from the original SNO electronics [105], with a few major upgrades made in order to accommodate the high data rate expected from a liquid scintillator detector. The original SNO electronics could take data at a maximum rate of 2 Mbit/s, though normal operations were around 15 kbit/s. Since data is a collection of PMT charge and timings, the data rate is proportional to the event rate times the number of PMTs which see light during an event. The light output of liquid scintillator, as shown in the previous section, can be 100 times greater, which would push the data rate near the SNO limit even at the same rate of events. The new electronics are designed to operate up to 250 Mbit/s to account for the greater light yield. The following is an overview of the electronics scheme of the SNO+ detector, with more complete versions found in internal SNO+ documents [17].

The SNO+ trigger system is mostly unchanged from the original SNO design aside from specific upgrades aimed at improving the data rate at which the detector can run. Each PMT is associated with a channel in the electronics, and whenever the charge on that channel goes above a predefined threshold a trigger signal is propagated through the electronics to a single board which determines the total number of triggers in any given 400 ns time window. When enough channels trigger in coincidence then a global trigger is sent to all channels and the charge and time from the triggered channels are digitized and recorded as data.

PMT pulses are first sent to the deck above the detector where 11 racks are distributed circularly above the PMT support structure. Each rack is capable of holding 2 crates, of which 19 crates are used for PMT high voltage, triggering, and PMT data collection. Figure 2.4 shows the flow of the electronics beginning with pulses from the PMTs. The

signal from each PMT is sent to one of 16 PMT Interface Cards (PMTIC), which have 4 paddle cards on board. Each paddle card can support 8 PMTs, resulting in 32 PMTs per PMT Interface Card (thus 512 PMT per rack). The PMTICs form the back-end electronics which controls the high voltage to each paddle card (but not each PMT), and picks off the PMT signal from the high voltage signal to send to the front-end electronics .

Due to this wiring scheme, the 8 PMTs associated with a single paddle card share the same high voltage line, control, and relay. The only way to remove the high voltage to a single PMT is to physically open the circuit to that PMT on the paddle card, otherwise the relay can be opened to disable high voltage to all 8 PMTs on that paddle card without having to physically alter the board. The signals are sent to the Front End Card (FEC), which mirror the paddle cards (each receiving 8 PMT signals). On the FEC 4 signals are generated each time the PMT signal crosses a predefined threshold. The 4 trigger signals are

1. **ESUM Hi** Analog sum of triggered channels with an amplification applied.
2. **ESUM Lo** Analog sum of triggered channels with a lower amplification factor than ESUM Hi.
3. **NHit 100** Digitized pulse which is set to a 100 ns width.
4. **NHit 20** Digitized pulse which is set to a 40 ns width and can be be adjusted to provide individual channel delays. The channel was changed from 20 ns in SNO to 40 ns in SNO+ but the name was never changed.

The purpose of each of these trigger signals is to provide additional information for each recorded event. Both the NHit 100 and NHit 20 trigger produce a fixed height square pulse, which means that each PMT that is over the trigger threshold contributes equally to the summed trigger signal. In comparison, the ESUM triggers are simply analog sums of all of the PMT pulses which exceed threshold, making the individual contributions to the triggers proportional to the deposited charge in each PMT. The transit time for a photon

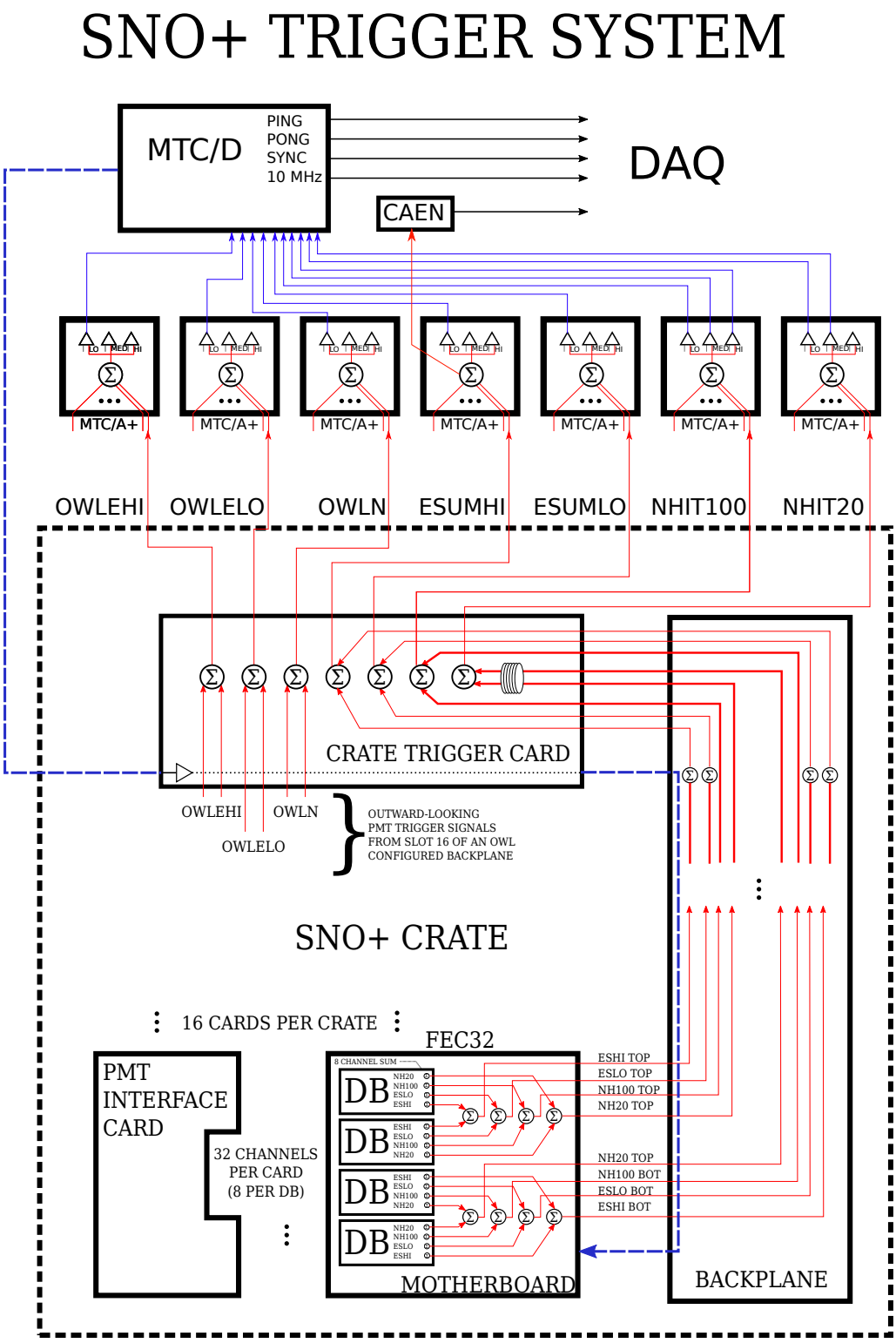

Figure 2.4: Diagram of the SNO+ instrumentation detailing the full trigger system [17].

across the entire detector is around 80 ns, so the NHit 100 trigger allows enough time for light from a single event to propagate through the detector medium and contribute to the trigger signal. This makes NHit 100 the primary trigger signal for physics events in SNO+.

The NHit 20 trigger is designed as a diagnostic tool to isolate events which originate from a fixed region of the detector by selecting for light detected within a 40 ns window. By adjusting the channel delays for the NHit 20 trigger, the selected region can be moved from the center of the detector to any location within the detector.

The ESUM triggers are separated by the gain applied when amplifying the raw PMT pulse with the high gain (ESUM Hi) channel being useful when looking at single photons striking the PMT, and the low gain (ESUM Lo) channel used when PMTs see a very high charge that would typically saturate the ESUM Hi trigger. The ESUM Lo trigger is used when looking for electronic breakdown in PMTs that produce charge well above a normal physics event. The ESUM Hi trigger is digitized and stored with the event data to be used as a means to characterize and remove electronic noise events from the data.

For each of these triggers, the daughter boards sum the outputs from all 8 connected channels and pipe that to the Front End Cards which then perform an additional analog sum before sending the signal to the backplane of the crate. Each crate additionally has a Crate Trigger Card (CTC) at one end, which takes the summed signals from all of the FECs in the crate (with an appropriate time delay) and performs another analog sum. From this point, all of the signals from each CTC in each crate must come together in the Timing Rack which contains 7 Analog Master Trigger Cards (MTC/A+). The MTC/A+ are upgraded versions of the original SNO MTC/A, with the following added advantages [105]:

- New digital logic to remove dead time issues.
- Switched from a current sum to a voltage sum.
- Re-trigger capabilities for tagging backgrounds.

The trigger logic on the MTC/A+ uses a Complex Programmable Logic Device (CPLD)

which allows programming via VHDL[2] to implement a digital trigger scheme. In the purely analog setup, when a global trigger is issued, another global trigger cannot occur again for another 440 ns (the lockout time). The CPLD allows for a channel which crosses threshold during the lockout window to provide a raw trigger signal at the end of the lockout window to help catch low-energy follower events.

Another issue with the previous MTC/A design was that each channel trigger sent 600 μA, which if triggering every channel, could send up to 6 A to the analog trigger. A current limiter used to protect the electronics realistically limited the dynamic range of the trigger system to 2000 PMT hits, which works perfectly well for the low light output of Cherenkov emission, but cannot work with the high light output of scintillator. The MTC/A+ uses operational amplifiers in place of the transistor current mirrors, allowing for the trigger current to be attenuated and trigger based on voltage. This provides a safer trigger signal with a larger dynamic range [106].

There is a single MTC/A+ for each of the trigger types as well as 3 extra which are in place to separately receive triggers from veto PMTs. The SNO+ veto PMTs are referred to as Outward Looking (OWL) PMTs and are situated on the outside of the PMT support structure, facing towards the cavity walls. OWL PMTs look for light that is emitted in the region between the cavity and the PMT support structure which is used to look for muons which travel through the cavity and into the detector. Using the OWL PMTs this way makes it possible to separate these muons from high energy events contained within the detector and act as a muon veto system. The OWL PMTs only produce ESUM Hi, ESUM Lo, and NHit 100 trigger signals, which are sent to the remaining three MTC/A+.

A total of three discriminators on each MTC/A+ can fire based on the sum of the signals input, which each send a signal to the Digital Master Trigger Card (MTC/D) in the same crate. The MTC/D is in charge of telling the data acquisition hardware (DAQ) which triggers are firing, and also sending a signal to every Crate Trigger Card when a global trigger has fired. The Crate Trigger Cards then inform every Front End Card to transmit its PMT data (described below) to the XL3 which exports the data via ethernet

[2]VHSIC (Very High Speed Integrated Circuit) Hardware Description Language

to be stored nearline.

The XL3 is an interface board which directly reads custom "SNOBUS" signals from the Front End Cards in each crate and pushes the data via ethernet to a switch which then forwards the data to the central DAQ computer. The XL3 is a replacement to the SNO XL2/1 system, improving the data readout rate by switching from crate-by-crate readout to simultaneous readout and improved individual bitrate. Compared to SNO's limit of 2 ∼Mbit/s total, SNO+ can achieve a data rate of 13 ∼Mbit/s per crate (∼250 Mbit/s total) [107]. As a way to distinguish between instrumental backgrounds and physics events, there is a CAEN V1720 waveform digitizer which is setup to digitize the ESUM Lo trigger pulses for each event, which can later be used in data cleaning to distinguish instrumental noise from physics events. The specific data recorded for each event is,

1. Trigger types
2. Trigger ID number (GTID or Global Trigger ID)
3. MTC/D Clock Time
4. GPS Clock Time
5. CAEN digitized trigger pulses
6. Hit Information for each triggered channel
    (a) Integrated charges
        i. **QHS** Integrated with high gain over a short interval.
        ii. **QHL** Integrated with high gain over a long interval.
        iii. **QLX** Integrated with low gain over a short interval.
    (b) Hit time (TAC)
    (c) Status flags

A more detailed descriptions of the current electronics can be found in the internal SNO+ documentation [17] [105] [108].

Chapter 3

Detector Backgrounds

When selecting for neutron decay signals, events in the detector which can mimic the signal are considered a background to the experiment. Background processes can either be physical in nature, such as radioactive decay producing γ rays within the detector, or come from noise in the electronics. In order to extract the signal count from the total background, it is necessary to understand and model each background individually. Backgrounds due to physics events within the detector are modeled using Monte Carlo detector simulations. The simulated events are then fit to the data—typically in an energy region where the neutron decay signal does not exist—and used to subtract off the expected background in the neutron decay signal region. Instrumental noise presents an additional background caused by electronic pickup and failures in the instrumentation which are removed through "data cleaning."

3.1 Backgrounds

Backgrounds for all phases of the experiment are very similar and can be split into internal backgrounds and external backgrounds. Internal backgrounds are those which originate from within the detector medium within the Acrylic Vessel; while, external backgrounds consist of events coming from the AV, the water outside the AV, and even external sources of neutrinos. The internal backgrounds can be reduced by imposing strict material cleanliness as well as methods for recirculation and re-cleaning when required. The same is true for external backgrounds which come from the external water; however, radiation from detector components such as the PMTs are fixed as are natural sources of background such as solar neutrinos, and reactor antineutrinos.

3.1.1 Radioactive Backgrounds

Present in all materials are trace amounts of naturally occurring ^{238}U, ^{232}Th, and ^{40}K. Each of these are long-lived with decay chains which are in secular equilibrium as long as new sources of contamination are not introduced while running. For each of these long series, the only decays which could be present as backgrounds within the region of interest for either nucleon decay (in water) or $0\nu\beta\beta$ (in scintillator) are studied in detail. For the water phase, none of the α decays are of concern because the Cherenkov threshold is well beyond decay energies ($E_k \sim 2$ GeV). Similarly due to the large quenching factor for α measured in liquid scintillator, the emitted energy in photons is reduced by about a factor of 10, suppressing the α decays below the region of interest [109]. Therefore in both cases, the β^- decays are the only direct source of contamination. Due to the change in detector resolution from water to scintillator, the importance of individual backgrounds varies. In water all of the β decays are simulated because it's very likely that the tails of the spectra will spill into the nucleon decay signal region through miss-reconstruction, while in the scintillator phase (where the light-yield goes from ~ 8 NHIT/MeV to ~ 250 NHIT/MeV) only decays with a Q-value near or above the ^{130}Te endpoint (2.528 MeV) are important [103]. In the ^{232}Th chain, the primary contribution for the water phase comes from the β^- decay of ^{208}Tl to ^{208}Pb with a Q-Value of 5.00 MeV, with everything else having a minor contribution. In scintillator phase where α particles can be detected, there is

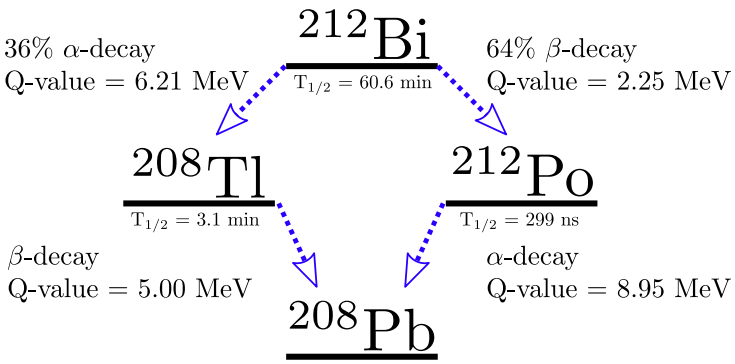

Figure 3.1: Partial ^{232}Th decay series.

further concern with coincidence decays of ^{212}Bi$\rightarrow^{212}$Po$\rightarrow$ ^{208}Tl. These decay paths are shown in figure 3.1 with their relative branching ratios and half lives. Since the half-life of ^{212}Po is 299 ns, the two decays fall within the same trigger window 45% of the time (summing their energies), the total energy of the event falls within the region of interest though separation based on the timing profile is possible [103]. In the ^{238}U chain, both

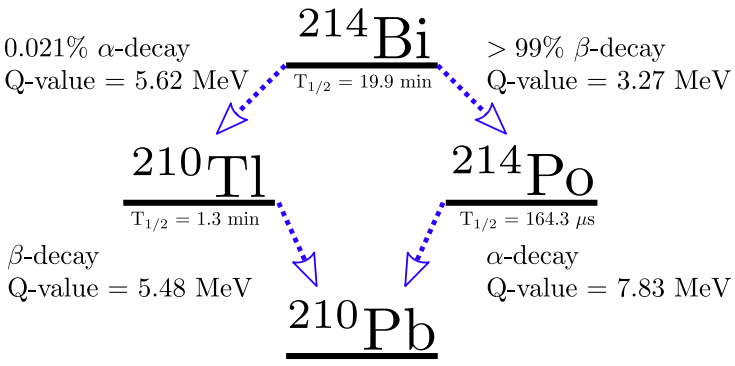

Figure 3.2: Partial ^{238}U decay series.

the ^{214}Bi and ^{210}Tl have high energy β which can reconstruct into the region of interest for water and scintillator phase. ^{210}Tl represents an irreducible[1] background for the water phase analysis; however, it is possible (though difficult) to tag the coincidence—incurring a larger signal sacrifice. The β decay of ^{214}Bi can be tagged reliably in scintillator, and represents another dominant background for the water phase. Figure 3.2 shows the relative branching ratios and energy deposited for these decay modes.

[1]Indistinguishable from signal events when reconstructed.

3.1.2 (α, n) Induced Background

An energetic α emitted from decay can capture on various isotopes to emit a prompt neutron such as

$$\alpha + {}^{13}\mathrm{C} \rightarrow {}^{16}\mathrm{O} + n, \tag{3.1}$$

which is likely to occur in the Acrylic Vessel. A neutron, once thermalized is a background in scintillator due to the 2.2 MeV γ emitted from hydrogen capture as well as the 4.95 MeV γ from carbon capture. In water the hydrogen capture is very difficult to see, and there is very little carbon in the detector so this background is extremely small. However, 10% of the (α, n) results in an excited state of ^{16}O which deexcites emitting a 6.1 MeV γ. The rate of this background is expected to be small, and because they will occur near the Acrylic Vessel, the background is reduced significantly with a fiducial volume cut.

3.1.3 Solar Neutrinos

Solar neutrinos are a dominant background in both the water and scintillator phase of the detector. Shown earlier in figure 1.3, the only solar neutrinos above 2 MeV are ^{8}B and hep ν_e, with ^{8}B being 3 orders of magnitude higher in flux. Unlike SNO which could detect neutrinos through charged current (CC), neutral current (NC), and elastic scattering (ES) [54]

$$\begin{aligned} \text{ES}: &\quad \nu_x + e^- \rightarrow \nu_x + e^-, \\ \text{CC}: &\quad \nu_e + D \rightarrow e^- + p + p, \\ \text{NC}: &\quad \nu_x + D \rightarrow \nu_x + n + p, \end{aligned} \tag{3.2}$$

SNO+ (lacking the deuteron from heavy water) only has to contend with the elastic scattering of the combined flavors ν_x. The solar spectrum shown in figure 1.3 gives the ν_e kinetic energy at production based upon the Standard Solar Model [110]. This spectrum must be oscillated in order to predict the expected solar neutrino background at SNO+. There are three zones of oscillation that can effect the neutrino energy spectrum and total rate corresponding to resonant flavor transition in the solar interior, vacuum oscillations as the neutrinos come towards earth, and matter oscillations through the planet (at night). Oscillations through the solar interior through the so-called MSW

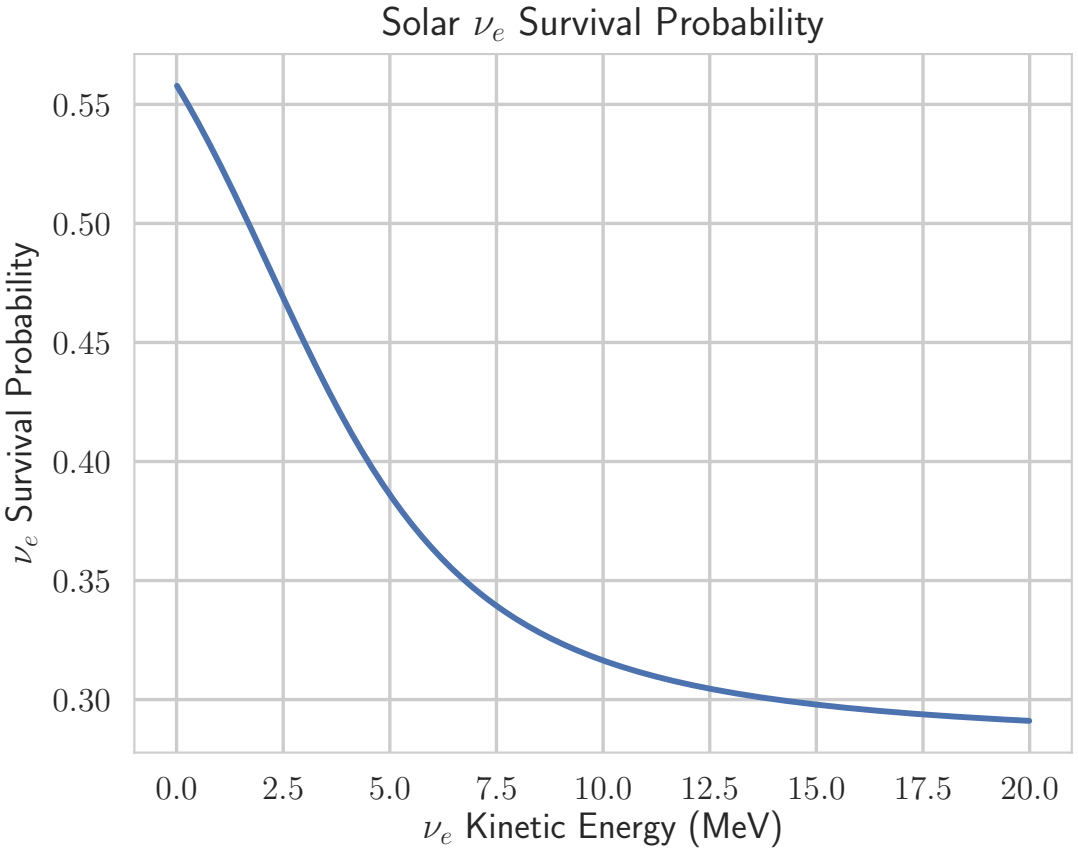

Figure 3.3: Solar neutrino survival probability using the BS05(OP) solar model and the PEM-C earth model for SNO+ courtesy Barros [18].

effect is a resonant transition which occurs due to the weak (force) potential seen by neutrinos as they traverse areas of high electron or nucleon density. This is caused by coherent forward scattering of the neutrinos through the medium analogous to the index of refraction seen by photons through an electric field. The neutrino mass states gain an effective mass based on this potential,

$$\Delta m^2_M = \sqrt{(\Delta m^2 \cos 2\theta - A_{CC})^2 + (\Delta m^2 \sin 2\theta)^2}, \tag{3.3}$$

where $A_{cc} = 2\sqrt{2} E G_F N_e$ for a neutrino of energy E with respect to the weak coupling constant G_F and the electron density N_e. The effective mixing angle becomes,

$$\tan 2\theta_M = \frac{\tan 2\theta}{1 - \frac{A_{CC}}{\Delta m^2 \cos 2\theta}}, \tag{3.4}$$

which has an obvious resonant structure that will maximize the effective mixing angle to $\pi/4$ at densities where $A_{CC} = \Delta m^2 \cos 2\theta$ only in the case where $\cos 2\theta$ is positive[2]. For neutrinos which propagate through a smoothly changing electron density (as is the case in the solar interior), the effect is an adiabatic transition across a large range of energies, with a natural cutoff at the maximum (core) density of the sun given by

$$E < \frac{\Delta m^2 \cos 2\theta}{2\sqrt{2} N_{e-\text{core}} G_F}, \tag{3.5}$$

which for current measurements of the solar mixing angle is about 2 MeV. Below the transition energy, the matter effects reduce to vacuum oscillations, which averaged over the size of the solar core gives

$$P_{\nu_e \to \nu_e} = 1 - \frac{1}{2} \sin^2 2\theta_{\text{sun}} \approx 0.57. \tag{3.6}$$

Around 2 MeV the matter effects begin to take effect and is crossed adiabatically yielding a survival probability

$$P_{\nu_e \to \nu_e} \approx \frac{1}{2} + \frac{1}{2} \cos 2\theta_M \cos 2\theta, \tag{3.7}$$

which slowly transitions into a region dominated by matter effects

$$P_{\nu_e \to \nu_e} = \sin^2 \theta \approx 0.307. \tag{3.8}$$

Figure 3.3 shows the survival probability of solar electron neutrinos as a function of energy, which is used to correct the predicted energy spectrum of solar neutrino interactions in SNO+. The predicted flux of ^{8}B neutrinos given by the Standard Solar Model is,

$$\Phi_{^8\text{B}} = 5.69 \times 10^6 \text{ cm}^{-2}\text{s}^{-1} [32]. \tag{3.9}$$

The interaction cross section for neutrino-electron elastic scattering for the three neutrino flavors is given in terms of the weak mixing angle θ_W and the weak coupling constant G_F as

$$\begin{aligned} \sigma_{\nu_e + e^-} &= (2G_F^2 m_e E_\nu / 4\pi) \left[(1 + 2\sin^2 \theta_W)^2 + \frac{4}{3} \sin^4 \theta_W \right] \approx 95.05 \times 10^{-46} \text{ cm}^2 E_\nu/\text{MeV} \\ \sigma_{\nu_{\mu,\tau} + e^-} &= (2G_F^2 m_e E_\nu / 4\pi) \left[(1 - 2\sin^2 \theta_W)^2 + \frac{4}{3} \sin^4 \theta_W \right] \approx 15.33 \times 10^{-46} \text{ cm}^2 E_\nu/\text{MeV} \end{aligned} \tag{3.10}$$

[2]The effect is reversed for anti-neutrinos because the potential changes sign, causing resonance only when $\cos 2\theta$ is negative.

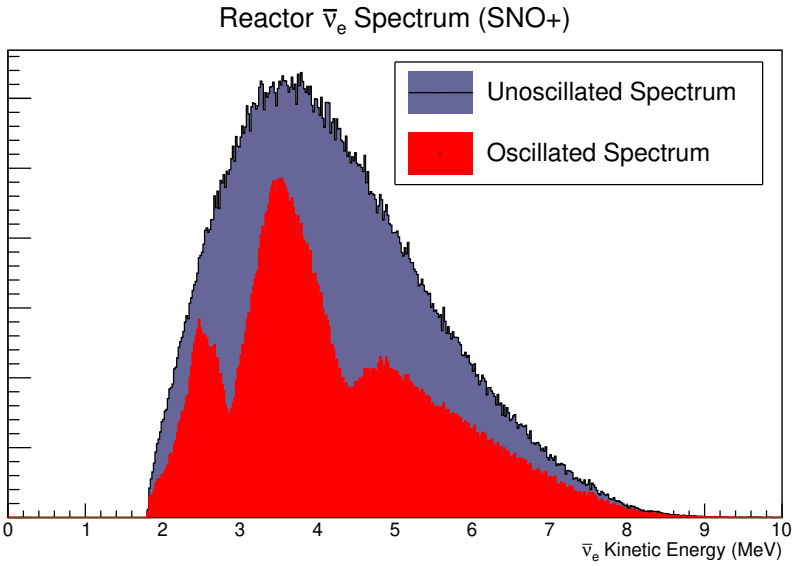

Figure 3.4: Reactor $\bar{\nu_e}$ spectrum predicted in RAT for SNO+ with the leading order reactors. Shown is the oscillated and unoscillated spectra after applying inverse beta decay cross section.

Within the Acrylic Vessel, during the water phase there will be $N_{\nu_e} \approx 5.148 \times 10^{15} \nu_e/s$ going through the detector, which accounting for the cross section and integrating over the ^{8}B spectrum yields an unoscillated rate of 3318 ν_e/year. The detection rate after oscillations will depend on the energy window used for each analysis.

3.1.4 Reactor Antineutrinos

Nuclear power reactors produce a substantial number of $\bar{\nu}_e$ through the various fission processes in their cores, which need to be accounted for as a potential background in SNO+. The expected neutrino spectrum at SNO+ is sensitive to the oscillation parameters used in predicting the expected background count as well as knowledge of the power output and refueling cycles. The dominant fission isotopes used in power reactors are ^{235}U, ^{238}U, ^{239}Pu, and ^{241}Pu and the ratio of these contributions changes as a function of the fuel burning cycle [111]. The buildup of Plutonium is due to the capture of fission neutrons on ^{238}U,

Reactor	Baseline (km)	Power (GW_{th})
Bruce	241	2
Pickering	340	8.2
Darlington	348	8.5
R.E. Ginna	469	1.7
Nine Mile Point	499	5.6
Perry	519	3.2
Point Beach	551	3.5
Davis-Besse	563	2.8
Enrico Fermi	527	2.6
Palisades	614	2.3
Fitzpatrick	500	2.6

Table 3.1: Power and baseline of the leading contributors to reactor anti-neutrinos in SNO+ [25].

$$\begin{aligned} &^{238}\mathrm{U} + n \rightarrow {}^{239}\mathrm{U} \rightarrow {}^{239}\mathrm{Np} + e^- + \bar{\nu}_e \rightarrow {}^{239}\mathrm{Pu} + e^- + \bar{\nu}_e \\ &^{239}\mathrm{Pu} + n \rightarrow {}^{240}\mathrm{Pu} \\ &^{240}\mathrm{Pu} + n \rightarrow {}^{241}\mathrm{Pu}. \end{aligned} \tag{3.11}$$

Antineutrino production in reactors is sensitive to the details of the nuclear cross-sections for these isotopes when calculating the expected spectrum before oscillations are accounted for. Each fission process releases roughly 200 MeV of energy and 6 $\bar{\nu}_e$, which is plotted in figure 3.4 using the given thermal power and baseline in table 3.1 [32]. The detection channel in both phases of the detector is through inverse beta decay,

$$\bar{\nu}_e + p \rightarrow e^+ + n. \tag{3.12}$$

Due to the mass difference of the proton and neutron, the threshold of this interaction is 1.8 MeV ($\sim m_n + m_{e^+} - m_p$). Since the interaction occurs on a proton, which is much heavier than the positron, the positron does not retain most of the directional information of the incident neutrino. The positron will deposit its kinetic energy into the medium through ionization and then annihilate with an electron to produce two 0.511 MeV γ.

Meanwhile, the energetic neutron will spend time thermalizing (kinematically scattering through the medium until it comes into thermal equilibrium with a mean energy of 0.0025 eV). The thermal neutron capture then provides a signal, which if it is detectable, provides a way to tag the reaction. In both liquid scintillator and water (without any kind of neutron capture dopent), the primary capture will occur on hydrogen releasing a 2.2 MeV γ with a mean capture time dependent on the hydrogen density of the material. With a neutron capture cross section of 0.33 barns, the mean time for capture in water is ~ 200 μs (and very similar in liquid scintillator depending on the exact hydrogen composition). In liquid scintillator this γ is very easy to detect and thus provides a very strong coincidence signal; however, in water the efficiency to reconstruct a 2.2 MeV γ is much lower, and thus reactor $\bar{\nu}_e$ present as an irreducible background. The total expected rate of reactor neutrinos in SNO+ before oscillations based on the reactors in table 3.1 is 208 $\bar{\nu}_e$/year.

3.2 Instrumental Backgrounds

Separate from physical background signals, are a unique type of background caused from instrumental noise due to the electronics. These types appear in various forms and from many different causes. The main signature for discriminating these events from data is the unphysical nature of them. "Data cleaning" is the process of cutting non-physics events out of the data with the goal of minimizing both the sacrifice of real physics events to these cuts and the contamination of non-physics events passing the cuts. The following sections outline the various types of instrumental backgrounds seen in the SNO+ detector, the methods used for cutting various backgrounds, and the overall contamination and signal loss, or "sacrifice" from these cuts. One key aspect of data cleaning cuts is that they must be performed prior to event reconstruction, this is to decouple the cuts from reconstruction bias as well as to reduce event processing times. Given the low trigger thresholds in the SNO+ water phase, the instrumental backgrounds are 2-3 orders of magnitude greater in number than physics events, so the savings in processing time is significant. Instrumental backgrounds are not defined by a known set of event topologies, but rather the total set of all events which are not physics. Due to the nature of this definition all possible types of instrumental backgrounds cannot be known, but a subset of these which contains the majority can be found by looking at events by hand and deducing reasonable causes of these instrumentals. When the original SNO detector began running, many of these unknown instrumental backgrounds were investigated in great detail, and this is used as a starting point for developing the data cleaning cuts for the SNO+ water phase. A list of some of the known instrumentals from SNO [112] which are prominent in SNO+ data are:

1. **Flashers:** Events in which the PMTs electrically discharge, emitting light into the detector. Characteristics of a flasher are a high charge cluster of PMTs on one side of the detector, followed by hits on the other side of the detector corresponding to the light emitted. This is shown in figure A.1, with a prominent two-bump CAEN trace from the ESUM trigger.

2. **Neck Events:** Events in which the acrylic neck builds up a static charge which then discharges to create light. The light is transported down from the neck (firing the neck PMTs) and is concentrated at the bottom of the detector.

3. **Bubblers:** Events in which the bubbler tubes (used to measure the water level) produce light right at the acrylic vessel. These are typically very high in NHIT and produce light on par with a muon. Bubbler events always occur along the bottom side of the detector and only produce light inside the support structure.

4. **Wet-end Breakdown:** An electronics breakdown that occurs on the "wet"-end of the high-voltage (near the PMT). Breakdowns often occur in large bursts in which the only means to stop them is for the detector operator to ramp down the high-voltage to that crate and disable the relay to that channel. So-called "friendly" breakdowns can also occur in which a channel appears to breakdown momentarily and then appears to recover (sometimes fast enough that the operator is unaware of the situation). Wet-end breakdowns can also cause large pickup in nearby crates.

5. **Dry-end Breakdown:** Events in which the breakdown occurs in the crate, which does not produce light in the detector, but creates pickup in the crate and rack. Similar to wet-end breakdowns, these often require operator intervention.

6. **Rings-of-Fire:** Due to the location of the DAQ readout in the crate (at the end), pickup from the DAQ can cause the exterior slots in a crate to trigger together.

7. **Slots-of-Fire:** Similar to rings-of-fire, but not restricted to exterior slots.

8. **Flat TAC events:** Events in which the timing distribution of many hits appears random (or flat) across the event window. Often caused by minor wet-end breakdowns, producing light in the detector.

9. **Pickup:** Generic term for events caused by pickup in the electronics. Pickup can come from many sources such as vibrations (someone walking on deck, rockbursts, etc.), or power cycling of nearby electronics.

10. **Sharkfins:** Events in which high charge appears in a single tube, but no light is emitted in the detector. The high light in one channel often causes pickup in the slot that holds it (and sometimes in neighboring slots), and the ESUM trace resembles that of a shark's fin.

11. **Manipulator light events:** Light generated by the motion of the manipulator during calibration runs.

12. **Umbilical light events:** Light generated on or within the umbilical during calibration runs.

13. **Re-circulation light events:** Light generated by the motion of water during re-circulation.

14. **Orphan PMT hits:** "Orphans" are PMT hits which are not placed within the correct event by the DAQ. These hits either cluster together in separate events or are placed individually in the incorrect event.

Most of these events are either due to the geometry and components of the detector or through the electronics itself, giving no reason to expect these to be less prominent in SNO+.

3.3 Data cleaning cuts

Events in the data stream are not actually removed with data cleaning, but rather are flagged as potentially spurious events which should be ignored, or "masked out" when running physics analysis. This is done using three bitwords, the *Applied Mask* which decides which data cleaning words should be processed on events, the *Flagged Mask* which is an event by event status for that event, and the *Analysis Mask* which defines which of the many data cleaning cuts to use for physics analysis. Ideally the *Applied Mask* and the *Analysis Mask* should contain all data cleaning cuts, as long as all the cuts are necessary and working appropriately. As of the SNO+ water phase, the data cleaning bitword also stores the information on event blinding. This was done for ease of use. The bitword used for this analysis is given in table 3.2 using the internal naming convention for each of the cuts. For the water phase analysis, the analysis mask used is 0x7b0000017ffe which includes: zerozerocut, crateisotropy, ftscut, flashergeocut, itctimespreadcut, junkcut, muontag, neckcut, owlcut, qcluster, qvnhit, qvt, ringoffire, tpmuonfollowercut-short, caencut, pollingcut, retriggercut, tpburstcut, missedmuonfollower, missingcaendata, and pedcut. It was decided upon that the logic for events would be to set the *Flagged Mask* bits as

$$\begin{aligned} 1 &= \text{Passes data cleaning (good event)}, \\ 0 &= \text{Fails data cleaning (bad event)}. \end{aligned} \tag{3.13}$$

For final analysis the result is to only use events where

$$(Analysis) \wedge (Flagged) = Analysis. \tag{3.14}$$

The individual cuts used in the analysis mask are described in the following sections.

3.3.1 Zero-Zero

The zero-zero cut is the simplest data cleaning cut which simply removes any event in which the global trigger ID (in hex) ends in 00. This cut is put in place to avoid the effects of a rollover issue with the global trigger registers that will create orphan hits with bad global trigger IDs. Since 00 occurs at the end of sequential events every 256 events, there is an automatic (unbiased) sacrifice of 0.39% of the data from this cut alone [17].

0	prescalecut	22	waterblindlow3	44	missedmuonfollower
1	zerozerocut	23	waterblindlow4	45	missingcaendata
2	crateisotropy	24	waterblindlow5	46	pedcut
3	ftscut	25	waterblindlow6	47	
4	flashergeocut	26	waterblindlow7	48	
5	itctimespreadcut	27	waterblindlow8	49	
6	junkcut	28	waterblindlow9	50	
7	muontag	29	waterblindhigh0	51	
8	neckcut	30	waterblindhigh1	52	
9	owlcut	31	waterblindhigh2	53	
10	qcluster	32	waterblindhigh3	54	
11	qvnhit	33	waterblindhigh4	55	
12	qvt	34	waterblindhigh5	56	
13	ringoffire	35	waterblindhigh6	57	
14	tpmuonfollowercut-short	36	waterblindhigh7	58	
15	tpmuonfollowercut-long	37	waterblindhigh8	59	
16	caencut	38	waterblindhigh9	60	
17	nothingcut	39	thresholdflashercut	61	
18	nhitcut	40	pollingcut	62	
19	waterblindlow0	41	retriggercut	63	
20	waterblindlow1	42	firstevent		
21	waterblindlow2	43	tpburstcut		

Table 3.2: Data cleaning bitmask for the SNO+ water phase. Bits 47-63 are currently unused (saved for later expansion).

3.3.2 Crate Isotropy

The crate isotropy cut targets events that are caused by pickup from the front-end electronics. This cut only using the position of a PMT in "electronic space", defined by its readout location on its corresponding PMT Interface Card. In order to fail this cut, an event has to first have most of its hits within a single crate. Defined as

$$\frac{\text{Hits in any one crate}}{\text{Total Hits}} > 0.7. \tag{3.15}$$

If the event does pass this criteria, it must further exhibit signs of card-to-card or channel-to-channel pickup. Within the crate of interest, two comparisons are made. First a check is made to see if any two side-by-side cards contains more than 80% of hits in that crate, followed by a check if any two side-by-side channels (across all cards) contains more than 70% of the hits. If either of these two is true, then the event is removed from data.

3.3.3 Fitterless Time Spread

The fitterless time spread cut (FTS cut), is designed to look for so-called blind flashers. In the case of a blind flasher, the suspect PMT does not exhibit a high-charge due to its readout being disabled and only the emitted photons can be used to detect and remove the event. This can be separated from true Cherenkov events by looking for a spread in the hit timing which is characteristic of a flasher which will look more sporadic (as opposed to the prompt nature of Cherenkov light). In order to avoid the use of event reconstruction, only the timing of adjacent PMTs is used in the FTS cut. Since hit timing is used as well as hit location this cut is sensitive to PMT calibrations making it slightly less robust than cuts which rely solely on electronic space. The FTS cut works by creating a list of all PMTs which are hit and have good calibration (ignoring the rest), then each hit is compared with every other hit to check for their distance in the detector d and the time difference between their hits Δt. A valid pair is one where,

$$\begin{aligned} \Delta t &< 25 \text{ ns} \\ d &< 3 \text{ m}. \end{aligned} \tag{3.16}$$

One caveat is that PMT hits which are due to pickup in channels near the blind flasher must be ignored. This is done by skipping pairs of hits which are due to a cluster defined

as 3 or more channels in a row in electronic space). As long as

$$\text{Number of valid pairs} > 15, \tag{3.17}$$

the median of the Δt distribution is compared to a median threshold. If

$$\text{Median}[\Delta t] > 6.8 \text{ ns}, \tag{3.18}$$

then the event is flagged by the FTS cut.

3.3.4 Flasher Geometry Cut

With the intent at looking for typical flasher events, the flasher geometry cut looks for a burst of hits nearby (in either electronic or detector space) and compares that to all other hits. Hits are once again compared pair-wise, but in this case uncalibrated hit information can be used. For each hit, the ratio of all hits within 1 meter to total hits is calculated, and if this ratio is greater than 0.5 and the number of hits within the radius is at least 4, then this cluster is considered a possible flasher origin. For each possible flasher origin, if the average hit time inside the cluster is more than 500 TAC counts ($\sim$ 48.8 ns) away from the average hit time outside the cluster or if one of the hits in the cluster is considered a bad hit[3], and the distance between the cluster and average outer hits is $>$ 12 meters, then the event is flagged. If an event passes this criteria, then another check is made in a similar fashion but clusters are looked for in electronic space. In this case the criteria is that a cluster (at least 4 hits) must be within $\pm$8 channels of one hit. If a cluster is found in this way, then the same checks for position and time relative to the cluster are made as before.

3.3.5 In Time Channel Time Spread

The In Time Channel (ITC) Time Spread cut ignores the geometry of events and instead looks only at the timing profile of the hits (which have good calibration). This cut simply slides a 93 ns time window (in 1 ns increments) and calculates the percentage of hits within that window. 93 ns was chosen to match the time window of the NHit 100 pulse (excluding the rise and fall time of the trigger pulse). In practice the ITC cut

[3]Bad hit could be unphysical charge in any of the charge integration channels.

is insensitive to slight changes in the time window length [113]. If the window with the highest percentage of hits contains less than 60% of hits, the event is cut from analysis. This primarily targets flat-TAC events which have a more uniform distribution of hits across time, whereas Cherenkov events will have most hits clustered in time.

3.3.6 Junk

The junk cut is a very simple cut to remove events with anomalous channels being placed within the same event. The cut simply checks that every hit in an event is unique (no PMT contributes more than once), which can happen in the case of an orphaned hit being placed in the wrong event.

3.3.7 Neck

The neck cut specifically targets neck events using data from the neck PMTs. During the SNO+ water phase there were originally 3 PMTs situated in the neck. In order to create room for side-ropes to manipulate the calibration sources along the horizontal axes, one of the neck PMTs was removed. In the simplest case, if 2 neck tubes are hit within an event, then that event immediately fails this cut. If only 1 tube is hit, then additional checks are made to look for the flashlight nature of the acrylic neck, which produces a majority of hits in the bottom half of the detector. If the average time of hits below the equator is more than 85 ns after the neck hit, then the event is flagged.

3.3.8 Owl

Another simple cut is placed on events in which the number of outward looking PMT hits is greater or equal to 3.

3.3.9 Charge Cluster

The charge cluster cut is purely in electronics space and looks for high charge hits that cause pickup in surrounding channels (such as wet-end breakdowns, flashers, and shark-fins). A 5 channel wide sliding window (in PMT id) goes across all channels and if 3 of the channels register a hit, then if any of the hits are considered bad the event is flagged.

3.3.10 QvNhit

The charge vs NHIT cut compares the charge of hits in an event with the total number of hits with the intent in removing events with very little charge in most of the channels. This cut is aimed at low level pickup events which cause many hits just above threshold. Since this cut uses charge information it is important that hits have good calibrations for the cut to be effective. In QvNhit the charge from the lower 90% of hits is summed and then this charge is converted into a total number of photoelectrons (based on the calibration for each channel). If the average number of photoelectrons per channel in this population is less than 0.25, then the event fails.

3.3.11 QvT

The charge vs time cut is yet another cut aimed at targeting flashers using calibrated PMT data if available. This cut is more relaxed than the flasher geometry cut due to only using charge and timing information. QvT looks for the hit in an event with the highest charge in two of the three charge channels (for the water phase QLX and QHL were used). Qualification of high charge is as follows,

$$\begin{aligned} QHL_{\max} - \langle QHL \rangle &\geq 610 \\ QLX_{\max} - \langle QLX \rangle &\geq 110. \end{aligned} \tag{3.19}$$

For each of these two charge channels if the high charge hit came earlier than the median time of hits in the event by

$$60 \text{ ns} \leq \text{Median}[time] - time_{\max} \leq 250 \text{ ns}, \tag{3.20}$$

then the event is flagged.

3.3.12 Ring of Fire

As the name implies, the Ring of Fire cut aims to remove ring of fire events from data. The cut is made using only information in electronics space, so no PMT calibration is needed. To apply the cut, 70% of the hits in the event must be in a single crate, and if so then 80% of those hits must be in the outer ring of the crate. For the water phase the outer ring is defined as cards 0-3 and 12-15 as well as channels 0-7 and 24-31.

3.3.13 CAEN

The CAEN digitizer takes the output of the ESUM trigger signal for the entire event and stores the signal in the data file. This allows for cuts to be made on the shape and size of the ESUM trigger based upon expectations from normal events. This has the potential to provide high levels of discrimination for various event types (for example, as is shown in the flasher example A.1, the CAEN trace has two humps corresponding to the initial flash and the light detected on the other side of the detector). As of the water phase, only the peak height and integral are being used. Shown in figure 3.5 are the bounds that a good event must satisfy, else the event is cut out of the data. These bounds are chosen to provide a 99% coverage across the ^{16}N calibration run, with corrections made at low hit where pedestal noise becomes comparable to the peak height [114],

$$a(1 - S(x)) + S(x)(b + cx) \tag{3.21}$$

where,

$$S(x) = \frac{1}{e^{-(x-T_{NHIT})/T_w} + 1}, \tag{3.22}$$

is the Sigmoid function. The Sigmoid is used to parameterize the transition of small amplitude events (low NHIT) into the noise and is tuned using random trigger events (PulseGT in SNO+). T_{NHIT} shifts the Sigmoid to the NHIT at which the CAEN signal transitions out of the noise and T_w adjusts the width of that transition. The constants define the linear components of the fit where a controls the baseline at low NHIT, b controls the high NHIT offset, and c is the slope at high NHIT. Notice that outside of the noise range ($S(x) \to 1$), the boundaries are simply defined by the line $(b + cx)$. For SNO+ water phase the values of these constants are given in table 3.3.

3.3.14 Muon Followers

Due to the depth of SNO+, the low muon rate allows for a long time cut to be made after muons without a significant impact on the live time. At a muon rate of ~ 3 through the detection volume per hour, a data cleaning cut is applied to every event for 20 seconds following each muon, resulting in the loss of 1 minute of data each hour. This time window suppresses the vast majority of cosmogenic induced radioisotopes and spallation

	T_{NHIT}	T_w	a	b	c
Peak (lower bound)	15	5	6.6	5.1	0.45
Peak (upper bound)	15	5	73.4	54.14	1.34
Integral (lower bound)	15	5	−834.0	−707.0	−15.9
Integral (upper bound)	15	5	720.6	658.8	−6.61

Table 3.3: CAEN Cut constants for SNO+ water phase.

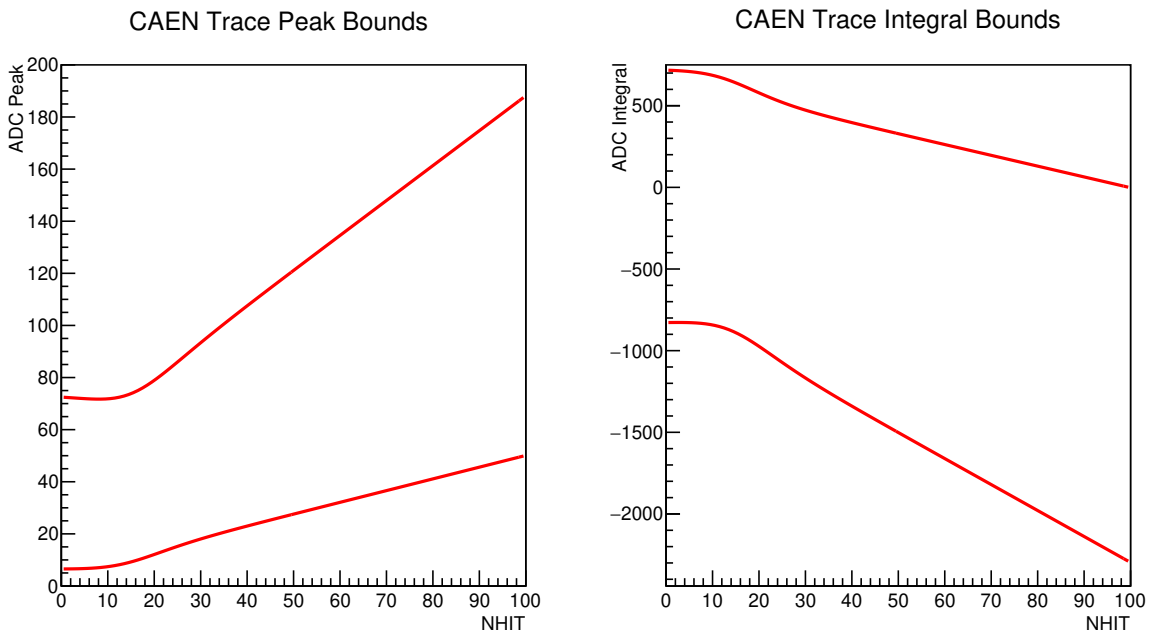

Figure 3.5: CAEN cut digitized peak (left) and integral (right) bounds as a function of NHIT.

neutrons except for a few rare candidates (^{11}Be, ^{16}N) which already have tight bounds set thanks to Super-Kamiokande [115] and other radionuclide detectors [116]. In the case of a possible cosmogenic follower analysis, an additional data cleaning bit is set tagging events up to 60 seconds after a muon, though this will not be used in physics analysis. The muon tag which this is associated is rather simple (to avoid missing muons) and flags any event with at least 5 OWL hits and 150 hits on inward facing PMTs.

3.3.15 Polling

To monitor the detector state, the base currents and CMOS rates of each channel is periodically polled for data. Since this is a forced trigger it is very easy to tag these events and remove them from data. Events during so-called detector polling are flagged by an external trigger and then removed from the data [117].

3.3.16 Retrigger

Retriggers occur when particular events are long enough that they overlap multiple trigger windows. This can occur from real light being emitted, flashers sparking over long periods of time, or pickup in the electronics. The retrigger cut removes events where 2 or more events happen within the same 3 μs window [118].

3.3.17 Burst

Flasher events often come in bursts of high light output over a period of time. Since the events in between the bursts are contaminated with extra light from the flasher events, an NHIT burst cut is applied to remove time windows which contain at least 6 events with NHIT $>$ 40 inside a 4 s window [118].

3.3.18 Missed Muon Followers

The missed muon follower cut is designed to find muons which are not tagged by the muon data cleaning word by looking for pairs of high energy events near one another in time. These events could correspond to a low energy muon which clips the detector but is not reconstructed as a muon, with a follower event arriving directly afterwards. The NHIT threshold for the pair is 60 for the primary particle and 20 for the secondary particle, where pairs must occur within a 1 ms time window. The sacrifice due to this

cut is difficult to assess because calibration data is at a rate which would easily meet this condition causing many events to be flagged. The sacrifice is instead estimated based on the random coincidence rate calculated based on the detector trigger rate.

3.3.19 Missing CAEN Data

The CAEN digitizer is important in removing instrumental backgrounds and when the data rate gets too high then its buffers will fill and be unable to record waveform data for events which overflow the buffers. This typically occurs when burst events or breakdowns occur, and so events which do not have valid CAEN data are simply removed from the data set [118].

3.3.20 Pedestal

Another method for tagging detector monitoring tools is to look for pedestal triggers in the event triggerword. In most cases the pedestal cut directly overlaps with the polling cut, but acts as a backup during runs in which the external trigger source is not active. Since there is concern that polling and detector state monitoring, which is periodically run, may change the state of the electronics during the checks, a safe approach is to remove all events within a time window around the checks. The pedestal cut removes the block of pedestal events during a polling check as well as 1 second before and after the checks and is accounted for when calculating the detector live time [117].

3.4 Signal Sacrifice

An inevitable consequence of applying data cleaning cuts is that a portion of the physics events will also be subject to the conditions of a portion of these cuts. The goal is to minimize the signal loss, known here as sacrifice, while still maintaining a cut that removes nearly all of the instrumental backgrounds. Since certain components of the detector are difficult to model (such as the CAEN digitizer), a combination of detector simulations and calibration data are used to assess the total signal sacrifice as a function energy, position, and NHit. Initial studies using the detector simulation were done by Walker [119] as a means to set initial values for data cleaning cuts used for the water phase prior to data taking. The following section compares the sacrifice from ^{16}N calibration data with that expected from simulations, focusing primarily on the true NHIT, reconstructed energy, and the reconstructed position. Ideally there will be little bias as a function of observables within the analysis window, as well as minimal sacrifice. When performing the cut tuning, an arbitrary goal of 1% signal sacrifice across all cuts was used, though this was not strictly enforced. In total two separate calibration runs were taken using ^{16}N during the water phase and uncertainties in sacrifice are estimated using the difference in these two run sets. The total sacrifice over ^{16}N calibration is shown in table 3.4, separating the sacrifice into its individual components. Data cleaning cuts were plotted as a function of NHITS, energy, and r^3 in figures 3.6, 3.7, and 3.8 respectively to look for overall bias. In areas near the region of interest (where the ^{16}N statistics are highest), the distributions are flat, implying no bias.

3.4.1 Fitter Classifier Sacrifice

When attempting to reconstruct an event, the fitter assumes that the event is a Cherenkov event, and then proceeds to find the most likely energy, position, time, and direction accordingly. If an event is an instrumental then it is unlikely to behave like Cherenkov light and the fitter will perform very poorly. This feature of the fitter is very convenient as a secondary tool for removing instrumentals independent of data cleaning. The fitter will only fail if the minimization in the fitting likelihood fails, but it is possible for the fit to converge slowly and return a valid fit for non-Cherenkov events. To handle such

Data cleaning word	Fractional Sacrifice – run 1	Fractional Sacrifice – run 2
junkcut	0.00001	0.00009
qvnhit	0.00004	0.00036
retriggercut	0.00000	0.00000
flashergeocut	0.00165	0.00055
caencut	0.00200	0.00578
qvt	0.00135	0.00255
thresholdflashercut	0.00000	0.00000
tpmuonfollowercut-long	0.00000	0.00000
qcluster	0.00199	0.00080
tpburstcut	0.00000	0.00000
ftscut	0.00070	0.00141
owlcut	0.00106	0.00068
missedmuonfollower	0.00000	0.00000
itctimespreadcut	0.00003	0.00045
muontag	0.00000	0.00000
pollingcut	0.00000	0.00000
prescalecut	0.00000	0.00000
nothingcut	0.00000	0.00000
nhitcut	0.00000	0.00000
zerozerocut	0.00381	0.00395
ringoffire	0.00000	0.00001
crateisotropy	0.00000	0.00001
neckcut	0.00021	0.02224
firstevent	0.00000	0.00000
missingcaendata	0.00000	0.00000
tpmuonfollowercut-short	0.00000	0.00000
Total	0.01223	0.03786

Table 3.4: Data cleaning fractional sacrifice over the two ^{16}N calibration runs. The second run shows signs of a light leak near the top, inflating the neck cut sacrifice.

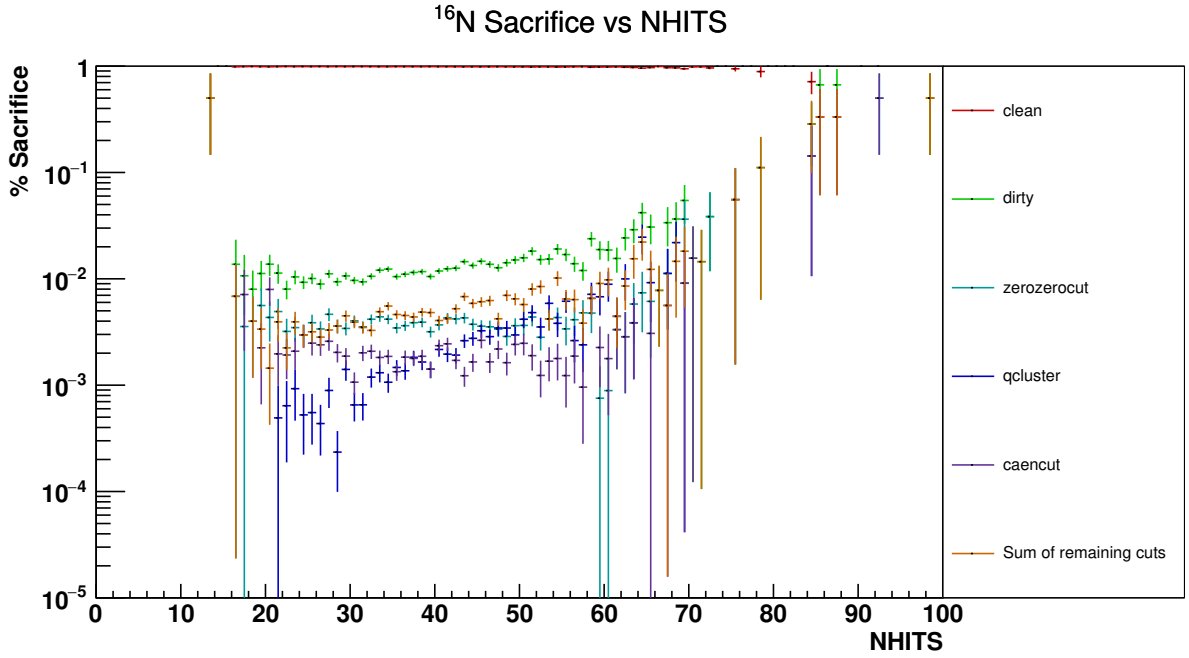

Figure 3.6: Sacrifice as a function of NHIT due to data cleaning cuts on ^{16}N calibration data. Shown in descending order are the most dominant cuts, with the remaining cuts summed together.

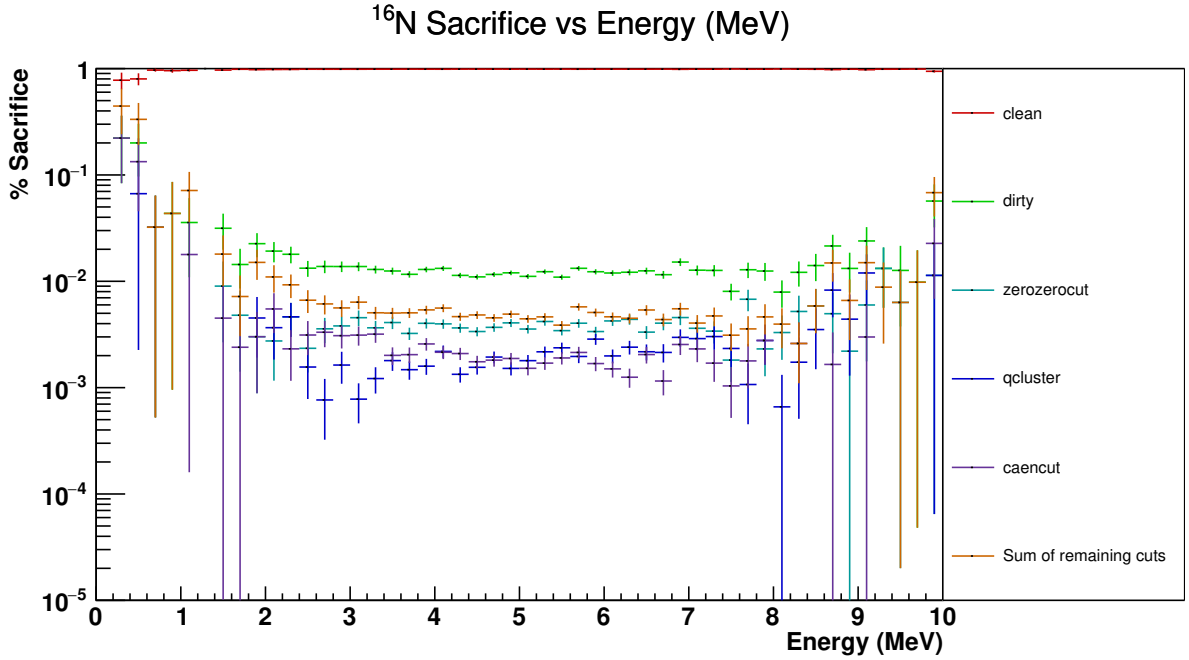

Figure 3.7: Sacrifice as a function of reconstructed energy due to data cleaning cuts on ^{16}N calibration data. Shown in descending order are the most dominant cuts, with the remaining cuts summed together.

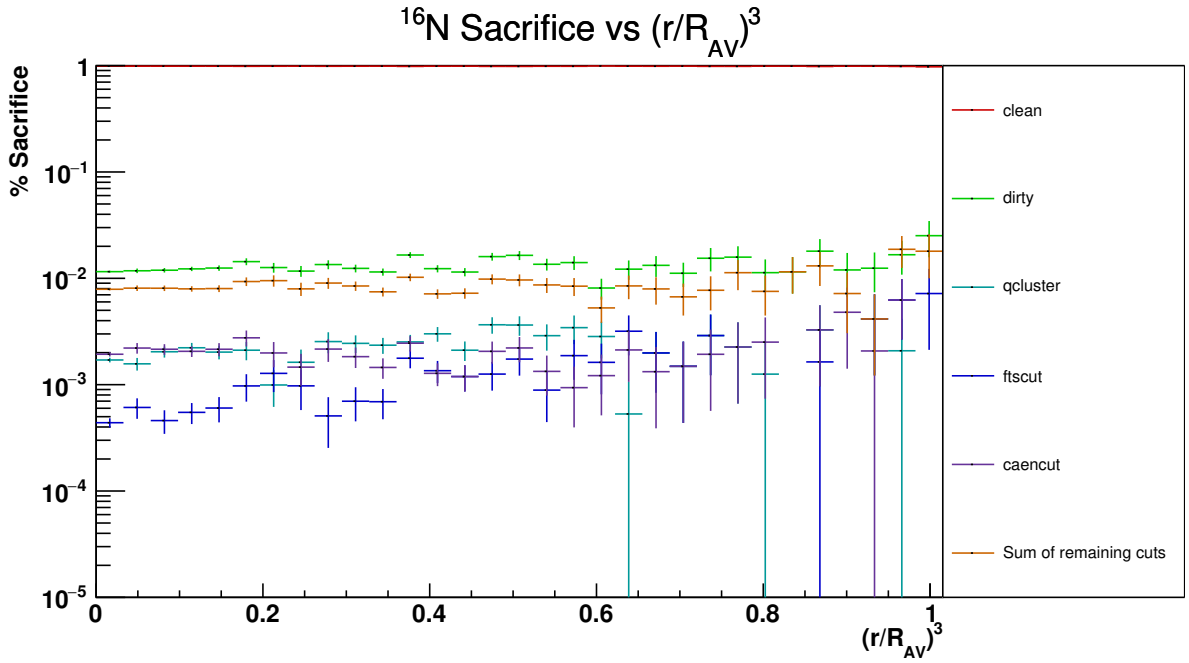

Figure 3.8: Sacrifice as a function of reconstructed radius(cubed) due to data cleaning cuts on ^{16}N calibration data. Shown in descending order are the most dominant cuts, with the remaining cuts summed together.

cases fit classifiers are in place which take the fitted vertex information and subsequently assess the Cherenkov-like properties for that particular vertex. The two classifiers used in this analysis are the β_{14} isotropy classifier and the in-time ratio (ITR) classifier described below.

3.4.1.1 β_{14} Isotropy Classifier

Cherenkov events have a well defined shape, and even at low energy should not appear isotropic. As a means to measure the total isotropy of events, SNO relied on a measure of the isotropy of an event relative the reconstructed position with respect to the hit distribution in the detector. The so-called β_l parameters [120],

$$\beta_l = \frac{2}{N(N-1)} \left[\sum_{i=1}^{N-1} \sum_{j=i+1}^{N} P_l(\cos\theta_{ij}) \right], \tag{3.23}$$

where $P_l(\cos\theta_{ij})$ are Legendre polynomials for the angle subtended by photomultiplier pair ij. Linear combinations of various β_l where previously tested comparing the separability of simulated Cherenkov events with isotropic events. Empirical studies by Dunmore [121]

concluded that β_1 has the strongest separability followed by β_4 and β_5. An optimal separability was found to be:

$$\beta_{14} = \beta_1 + 4\beta_4. \tag{3.24}$$

β_{14} is used as an event classifier in SNO+ to separate Cherenkov events from isotropic signals in the detector.

3.4.1.2 In-time Ratio Classifier

The second event classifier compares the time residual distribution of hits in an event using the reconstructed time and position to that of expected Cherenkov light. In a Cherenkov process, the light is emitted in a very short time window, and in water will have the majority of light arrive within a short prompt window. ITR is calculated as the ratio of PMT hits whose time residual falls within this window to all hits. For the water analysis the window is [-2.5ns, +5.0ns]. The time residual of a PMT hit is the difference in time between the measured arrival time and the expected time under the hypothesis that the photon is Cherenkov radiation and traveled directly from the reconstructed event vertex to the PMT. A plot of the classifiers separating flasher events (tagged via data cleaning) and ^{16}N calibration events is shown in figure 3.9. Based on this distribution and values used in the SNO experiment, physics events require $-0.12 < \beta_{14} < 0.95$ and $ITR > 0.55$. The sacrifice and contamination from these cuts are shown in the following section.

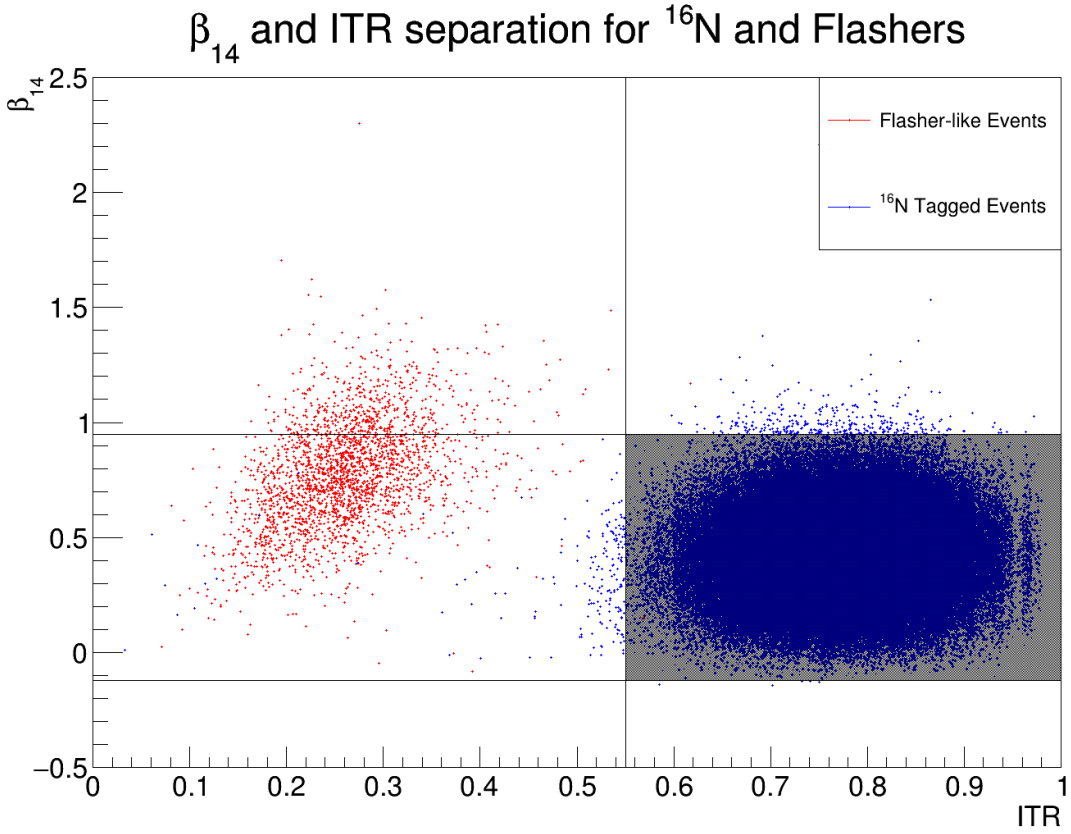

Figure 3.9: Comparison of β_{14} and ITR for tagged ^{16}N and Flasher-like events (events which are flagged by data cleaning cuts: crateisotropy, ftscut, flashergeocut). Events have reconstructed energy > 4.5 MeV and radial position < 6 meters.

3.5 Contamination

The other half of the equation is the resulting contamination of instrumentals that happen to pass the cuts and make it into the physics signal. Unlike the sacrifice measurement, contamination cannot be assessed using a known calibration source. Furthermore, instrumentals are an open set in that they are defined as everything that can occur within the detector that is not the result of a particle physics process. One way to handle this problem, as was done in SNO, is to perform a so-called bifurcated analysis, comparing the efficiency of data cleaning cuts with higher-level reconstruction cuts [113] [112]. In order to perform such an analysis a set of assumptions must be made which may only be partially true, and then try to be as conservative as possible in order to account for this. The basic approach is to take two cuts (or two branches of cuts) and then proclaim that those two cuts are uncorrelated. If this is true then the "pass" and "fail" rates of each of the branches can be compared using the following set of over-constrained equations,

$$A + C = x_1\nu + y_1\beta, \tag{3.25}$$

$$A + B = x_2\nu + y_2\beta, \tag{3.26}$$

$$A = x_1x_2\nu + y_1y_2\beta, \tag{3.27}$$

$$S = \nu + \beta, \tag{3.28}$$

where S is the total number of events in the data set, β is the number of background events (instrumentals), ν is the number of signal events, x_1 and x_2 are the signal acceptance of cuts 1 and 2 respectively, and y_1 and y_2 are the background acceptance of cuts 1 and 2 respectively. The constants A, B, C, D are shown in figure 3.10 and are measured directly from the data set. x_1 and x_2 are found through the sacrifice studies using ^{16}N. The unknown parameters are ν, β, y_1, and y_2, though in practice only the product, $y_1y_2\beta$, is required to know the total contamination. Using the assumption that the combination of the two cuts works very well, then all of the backgrounds should fall into at least one of the fail events,

$$\begin{aligned} \beta &= B + C + D, \\ \nu &= A. \end{aligned} \tag{3.29}$$

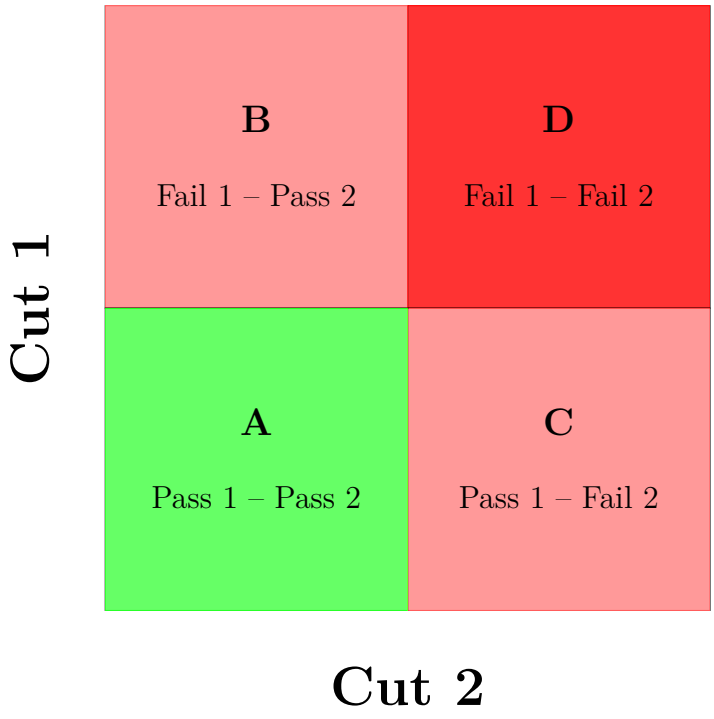

Figure 3.10: Pictorial representation of the bifurcated analysis.

This simplifies equations 3.25, 3.26, 3.27, and 3.28 to

$$y_1 y_2 = (A + C - x_1\nu)(A + B - x_2\nu)/\beta^2 \equiv \phi_1 \tag{3.30}$$

$$y_1 y_2 = (A - x_1 x_2 \nu)/\beta \equiv \phi_2. \tag{3.31}$$

The solution to $y_1 y_2$ is therefore not unique except under very specific conditions, with a best fit value which minimizes the error in $y_1 y_2$. For a linear system of equations of the form $A_{mn} x_n = b_n$ where $m > n$, there exists a vector x_n such that the solution x^* satisfies,

$$|A_{mn} x_n^* - b_n|^2 \leq |A_{mn} x_n - b_n|^2 \quad \text{for all } x_n. \tag{3.32}$$

Using the least squares method, one finds that the analytic solution can be found, though one must be careful in more complicated systems because there may be multiple solutions to the above inequality. This method involves multiplying the set of equations by the transpose of matrix A to form a standard square system of linear equations,

$$(A'_{nm} A_{mn}) x_n = A'_{nm} b_n, \tag{3.33}$$

and then simply solving for x_n. The system of equations can be rewritten in a similar fashion,

$$\begin{pmatrix} \phi_1^{-1} \\ \phi_2^{-1} \end{pmatrix} y_1 y_2 = \begin{pmatrix} 1 \\ 1 \end{pmatrix}, \tag{3.34}$$

with the above prescription yielding

$$y_1 y_2 = \frac{\phi_1 \phi_2^2 + \phi_2 \phi_1^2}{\phi_1^2 + \phi_2^2}. \tag{3.35}$$

A conservative assumption is made in which the entire data set is background such that the total contamination is

$$K = y_1 y_2 S. \tag{3.36}$$

As an alternate, a more conservative approach would be to choose the highest of the two values for $y_1 y_2$ from the set of equations.

3.5.1 Applying the Bifurcated Analysis

As was done by Pershing [122], pathological events must be removed from the data set before applying the contamination study. This includes data cleaning cuts which tag muons and their followers, as well as events created by specific non-physics triggers. The high level cuts made during analysis must also be applied for the contamination since only events which contaminate this window are of interest. The pathological cuts will remove the following:

- Muon + Muon Followers
- Junk, Ring of Fire, and zerozero events
- ITC Timespread
- Fitter does not converge
- Radius $>$ 5.5 m
- Energy $<$ 4.5 MeV and Energy $>$ 9.0 MeV
- ESUMHI, ESUMLO, pedestal, and pulseGT triggers

Cut 1	**Cut 2**
QvNhit	$-0.12 < \beta_{14} < 0.95$
Owl	$ITR > 0.55$
Neck	
QvT	
Crate Isotropy	
Flashergeocut	
FTScut	
Qclustercut	
CAEN	

Table 3.5: Orthogonal cut branches for the bifurcated analysis.

The remaining cuts are then used to form an orthogonal basis (table 3.5). Applying this to the data set used in this analysis finds an upper bound on the contamination K,

$$\begin{aligned} A &= 9, \\ B &= 1, \\ C &= 1, \\ D &= 83, \\ x_{data\ cleaning} &= 0.9933 \pm 0.0026, \\ x_{fit\ classifiers} &= 0.9993 \pm 0.0026, \\ K &= 0.037 \text{ at } 90\%\text{C.L.} \end{aligned} \tag{3.37}$$

for an energy window of 5.5 MeV to 9.0 MeV. Uncertainties on the sacrifice are determined by statistically fluctuating the number of events in the calibration and data sets, and the uncertainty on the contamination is determined by statistically fluctuating A, B, C, and D as well as the sacrifice. The distribution of possible $y_1 y_2$ values is then integrated from 0 to K such that it covers 90% in order to set an upper bound on the value. The sacrifice used for the contamination study differs from the real sacrifice found previously because it focuses only on the region of interest, and ignores signal sacrifice to pathological events.

Chapter 4

Water Phase Systematics

The Monte Carlo detector simulations for SNO+ are very detailed and account for many of the detector systematics already. These simulations are not perfect though, and this shows up as uncertainties in the detector resolution from reconstruction and uncertainties on the background rates. The primary means to assess these uncertainties is through an energy calibration source, which for the water phase analysis is primarily ^{16}N. To determine the effects of reconstruction uncertainty and bias, the simulated data set will be smeared using analytic functions for each of the various reconstructed parameters (energy, position, and direction), and the analysis will then be run with these updated distributions.

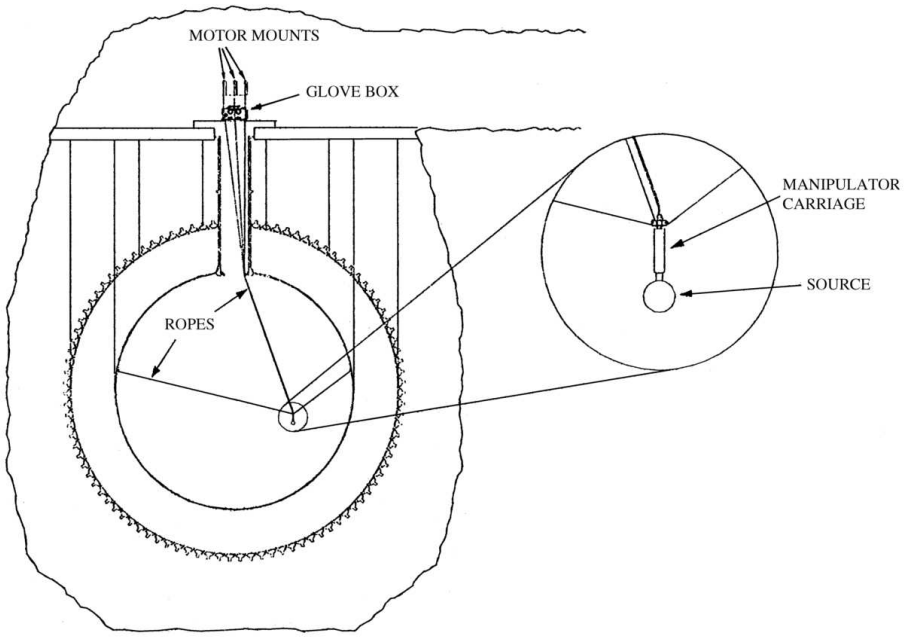

Figure 4.1: Calibration manipulator ropes and carriage from [19].

4.1 Calibration

Detector calibration in SNO+ comes in two forms: optical and energy. The optical calibration system consists of four subsystems each designed to tune different components of the detector. These consist of an updated version (for cleanliness) of the SNO laserball, as well the External LED/Laser Light Injection Entity (ELLIE), which is used to calibrate the PMT timing and gain, scintillator properties and PMT response as a function of event position. Energy calibration is done using an ^{16}N source and an Am-Be [1] source. For the water phase the primary calibration source is the ^{16}N, whereas the Am-Be source (which is a good neutron capture calibration source) is only used for low energy calibration and calculation of neutron capture efficiencies for reactor $\bar{\nu}_e$ measurements.

4.1.1 Optical

The goal of optical calibrations is to account for electronic variations when determining event position, direction and energy. To do this, each PMT must have a well understood time offset, discriminator time walk , and gain. PMT time offset comes from the relative

[1] ^{241}Am is an α emitter which bombards the ^{9}Be nucleus producing an (α, n) reaction which emits a neutron in coincidence with a 4.44 MeV γ roughly 75% of the time [123].

cable length and electronic path that the PMT signal must take before being readout by the Crate Trigger Card. A time delay is introduced per channel such that every PMT signal has the same relative transit time between the initial charge collection in the PMT and the trigger at the CTC. Discriminator time walk is an effect seen in constant threshold discriminators where high charge PMT hits cross the discriminator threshold sooner than low charge PMT hits, causing an apparent shift in the initial time. Time walk corrections apply a shift to the PMT hit time based on the charge deposited to mitigate the effect. This is achieved by having multiple optical calibration sources which can target specific components individually, these are described as follows.

4.1.1.1 Laserball

The laserball consists of a light diffusing sphere consisting of a fully synthetic fused quartz flask—designed specifically for the SNO+ low radioactivity requirement— which is filled with hollow glass spheres suspended in silicone gel [124]. Light is injected into the laserball via a fiber-optic bundle using a nitrogen dye laser which provides pulsed radiation at 337.1 nm with a 600 ps pulse width. This provides an approximately uniform distribution of light within the detector, which with information on the position of the laserball, allows the tuning of individual channel delays and gain measurements [19]. Furthermore, by moving the laserball to off-axis positions, absorption coefficients can be measured.

4.1.1.2 Tellie

Ellie is split into three subsystems, the primary subsystem is the timing module (Tellie). Tellie uses a system of optical fibers located on the outside of the PMT support structure running from the deck. These fibers are located along many points of the detector, pointing inwards to opposite sides. This provides the unique benefit of being able to run calibrations in-situ as opposed to requiring the deployment of a light source into the detector. Tellie uses 92 PMMA (acrylic) fibers with large opening angles along various locations, which have enough overlap to bootstrap the timing calibration by comparing multiple fibers on single PMTs. Tellie is used as a means to correct for PMT time offsets and time walk effects, which are stored in database tables and corrected for during event reconstruction [125] [124].

4.1.1.3 Smellie

The Scattering Module subsystem of Ellie (Smellie) is smaller than Tellie with only 4 injection points, each with 3 separate beam angles. Smellie uses a laser with a narrow angle of emission designed to assess the scattering properties of the detector medium. This becomes very important when switching from water to liquid scintillator, as the scattering length in scintillator is much shorter (in water for a detector the size of SNO+, the scattering length has a negligible effect) [126].

4.1.1.4 Amellie

The Attenuation Module subsystem of Ellie (Amellie) is similar to Smellie with 4 injection points; however, it only has 2 beam angles, but is intended to operate at various frequencies. Amellie is designed to monitor the optical attenuation of the liquid scintillator as a function of time (as it is common for optical properties to degrade over time) [127] [119].

4.1.2 ^{16}N Source

Energy calibration for the water phase of SNO+ is based on the energy deposited by the γ-rays produced from ^{16}N β-decay. This source was tested and used to great effect in SNO, so much of the properties of the design and implementation are already well understood. ^{16}N is a short-lived isotope ($t_{1/2} = 7.13$ s), so the isotope must be produced on-site through a commercial Deuterium-Tritium (DT) generator. The DT generator accelerates both deuterium and tritium into a target which also contains deuterium and tritium, resulting in 14-MeV neutrons,

$$d + t \rightarrow n + {}^4\mathrm{He}. \tag{4.1}$$

The neutrons are then captured on the oxygen atoms in a CO_2 environment, which flows from the DT generator into the decay chamber residing within the detector.

$$^{16}\mathrm{O} + n \rightarrow {}^{16}\mathrm{N} + p \xrightarrow{7.13\ \mathrm{s}} {}^{16}\mathrm{O} + e^- \tag{4.2}$$

The resulting oxygen nucleus deexcites emitting a cascade of γ's whose relative intensity is given in table 4.1. The γ's with intensity lower than 0.1% are omitted from the table. The decay chamber can be moved throughout the detector through a series of side ropes as shown in figure 4.1 allowing for positional dependence to be accounted for. The activated

Energy (MeV)	Intensity (%)
1.76	0.121
2.74	0.82
2.82	0.13
6.13	67.0
7.12	4.9

Table 4.1: Deexcitation γ's from the β decay of ^{16}N with intensity $> 0.1\%$.

CO_2 is sent through an umbilical to the decay chamber shown in figure 4.2. To provide a tag for the emitted γ, a small PMT paired with plastic scintillator is housed within the decay chamber and provides a coincidence signal by measuring the emitted β from the ^{16}N decay. Relying on the trigger signal from that PMT greatly reduces backgrounds into the calibration signal [19].

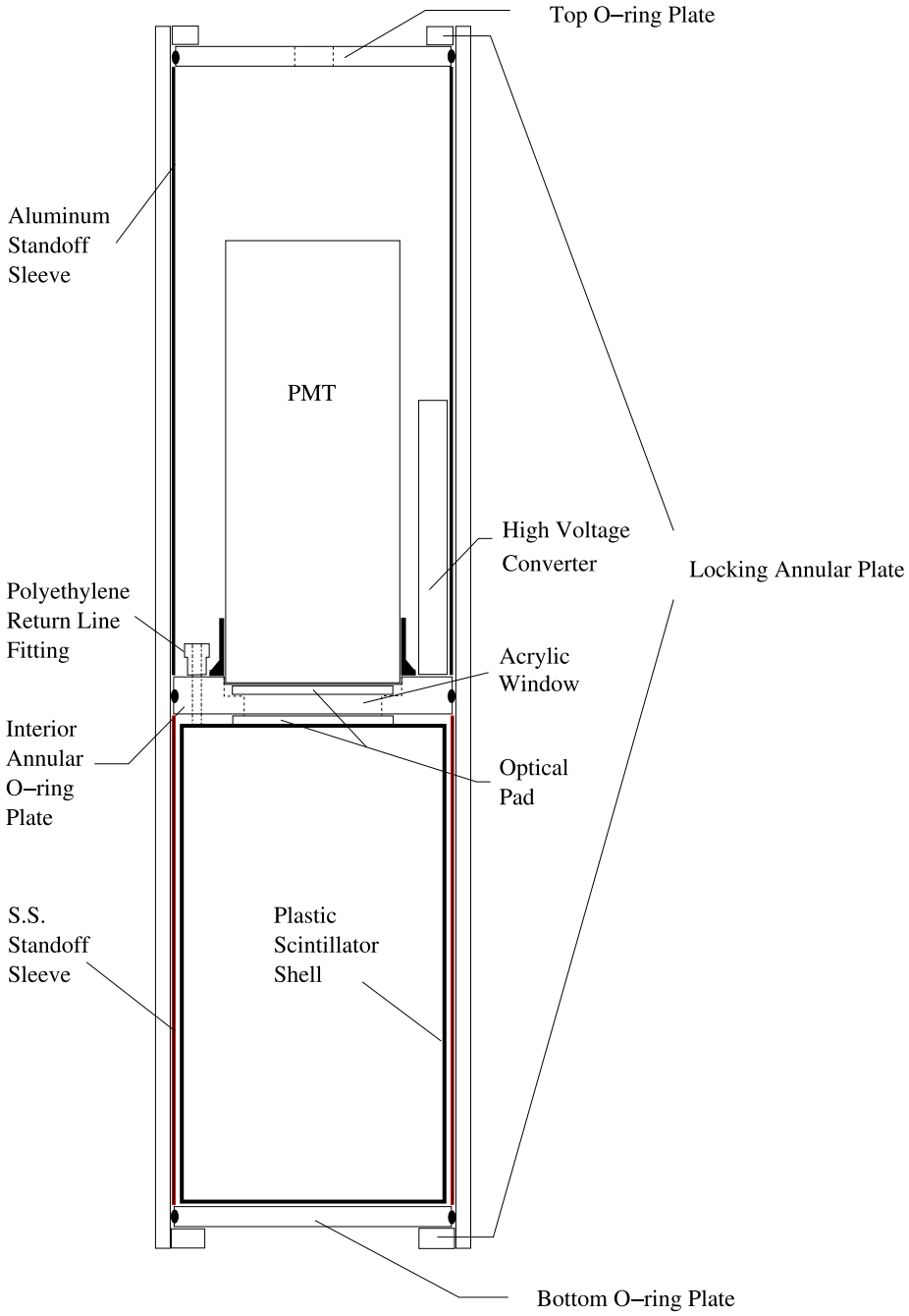

Figure 4.2: ^{16}N source decay chamber from [20].

4.2 ^{16}N Reconstruction Evaluation

As a means to estimate the systematic uncertainties of event reconstruction on the final nucleon decay result, a rather simple approach of applying the uncertainties found from calibration directly to the simulations through a smearing function was taken. This works by convolving the fitted results with an additional factor to worsen those results based on the difference between simulated and actual ^{16}N data. In an ideal case each uncertainty would be applied individually and then the full fitting algorithms would be rerun to see the effects of the correlation between the uncertainties. Due to limitations in computational resources, it is not feasible to rerun the reconstruction algorithms in this manner. By smearing each parameter individually post-reconstruction, correlations between energy, direction, and vertex fits are ignored. Since the effects of such correlations are expected to be small, smearing each parameter individually will provide a satisfactory estimate of the systematic uncertainties. The three main contributors to reconstruction uncertainty are energy, position, and direction. Both simulated and actual ^{16}N data will be fit with an analytic response function convolved with the necessary ^{16}N source information to translate γ response into electron equivalent values.

4.2.1 Calibration runs

Two sets of calibration runs taken during the water phase were used for systematic uncertainty evaluation and tuning of the detector simulation. The first (shorter) set only sampled along the z-axis of the detector prior to the side-ropes being ready and consisted of 7 source positions. The second (longer) set included the side-ropes to provide off-axis measurements. The central position will be used in the analysis to set estimates of the systematic uncertainties in reconstruction resolution, with evaluation of off-axis measurements used as a means to validate those estimates. A more thorough examination is being made by the SNO+ calibration group which will be used in place of these estimates for the final evaluation of the full water phase final analysis. Demonstration of source tagging is shown in figure 4.3. The central concentration of vertices is the ^{16}N source decay chamber. In the top plot, which includes both tagged and untagged events, the umbilical

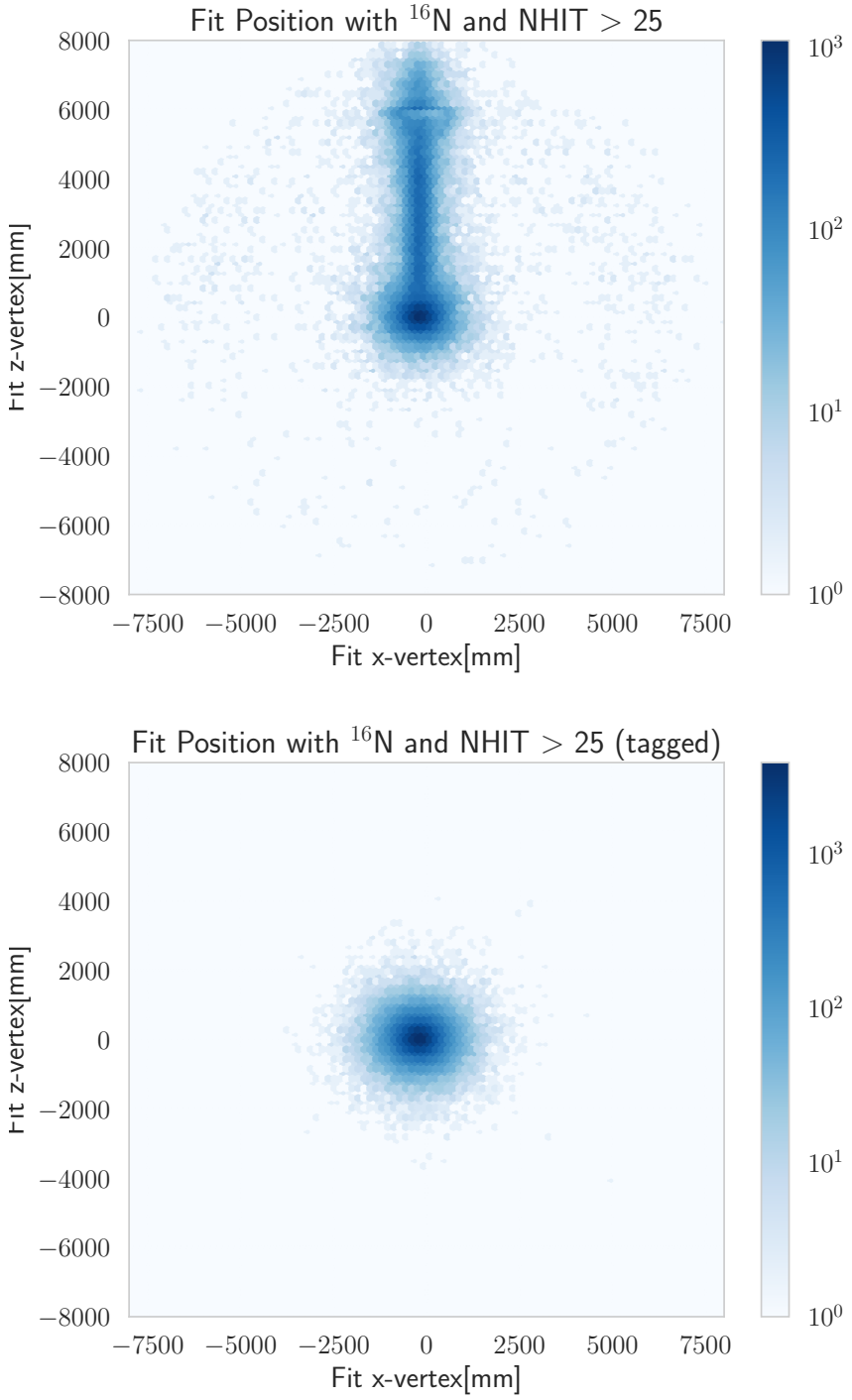

Figure 4.3: Plots of the reconstructed ^{16}N vertex for a central run (100934) showing all events with NHIT > 25 with (bottom) and without (top) the tagged β. The tagged distribution is well-centered on the deployed source position, whereas the untagged distribution has events within the umbilical which carries the activated gas, plus accidental events distributed randomly within the detector.

is clearly visible coming down to the decay chamber, as well as reconstruction of events along the acrylic vessel and in the neck of the detector.

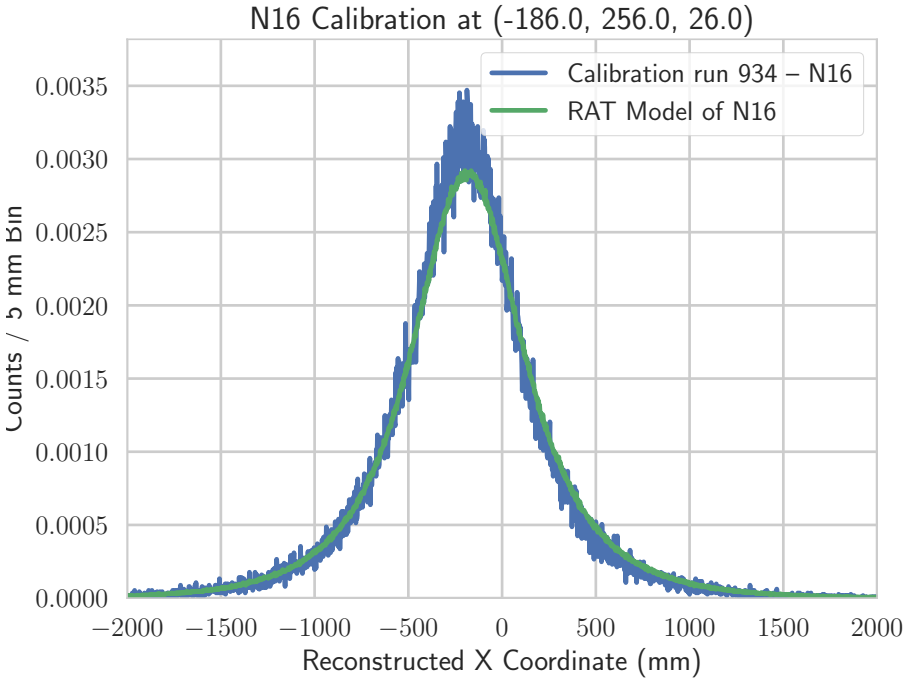

Figure 4.4: Reconstructed position (x-axis) of ^{16}N calibration data showing good agreement between the simulated and actual data.

4.3 Position Reconstruction

In order to evaluate the uncertainty on the reconstructed position the reconstructed position is compared with the known vertex of an event. Shown in figure 4.4 is the reconstructed position of events from the ^{16}N source showing good agreement between simulated and actual data. Since the ^{16}N calibration source is not point-like, the source position is further smeared in reconstruction. This smearing due to the source does not contribute to event vertex resolution for physics events, this extra broadening is accounted for by making the assumption that the first Compton scatter that the emitted photon makes is the dominant contribution to the emitted light and this Compton scatter position becomes the true event vertex. Figure 4.5 shows the results from smearing of the source position using the detector simulation. The underlying distribution to be fit is a Gaussian in one-dimension with exponential tails:

$$f(x,\alpha,\sigma,\mu,\tau) = \frac{1-\alpha}{\sqrt{4\pi\sigma^2}}\exp\left[-\frac{1}{2}\left(\frac{x-\mu}{2\sigma}\right)^2\right] + \frac{\alpha}{2\tau}\exp\left[-\frac{|x-\mu|}{\tau}\right], \tag{4.3}$$

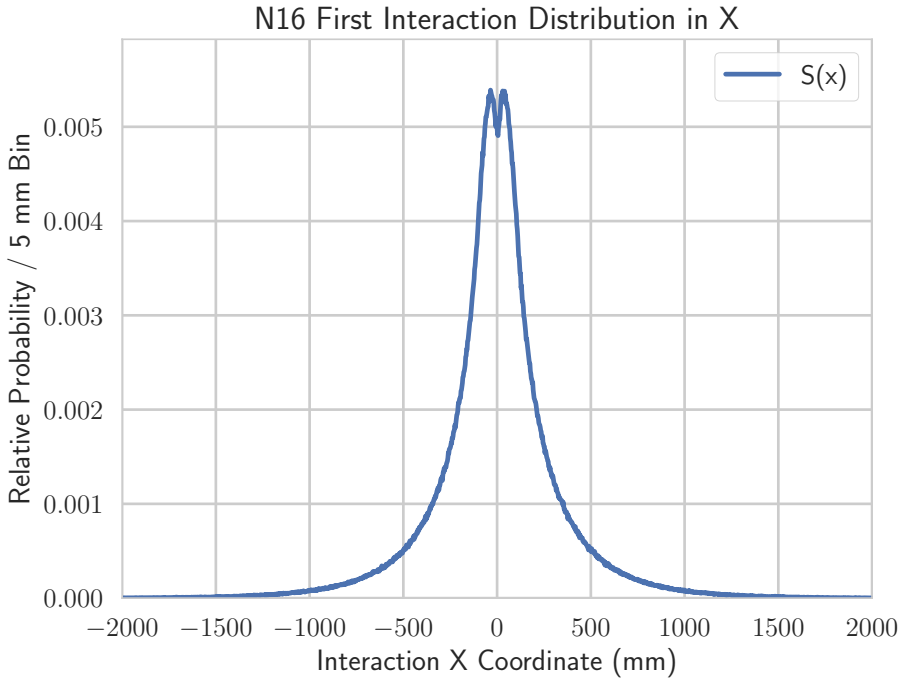

Figure 4.5: One dimensional first Compton scatter distribution for ^{16}N calibration runs in SNO+ relative to the source position. This is $S(x)$ used in the fit. The depression at the center comes from the requirement that the γ leave the decay chamber.

where μ is the true position—which can be used to evaluate any vertex bias—σ is the reconstruction vertex resolution, τ is a measure of the slope of the exponential tails, and α give the ratio of the exponential tails to the total distribution. The distribution of first Compton scatters (defined here as $S(x)$) is convolved with 4.3,

$$G(x) \equiv (f * S)(x) = \int_{-\infty}^{\infty} f(\chi, \mu, \sigma, \alpha, \tau) S(x - \chi)\, \mathrm{d}\chi\,, \tag{4.4}$$

which is evaluated numerically. This process is done for both Monte Carlo detector simulations as well as the ^{16}N measurements as a test of the simulation. This provides a comparison of the energy resolution difference between simulations and data, which will be used as an estimate of the systematic error on the results due to vertex resolution uncertainty. Figure 4.6 shows the results of this fit on the simulated data and data. Summarized in table 4.2 are the results of these fits with their parameter differences.

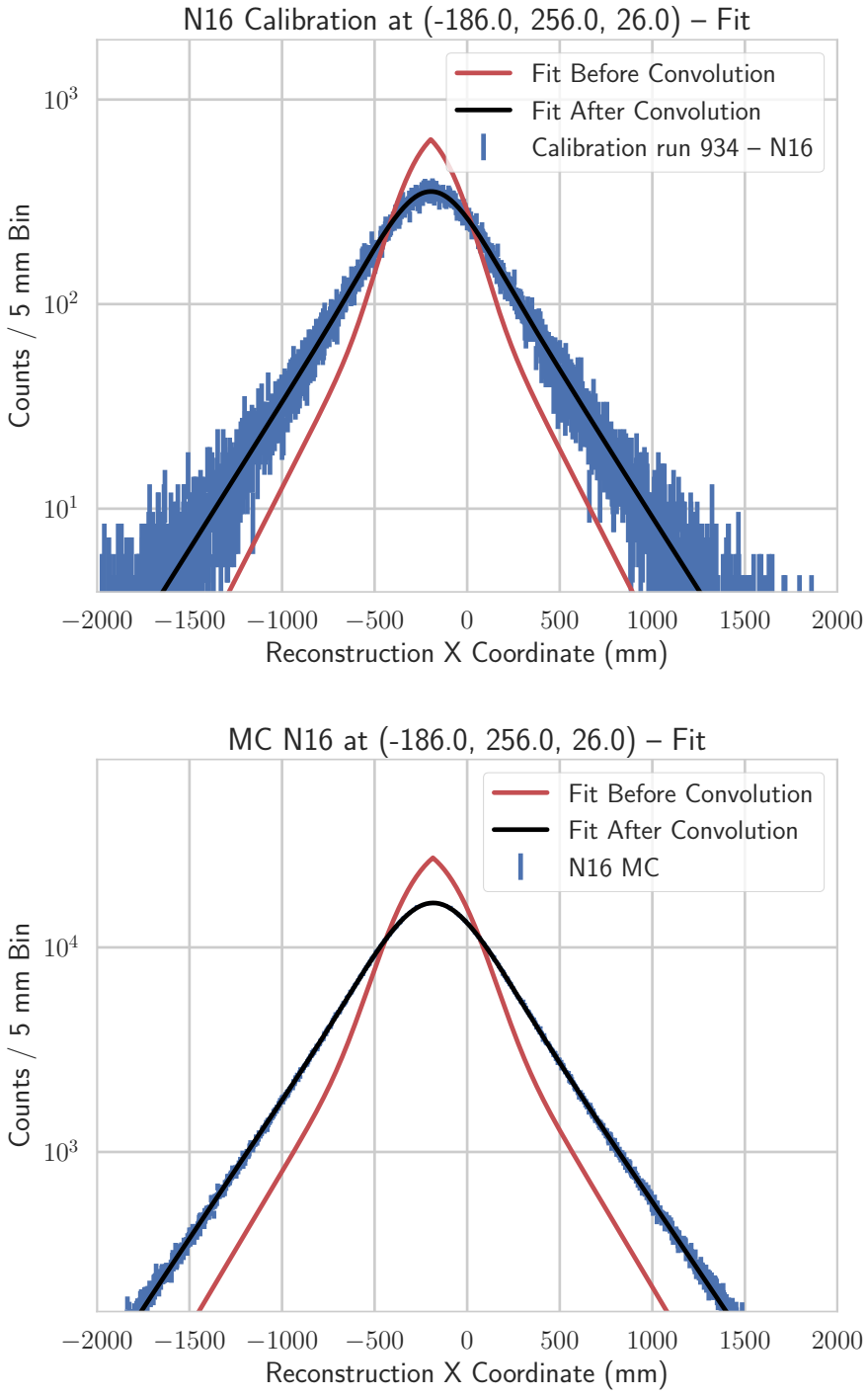

Figure 4.6: Plots of the reconstructed vertex for data (top) and simulated data (bottom) for central run (100934). The black curve is the full fit (equation 4.4) which is the convolution of the response function (shown in red—equation 4.3) with $S(x)$ (figure 4.5).

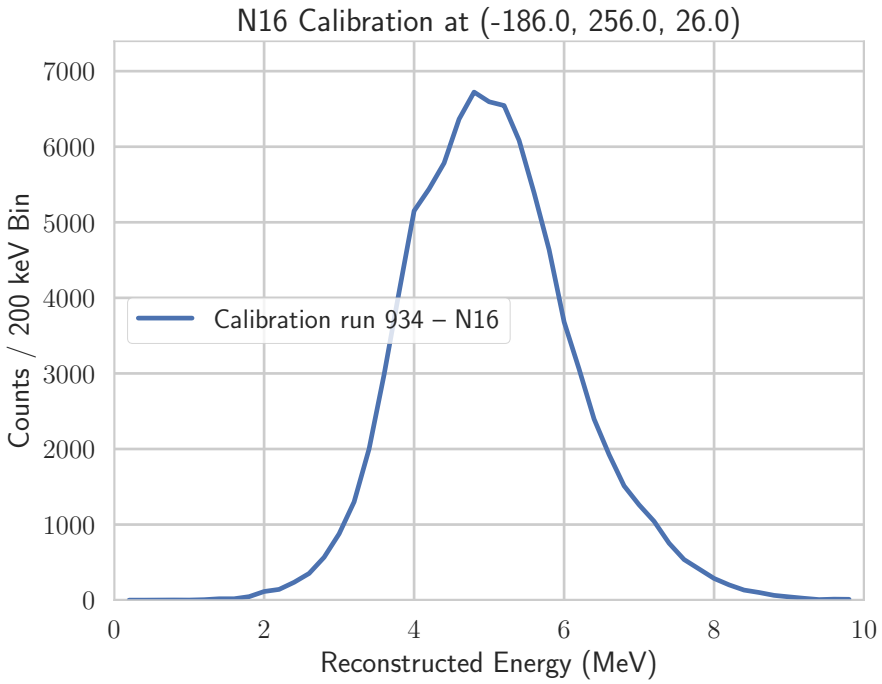

Figure 4.7: Reconstructed energy of ^{16}N calibration data. The model is shown to over predict the 2.7 and 2.8 MeV γ contribution and results in a broader energy distribution.

4.4 Energy Reconstruction

Due to the low photon count in Cherenkov radiation, reconstructing the deposited energy of an event typically results in a broad distribution which is driven by statistical fluctuations. Despite the broad width of reconstructed energy, it is still the primary observable and any discrepancies between simulated and actual data must be accounted for when assessing event selection uncertainties. Similar to vertex reconstruction, ^{16}N calibration data is used to assess the difference between data and simulations. One caveat to using this as an energy calibration, is that the source itself produces γ's whose energy deposition is based on their energy transfer to electrons via Compton scattering. Our energy reconstruction is based upon electron equivalent energy, which means in order to understand the calibration the source energy must be mapped to electron-equivalent energy. Similar to the position fit, a convolution of this mapping with a response function is used

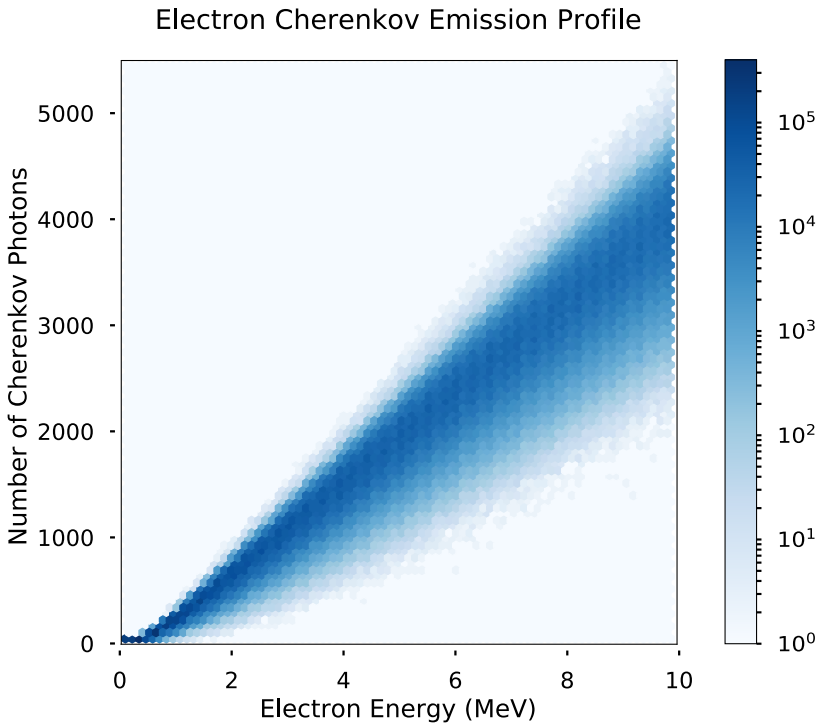

Figure 4.8: Mapping of electron deposited energy to number of emitted Cherenkov photons in water found using Monte Carlo simulations. This distribution is independent of detector geometry.

to fit the calibration source data.

$$f(E, a, b) = \frac{1}{\sqrt{2\pi b^2 E}} \exp\left[-\frac{(E-a)^2}{2b^2 E}\right] \tag{4.5}$$

This was studied in SNO [128] using the same calibration source, thus providing a good benchmark to compare with. Using Monte Carlo simulation estimations, figure 4.9 shows the distribution of deposited energy by the first Compton scatter, which accounts for loss of energy before leaving the source decay chamber. Using the deposited energy from the first Compton scatter, the total number of emitted Cherenkov photons is calculated to produce figure 4.10 which gives the distribution of the number of emitted Cherenkov photons across the ^{16}N γ emission spectrum. This photon response to ^{16}N events is translated into an electron response through sampling from a simulation of mono-energetic electrons across a 10 MeV energy range in steps of 0.05 MeV shown in figure 4.8. Finally, by

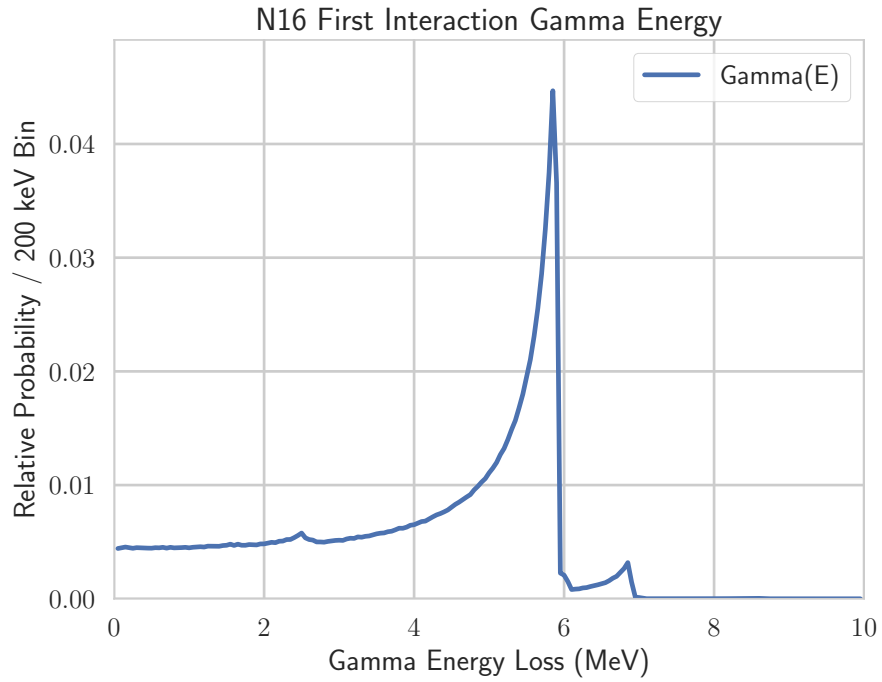

Figure 4.9: Distribution of energy deposited by the first γ interaction from the ^{16}N source outside of the source container as predicted by Monte Carlo detector simulations.

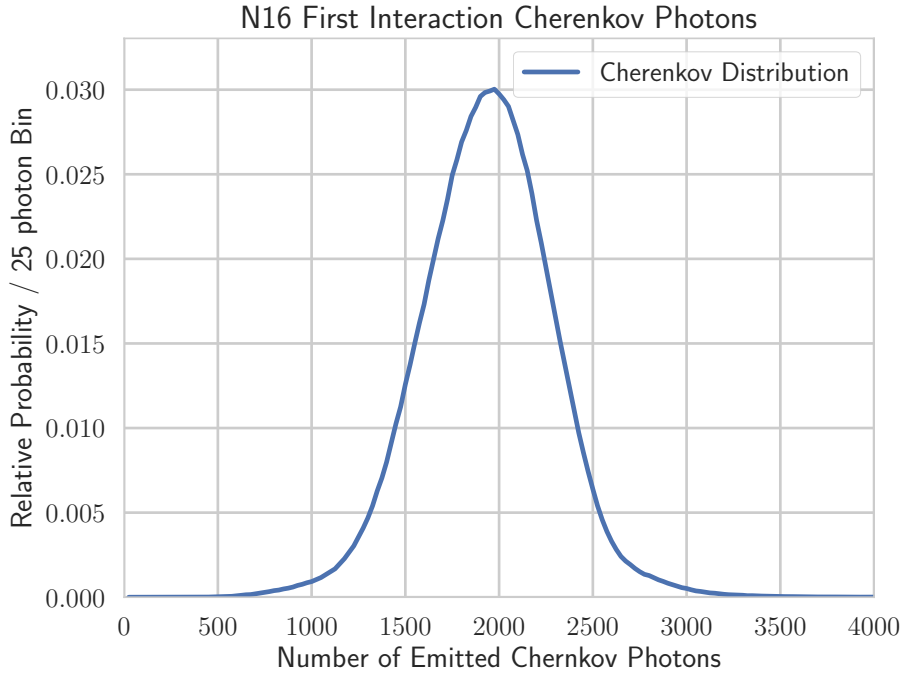

Figure 4.10: Simulated Cherenkov emission from Compton scatter of γs due to the ^{16}N source.

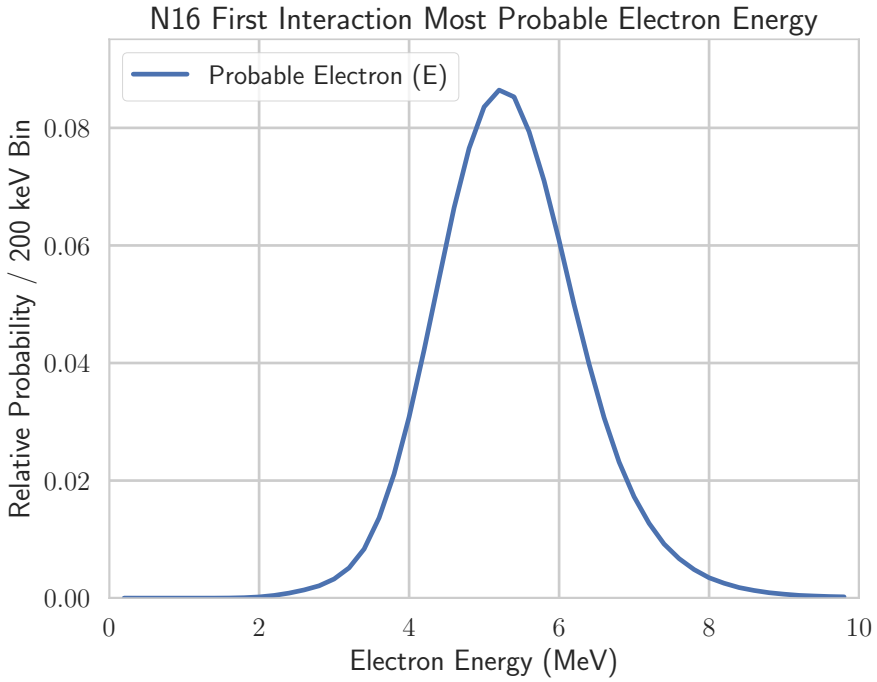

Figure 4.11: Most probable electron energy distribution obtained by randomly sampling figure 4.8 for each γ in figure 4.10.

inverting this electron-photon distribution, the most probable electron energy for a given Cherenkov photon count is found (figure 4.11). The distribution of figure 4.11, defined here as $S(E)$, is convolved with the detector response function (equation **??**) to yield:

$$G(E) \equiv (f * S)(E) = \int_{-\infty}^{\infty} f(\epsilon, a, b) S(E - \epsilon)\, \mathrm{d}\epsilon\,. \tag{4.6}$$

Figure 4.12 shows the fit to this function with both simulated and real data with results of the fits shown in table 4.3.

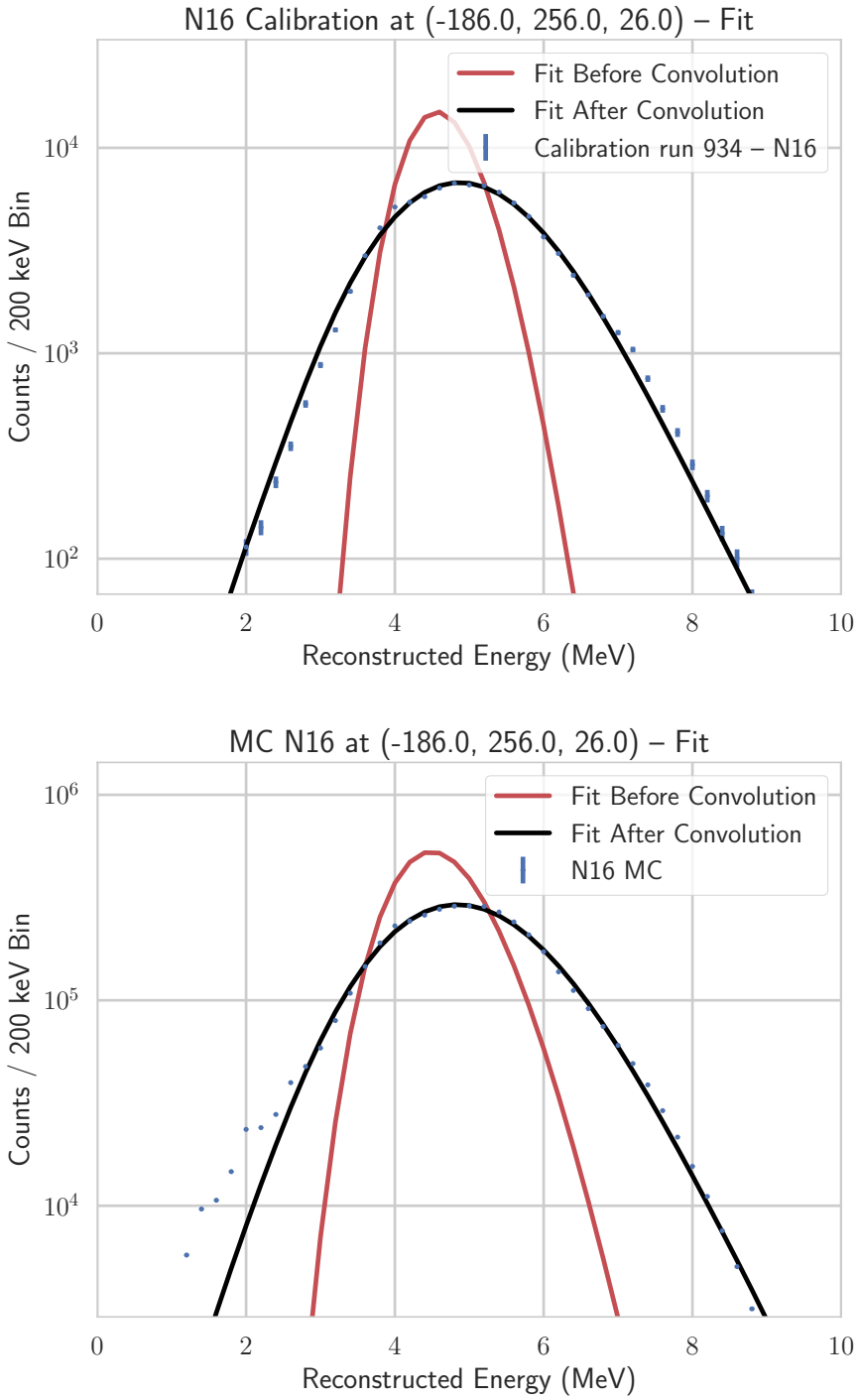

Figure 4.12: Plots of the reconstructed energy for data (top) and simulated data (bottom) for central run (100934). The black curve is the full fit (equation 4.6) which is the convolution of the response function (shown in red—equation 4.5) with $S(E)$ (figure 4.11).

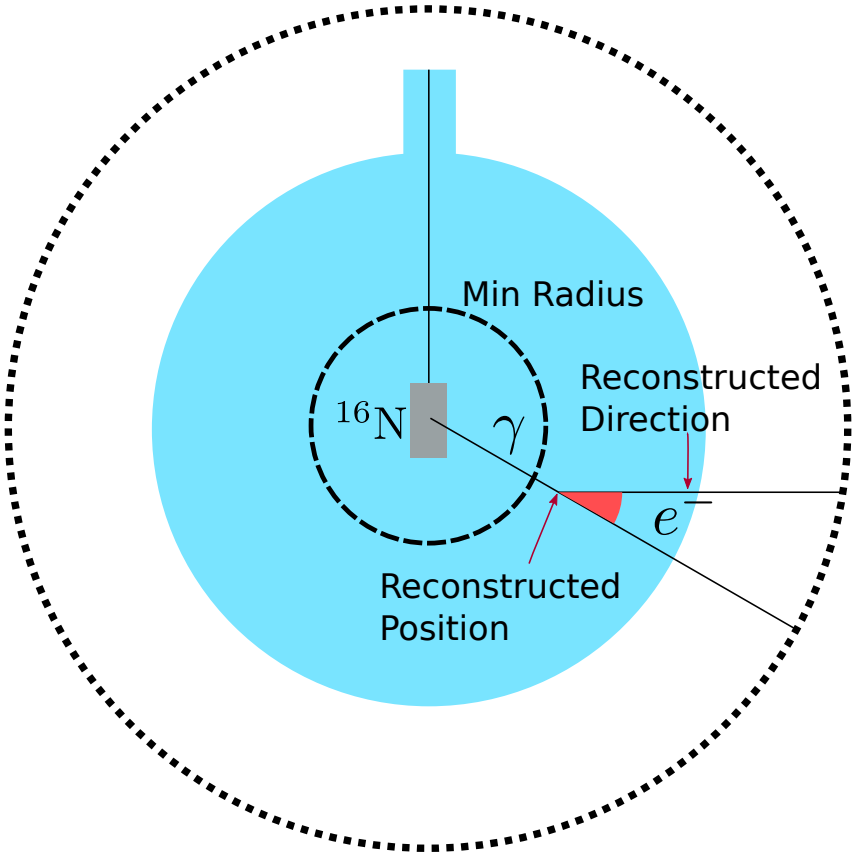

Figure 4.13: Event selection schematic for determining the SNO+ angular response. For an event which reconstructs beyond the innermost dashed ring, the reconstructed position is used to estimate the event direction assuming forward scattering.

4.5 Angular Response

The angular response of the reconstruction algorithm is primarily important in the nucleon decay analysis as a means to cut out the solar neutrino backgrounds and could potentially be used to discriminate external backgrounds (which are primarily inward pointing). Using the technique described below, the direction of events from the ^{16}N source is reconstructed in order to compare to simulated data. The true event direction for ^{16}N is not known a priori but it is possible to use the vector from the source decay chamber to the reconstructed event vertex as a proxy for the event direction. This estimate is used because the Compton scatter from the ^{16}N γ will be statistically forward scattering, causing the electron direction to point away from the source decay chamber position along the vertex vector. In order to guess the true position of the γ interaction

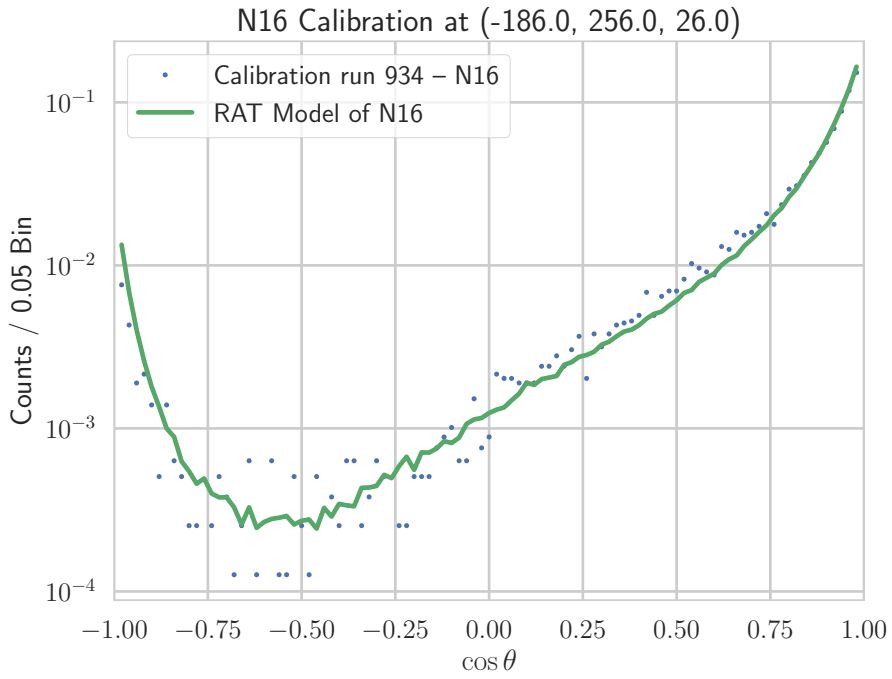

Figure 4.14: Plots of the reconstructed direction resolution for data and simulated data for central run (100934).

on event-by-event, the reconstructed position is used as a proxy for the known direction by selecting for events which appear to be forward scattering. Figure 4.13 demonstrates the event selection used for determining the true direction. To eliminate shadowing effects by the source container only events which reconstruct 120 cm from the source central position are used. 120 cm corresponds to the maximum dimension of the source container including the manipulator assembly but not the full length of the umbilical. Due to the angular response of Compton scattering, the result is a reasonable estimation of the event direction but has a noticeable distortion and back-scattering component. This remaining distribution is fit with a pair of exponential distributions described by

$$f(\theta,\alpha,\beta,\xi) = \alpha\frac{\beta\exp[\beta(\cos\theta-1)]}{1-\exp[-2\beta]} + (1-\alpha)\frac{\xi\exp[\xi(\cos\theta-1)]}{1-\exp[-2\xi]}, \tag{4.7}$$

where α denotes the ratio between the two contributions, ξ is the dominant (fast falling) component and β is the tail of the distribution. The results for both simulated and actual data are given in table 4.4 and plotted in figure 4.15 , where the detector simulations appears to overestimate the values of ξ and β. The difference in these values will be used

Position

$$f(x,\alpha,\sigma,\mu,\tau) = \frac{1-\alpha}{\sqrt{4\pi\sigma^2}}\exp\left[-\frac{1}{2}\left(\frac{x-\mu}{2\sigma}\right)^2\right] + \frac{\alpha}{2\tau}\exp\left[-\frac{|x-\mu|}{\tau}\right]$$

	α	σ (mm)	μ (mm)	τ (mm)
MC	0.44 ± 0.00	141.2 ± 0.20	-185.0 ± 0.1	298.5 ± 1.3
Data	0.46 ± 0.03	121.7 ± 1.28	-196.7 ± 0.5	257.4 ± 7.9

Table 4.2: Position reconstruction fit parameters to ^{16}N central run 100934 data and simulated data.

Energy

$$f(E,a,b) = \frac{1}{\sqrt{2\pi b^2 E}}\exp\left[-\frac{(E-a)^2}{2b^2E}\right]$$

	a (MeV)	b ($\sqrt{\text{MeV}}$)
MC	4.555 ± 0.011	0.138 ± 0.004
Data	4.597 ± 0.012	0.108 ± 0.006

Table 4.3: Energy reconstruction fit parameters to ^{16}N central run 100934 data and simulated data.

Direction

$$f(\theta,\alpha,\beta,\xi) = \alpha\frac{\beta\exp[\beta(\cos\theta-1)]}{1-\exp[-2\beta]} + (1-\alpha)\frac{\xi\exp[\xi(\cos\theta-1)]}{1-\exp[-2\xi]}$$

	α	β	ξ
MC	0.58 ± 0.01	2.24 ± 0.07	20.04 ± 0.07
Data	0.63 ± 0.02	1.96 ± 0.13	19.36 ± 1.01

Table 4.4: Direction reconstruction fit parameters to ^{16}N central run 100934 data and simulated data.

in the analysis section when estimating the uncertainty on the solar contamination into the nucleon decay signal window.

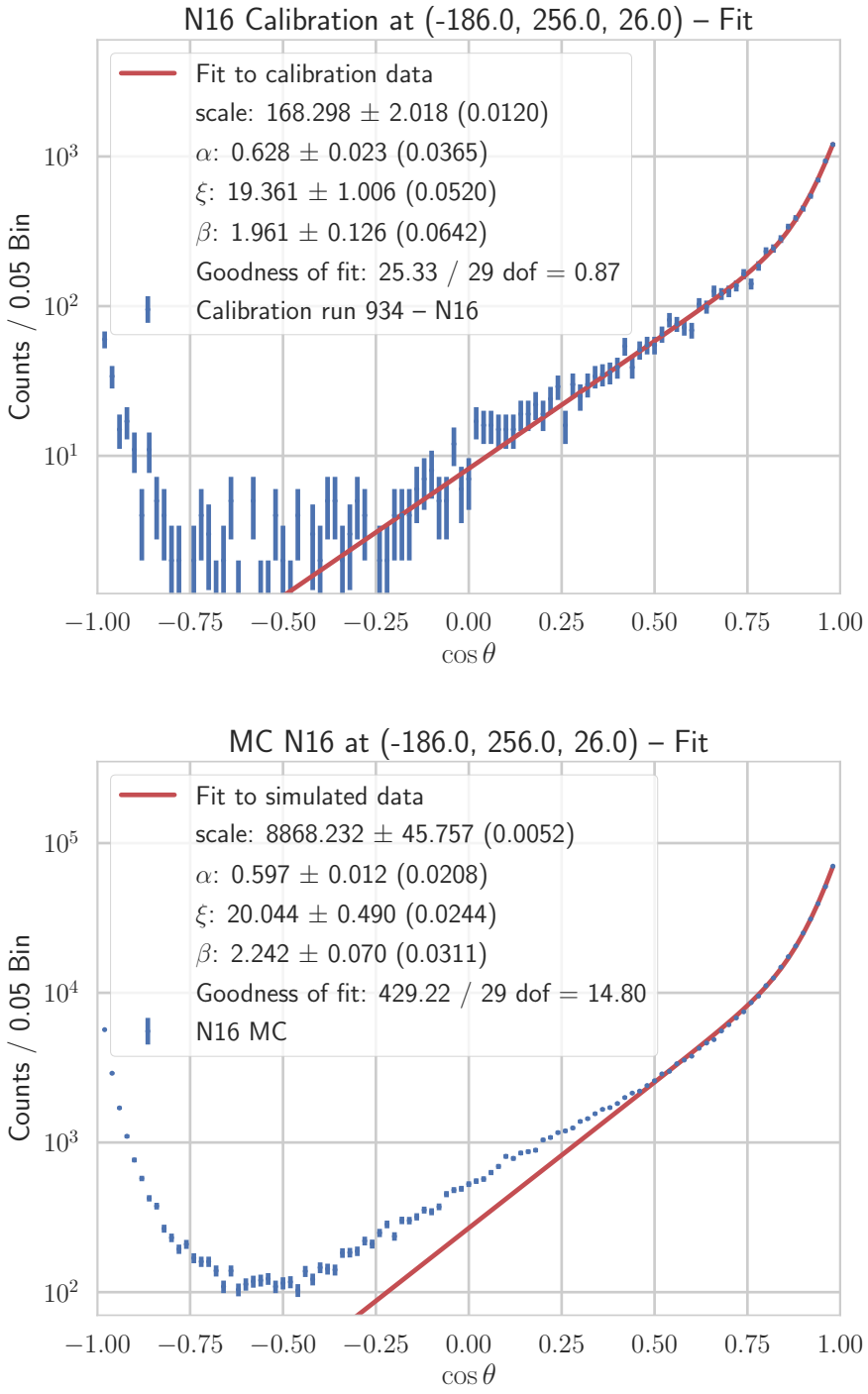

Figure 4.15: Plots of the reconstructed direction for data (top) and simulated data (bottom) for central run (100934). The double exponential from equation 4.7 is fit to both from $0.3 < \cos\theta < 1$.

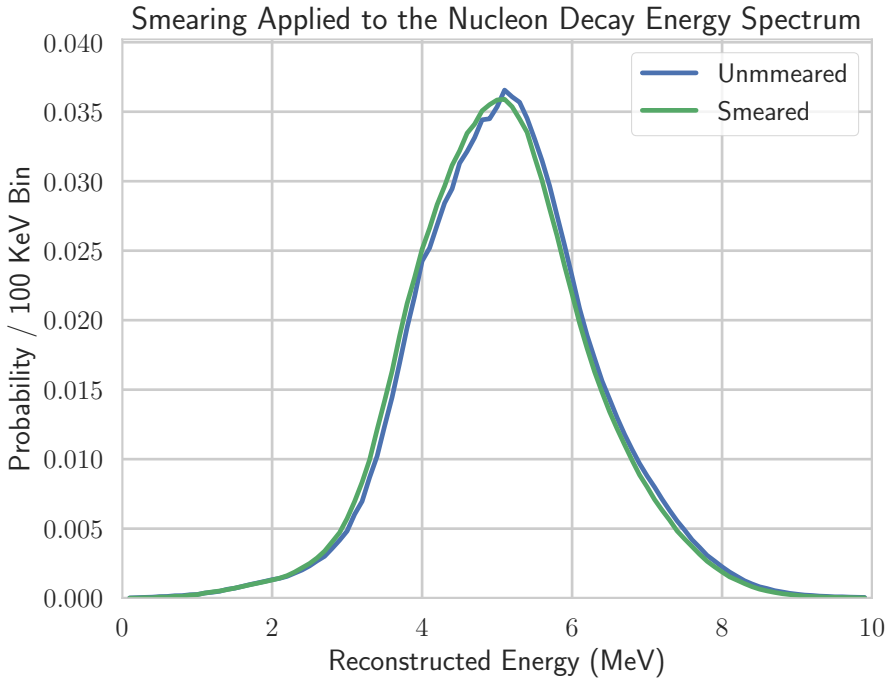

Figure 4.16: Application of energy smearing showing the overall effect of applying a Gaussian response with a bias using the systematics found in table 4.3 to the simulated invisible nucleon decay energy spectrum.

4.6 Applying the Systematic Uncertainties

The difference between simulated and actual data is used to evaluate systematic uncertainties. The approach used here for measuring the effects of differences in the fits of the previous section is to modify the simulation results with a smearing function based on these differences. The results of using this technique for energy, position, and direction uncertainties are given below.

4.6.1 Energy Smearing

Energy smearing is applied event by event to the simulated events using the fit parameters from table 4.3. In each simulated event, the previous reconstructed energy is replaced with a random draw from a Gaussian distribution based on the fit,

$$E' = \frac{1}{\sqrt{2\pi b^2 E}} \exp\left[-\frac{(E-a)^2}{2b^2 E}\right], \tag{4.8}$$

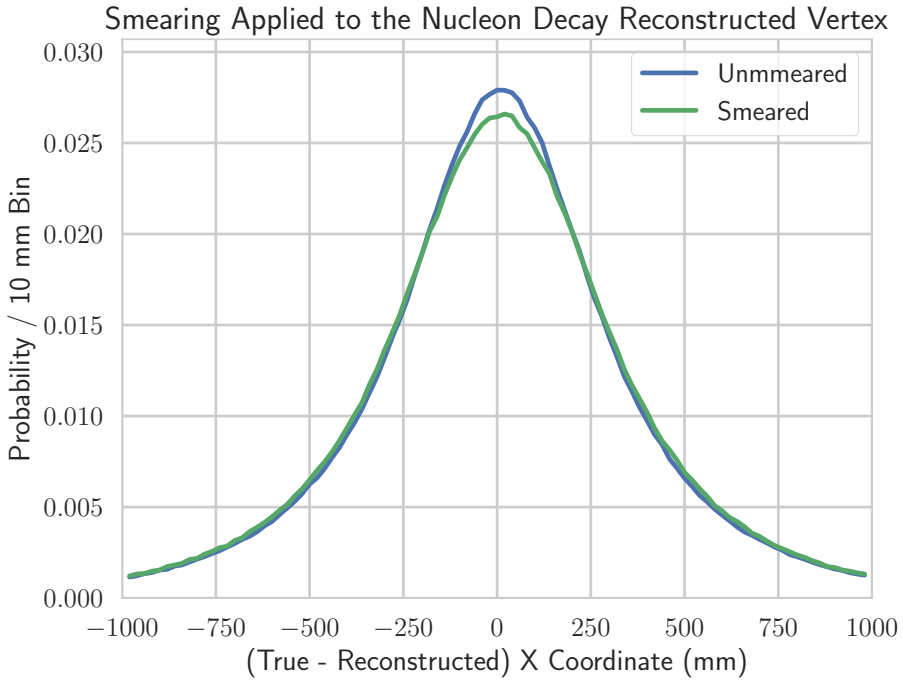

Figure 4.17: Application of vertex smearing showing the overall effect of applying a Gaussian response using the systematics found in table 4.2 to the simulated invisible nucleon decay energy spectrum.

where E' is the new energy and E is the reconstructed energy. The smearing applied uses the difference in the fitted mean $a_{\text{smear}} = a_{\text{data}} - a_{\text{simulation}} = 0.042$ MeV and the fitted resolution $b_{\text{smear}} = \sqrt{b^2_{\text{simulation}} - b^2_{\text{data}}} = 0.086\ \sqrt{\text{MeV}}$. Figure 4.16 shows the application of the smearing determined through ^{16}N calibration on the simulated invisible nucleon decay energy spectrum.

4.6.2 Vertex Smearing

Vertex smearing is applied using the fit parameters from table 4.2. To simplify the result of smearing, only the difference in the Gaussian component is applied to the initial vertex (applied to all three directions independently),

$$\frac{1}{\sqrt{4\pi\sigma^2}} \exp\left[-\frac{1}{2}\left(\frac{x-\mu}{2\sigma}\right)^2\right]. \tag{4.9}$$

This simplification can be made due to the small difference seen between data and simulated data. In the case of large deviation the effects of the tail cannot be neglected. For

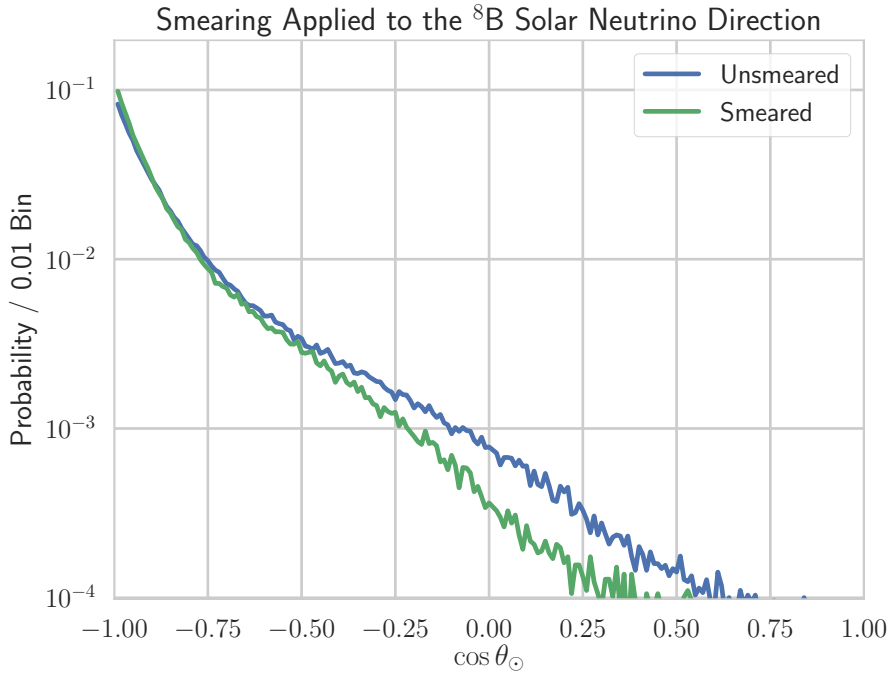

Figure 4.18: Smearing of the dot product of the direction of the sun with the reconstructed direction. Since the only direction parameter used in analysis is this one, it is simpler to smear this parameter alone rather than the actual direction.

each reconstructed vertex, equation 4.9 is sampled in x, y, and z and then added to the initial result where $\sigma_{\text{smear}} = \sqrt{\sigma^2_{\text{simulation}} - \sigma^2_{\text{data}}} = 71.6$ mm. Figure 4.17 shows the application of the smearing on the simulated invisible nucleon decay reconstructed vertex.

4.6.3 Direction Smearing

Unlike the energy and position reconstruction smearing, smearing of direction is not as straight forward. Since the measurable quantity is the dot product of the true direction and reconstructed direction, the observable is bound between $[-1,\ 1]$. Instead of applying a randomized smearing, each simulated event is shifted using a change of coordinates which is systematically applied (preserving the initial randomness of the distribution). Even though the fit to direction used two independent exponential distributions, if one of those exponentials is dominant then a linear transformation can be applied (by assuming the other has a negligible effect). This technique was utilized towards the end of the SNO experiment for low energy threshold analysis [129]. To shift from one exponential

to another (in terms of $\cos\theta$),

$$\cos\theta \to -1 + (\cos\theta + 1)(-b_2/b_1), \tag{4.10}$$

will shift,

$$\frac{b_1 \exp\left[-b_1(\cos\theta + 1)\right]}{1 - \exp\left[-2b_1\right]} \to \frac{b_1 \exp\left[-b_2(\cos\theta + 1)\right]}{1 - \exp\left[-2b_1\right]}. \tag{4.11}$$

Notice here that $\cos\theta \to -\cos\theta$ as compared to the direction fit used previously. This is due to the SNO+ definition of the solar position as as a vector pointing from the center of the detector towards the sun. Using this definition, the dot product of solar neutrino direction with this vector peaks at $\cos\theta = -1$. For the neutron decay analysis, the solar direction is only used as a cut, which allows for values that would surpass the boundary at $\cos\theta = 1$ to be retained in an overflow bin. Figure 4.18 shows the application of the smearing on the simulated ^{8}B solar neutrino elastic scattering direction distribution.

Chapter 5

Nucleon Decay Analysis

As a means to extract the nucleon decay signal from the total signal observed by the SNO+ detector during the live-time of the water phase, it is necessary to model the signal and backgrounds accurately in order to reject as many background events as possible. Due to the relatively poor energy resolution of water Cherenkov detectors and the similarity of the signal and background energy distributions, it is impossible to reject all backgrounds from the analysis, and thus a statistical approach must be taken. Two approaches to extracting the signal statistically will be presented, the first treats the data as a simple counting experiment, and the second is a more complex analysis using a profile likelihood fit to the reconstructed energy and radial position of the event vertex. Due to changing background and detector conditions, the data for the water phase is split into six time periods corresponding to different external and internal background rates. The final nucleon decay analysis will be performed on a blind data set. In order to prevent unblinding the data until the final analysis, this analysis is constrained to roughly 11 days of open data which was taken at the beginning of the water phase data taking.

5.1 Signal

The observed signal is the nuclear deexcitation γ's from the decay of neutrons through invisible channels as shown in section 1.3.4. To model this process the nuclear deexcitation γ's given in table 1.5 are simulated with their respective branching ratios, with the events isotropically distributed throughout the detector. The invisible components of the decay are ignored since they cannot be observed in the detector. The Monte Carlo simulations is done using RAT—a GEANT4 based simulation package built specifically for SNO+. RAT is tuned to accurately model detector related effects, with any discrepancies handled as systematic errors on the final result. Given in figure 5.4 is the simulated reconstructed energy spectrum for n$\rightarrow 3\nu$. The events are expected to be isotropic in the detector since they originate from the detection medium. If no significant signal is detected, then based on the measured amount of background a limit can be set on the lifetime of the neutron (τ_{ndk}) via invisible decay modes by simple counting statistics considerations:

$$N = N_0 e^{-\lambda t} \;\Rightarrow\; \frac{dN}{dt} \sim -N_0\lambda$$

$$\tau_{ndk} > \frac{\epsilon_{ndk} T_l N_0}{\chi}$$

Where ϵ_n is the detection efficiency, T_l is the live time, N_0 is the number of nucleons, and χ is the upper-limit statistic. The approximation $N(t) = N_0$ is made, which is valid in the case that the lifetime is much longer than the measurement time and large N_0, both true for SNO+. The number of neutrons in the detector (filled with water) in an oxygen atom is calculated for the detector volume within the acrylic vessel assuming a sphere of radius $R = 6.005$ meters. Accounting for the isotopic abundance of ^{16}O in the detector,

the total number of neutrons which could produce a signal in the detector are,

$$\begin{aligned} N_0 &= \frac{8\rho_w(\frac{4}{3}\pi R^3)A_O}{N_A M_O}, \\ \rho_w &= 998 \pm 1 \text{ kg m}^{-3}, \\ R &= 6.005 \text{ m}, \\ A_O &= 0.99762(16), \\ M_w &= 18.01528 \times 10^{-3} \text{ kg/mol}, \\ N_A &= 6.022 \times 10^{23} \text{ mol}^{-1}, \end{aligned} \tag{5.1}$$

where A_O is the natural abundance of ^{16}O, and M_w is the atomic weight of water, resulting in a total number of neutrons of

$$N_0 = (2.415 \pm 0.006) \times 10^{32}. \tag{5.2}$$

The density of water is calculated given the average cavity temperature and the increased pressure at SNOLAB due to the depth (~ 1.33 bar).

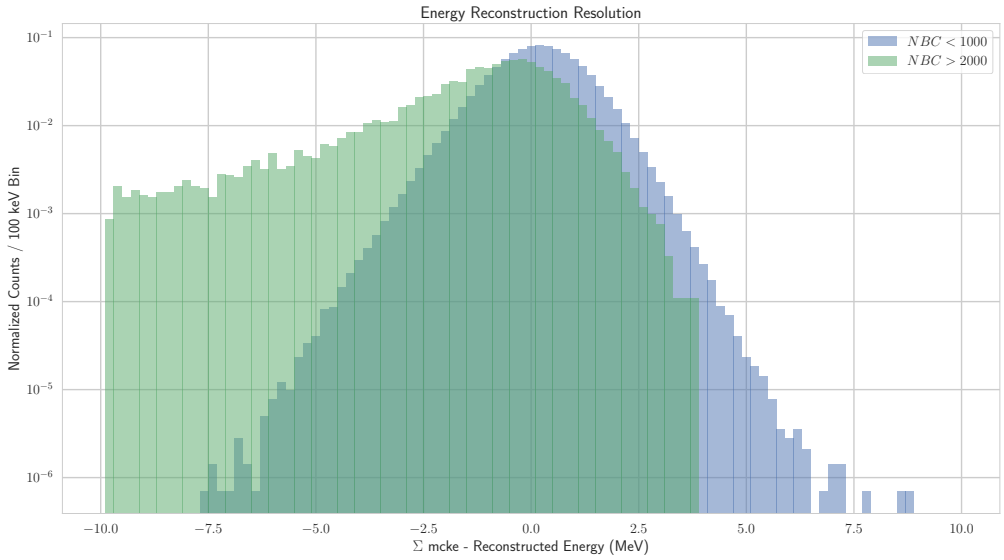

Figure 5.1: Reconstruction bias for the predicted solar spectrum in detector simulations comparing the simulated true kinetic energy to the reconstructed energy. For high NBC the distribution is biased to reconstruct to higher energy and has a very large skew.

5.2 Live Time

In order to assess the total live time for a set of runs, dead time made by data cleaning cuts which veto over significant periods of time must be accounted for. For the SNO+ water phase, these include loss of CAEN digitizer data, burst events, non-physics triggers, and muon followers. As summarized by Li [118], the live time is calculated by subtracting the recorded dead time of a run from the raw live time given by the GPS start and stop time for a run. The live time is further reduced by requiring that the detector be in a normal operating condition throughout the 1-hour run. This excludes runs with electronic breakdowns and runs in which a large part of the detector is off.

5.2.1 Run Selection

In general run selection is made before processing the data using values from the run database corresponding to the detector state at the time of the run. During the run, the detector operator will set a run type which is recorded to a database. These types include maintenance runs, abnormal activity, or even calibration runs. The database also includes

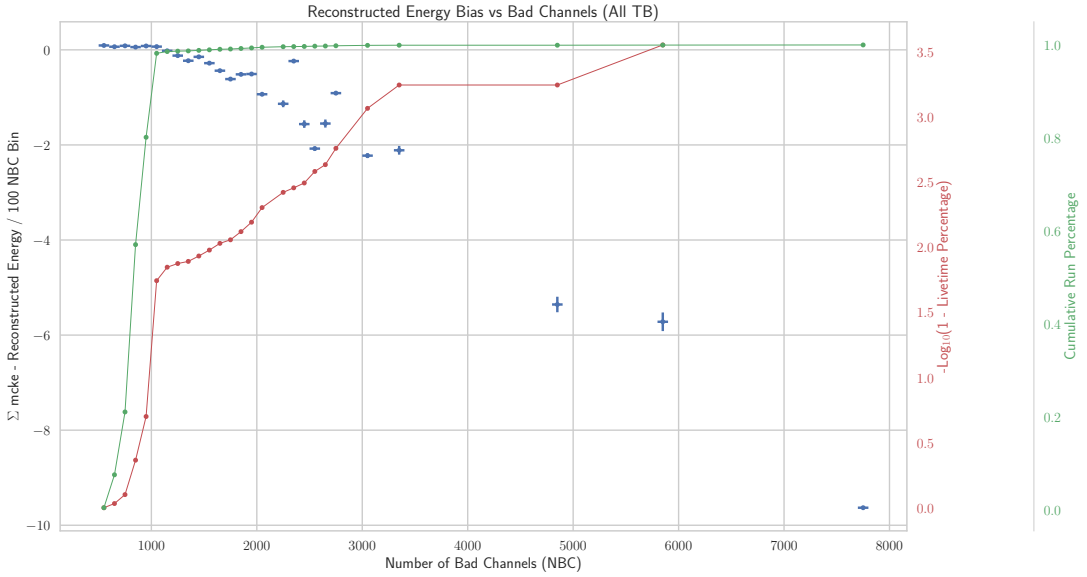

Figure 5.2: Shown in blue is the bias in the reconstructed energy for the solar energy spectrum as a function of NBC showing a flat region for $NBC < 1100$ followed by a somewhat linear descent. The green curve shows the corresponding cumulative distribution of live time for the same data as a function NBC where 98.2% of the live time has $NBC < 1100$.

information from the slow-control system which monitors the cavity temperature, the status of bubblers used for level monitoring, and the status of the magnetic compensation coils. Further checks are made on the run length, and internal clock to remove runs which are out of sync or were cut short for unknown reasons (often caused by breakdowns) [130]. Runs where a significant number of channels were not operating or were flagged as unusable for reconstruction also needed to be removed from the usable data. Channels were tagged as "Bad Channels" if the timing and charge calibration for the channel did not have good calibration points and also if the channel got out of sync during a run due to electronic noise issues. As a quantitative means to justify removing runs from the run list based on the total number of bad channels (NBC), the change in the reconstructed energy bias was investigated as a function of NBC. Shown in figure 5.1 is the difference between the true simulated energy and the reconstructed energy for solar neutrino elastic scattering events. The solar neutrino spectrum was used as a proxy for a flat electron background in order to avoid using additional simulation resources and

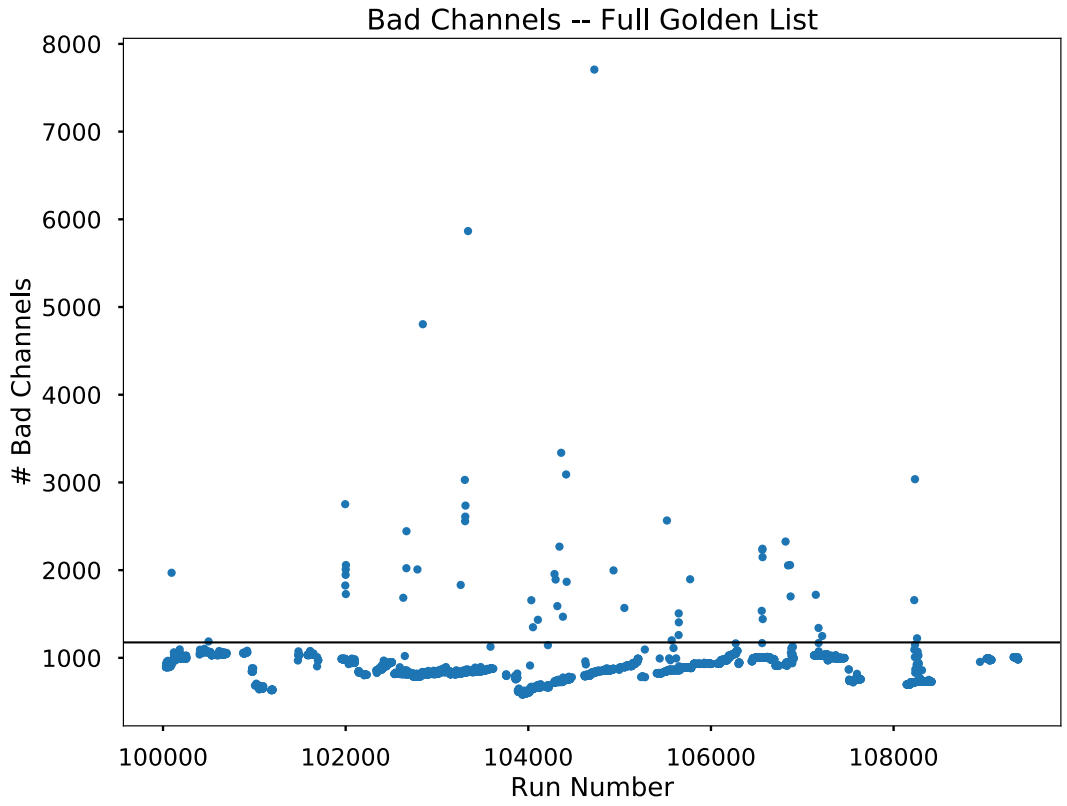

Figure 5.3: Number of bad channels across all of the golden physics runs with the cut at $NBC < 1100$ drawn.

because it provides a spectrum which is isotropic throughout the detector and has a flatter energy distribution as compared with the others which were simulated. A baseline of 800 - 1000 channels is expected for the number of bad channels purely from PMTs which have failed over time. In figure 5.1 runs with $NBC < 1000$ represents the nominal detector state where the energy reconstruction distribution is symmetric and $NBC > 2000$ shows the detector in poor state. Runs were grouped into bins of 100 NBC width and then the distribution of simulated kinetic energy and reconstructed energy was plotted. For each binned distribution, the mean of the distribution is calculated and then plotted in blue in figure 5.2 as a function of NBC. Shown alongside this is the cumulative distribution in green showing the amount of total live time relative to the entire data set as a function of cutting on NBC. A cut is made to accept only runs where $NBC < 1100$, which retains

98.2% of the live time while also minimizing the shift in the reconstructed energy. The effects of this cut can also be seen graphically in figure 5.3.

5.2.2 Cuts to Live Time

The live time cuts which are performed separate from data cleaning sacrifice are:

1. **Retrigger Cut**

   After a global trigger is sent out by the Master Trigger Card there is an intrinsic lockout window of 440 ns before another trigger pulse may be sent out; however, it is unlikely for physics events to occur in such rapid succession frequently. It is more likely the detector retriggers on late light or after pulsing in the electronics. To be conservative, any pair of events that occur within 3 μs of each other are cut.

2. **NHIT Burst Cut**

   Flasher events caused by sparking in the dynode typically occur in bursts. Events which occur between these flashes will be contaminated with light from the flashers and thus need to be cut. The NHIT Burst Cut removes any 6 events within a 6 second moving window which have an NHIT > 40.

3. **CAEN Loss Live Time Cut**

   As a means to look for instrumental bursts in SNO+, a CAEN digitizer is used. When the CAEN buffer fills faster than it can write-out, new events will not have CAEN data. Since waveform data is key to quality monitoring, such events must be removed. In addition, a full CAEN buffer often means a burst of events caused by instrumental noise has occurred. During a burst of events, not all events lose CAEN data but should still be removed from the data. To remove these events, if any 2 events within a 2 ms time window are missing CAEN data, then every event within that time window is also removed.

4. **Muon Followers**

   When a muon is detected, all events for the next 20 seconds are vetoed. At a rate of $\sim$3 muons per hour, this is an average reduction of the live time by a factor of $1/60 \sim 1.6\%$.

5. **Pedestal Cut**

   Every 50 minutes the detector goes into NHIT monitor mode where pedestal events are recorded for detector state monitoring, during this time we cut all events.

5.2.3 Calculated Live Time and Uncertainty

The live time was calculated run-by-run for 284 runs in the data set summing the errors in quadrature for each run to get a total live time of

$$T_l = 11.0682 \pm (1.54 \times 10^{-4}) \text{ days.} \tag{5.3}$$

This live time corresponds to a dead-time of $\sim 4\%$, which is primarily from muons and detector monitoring.

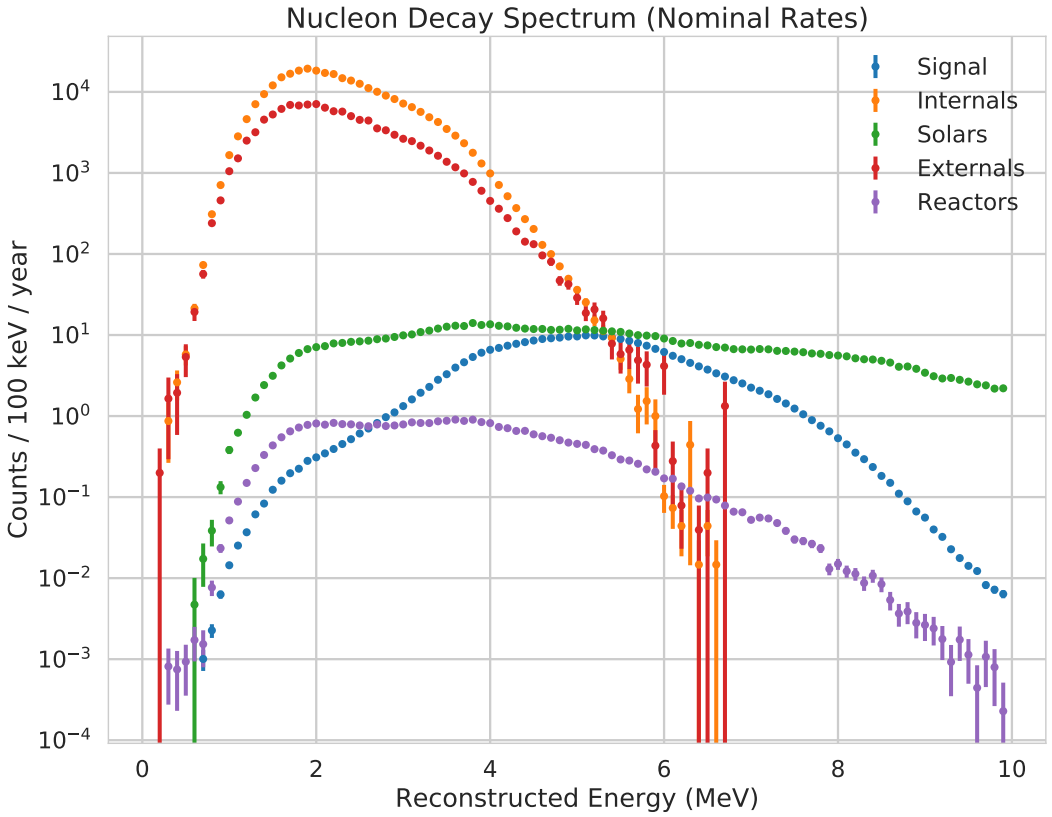

Figure 5.4: Neutron decay signal spectrum within a 5.5 m fiducial volume set to the KamLAND upper limit of $\tau = 5.8 \times 10^{29}$ years compared with the expected backgrounds at their nominal rates given in table 5.1.

5.3 Backgrounds

The backgrounds discussed in chapter 3 need to be determined for the run period of this analysis. The solar neutrino flux and reactor anti-neutrino flux have predictions based upon auxiliary measurements and theoretical calculations, whereas the internal and external radioactivity can be constrained through an energy spectrum side-band analysis. Nominal rates of radioactivity were calculated [26] and used as a first estimate of relevant backgrounds based on external measurements prior to running. Samples of the rope were measured in a High Purity Germanium detector to assess their contribution to the total background rates. The water was assayed using ex-situ measurements sampled during recirculation [26] to assess the total background contribution from Uranium and Thorium.

The sources of radioactivity within the detector are simulated for various components of the detector as well as for the water. The primary contributions come from dust which has collected on the acrylic vessel during the construction phase, the acrylic vessel itself, the hold-up and hold-down ropes which hold the acrylic in place and the water inside and outside of the acrylic vessel. Detector simulations are done for the various detector components with their expected rates for each of the time periods. Instead of fitting each of the components individually, the components where combined at their nominal rates into single components for the likelihood and counting analysis. All external radioactivity backgrounds are grouped together into a single background: *Externals*. All internal radioactivity backgrounds are grouped together into a single background: *Internals*. Solar ν_e, ν_μ, and ν_τ are grouped into *Solars*, and all reactors are grouped together into *Reactors*. The expected background as a function of energy using the nominal rates of table 5.1 is shown in figure 5.4.

5.3.1 Run Periods

During running, it was noted that some backgrounds were not distributed uniformly in time. This was likely due to an ingress of radon at the top of the detector which diffused and decayed throughout the outer volume. Due to the fact that the state of the backgrounds and the detector itself changed over time, the data is split into time periods which have separate cuts applied. While there are six distinct time periods, this analysis uses only the initial two weeks of data since the rest of the data will be used in a blind analysis. The first two weeks constitutes all of period 1 and some of period 2. Table 5.2 shows the contribution of each time period in terms of live time. Time period 1 corresponds to a time when a large excess of external backgrounds was seen near the top of the detector. During period 2 water recirculation was changed to move water throughout the cavity causing the event distribution to drop towards the equator of the acrylic vessel as the events diffused through the water. In period 3 the recirculation scheme was changed back to the scheme of period 1, and the event excess retreats back towards the top of the detector. Period 3 is the cleanest in terms of detector run conditions. Period 4 and 5 mark a period where pump failure forced a change in the recirculation scheme once again

Isotope	Source	Rate (per day)	Rate (per day) After Cuts
^{214}Bi	Internal Water	33972	0.886
^{214}Bi	Hold Down Ropes	11123	~ 0
^{214}Bi	Hold Up Ropes	2285	~ 0
^{214}Bi	External Water	361643	0.047
^{214}Bi	Acrylic Vessel	35068	10^{-2}
^{214}Bi	Acrylic Dust	2237	4×10^{-3}
^{208}Tl	Internal Water	400	0.169
^{208}Tl	Hold Down Ropes	6356	~ 0
^{208}Tl	Hold Up Ropes	1309	~ 0
^{208}Tl	External Water	10740	5×10^{-3}
^{208}Tl	Acrylic Vessel	4110	0.028
^{208}Tl	Acrylic Dust	1328	~ 0
ν_e	Solar	8.2	0.100
$\nu_\mu + \nu_\tau$	Solar	2.5	0.055
$\bar{\nu}_e$	Reactors	0.48	10^{-2}
Total			1.315

Table 5.1: Nominal background rates for the SNO+ water phase calculated based on expectations from SNO and background models [26]. Solar neutrino and reactor anti-neutrinos are shown unoscillated (but with cross-sections taken into account). The last column contains only reconstructed events, with cuts applied from table 5.3.

Bin	Name	Run Range (10XXXX)	Golden Run Count	Duration (h)
1	Open	0 - 399	131	127.10
2	Hot-spot	400 - 2048	385	378.76
3	Steady-state	2049 - 3403	797	797.77
4	AV 1+2	3408 - 4329 (AV 1)	770	759.66
		4331 - 5171 (AV 2)		
5	AV 3+4	5493 - 5661 (AV 3)	302	299.32
		6070 - 6499 (AV 4)		
6	Post Bubble	6716 - 8416	302	299.32
Total			2989	2942.97 (115.6 days)

Table 5.2: Time periods used in the nucleon decay analysis from Lozza [27]

and a large excess of events began to appear below the acrylic vessel and work its way up through the water. As the region of excess of events travel from the bottom towards the top of the detector, different cuts on the fiducial volume are applied. Time period 6 marks all runs after the excess of events had dissipated.

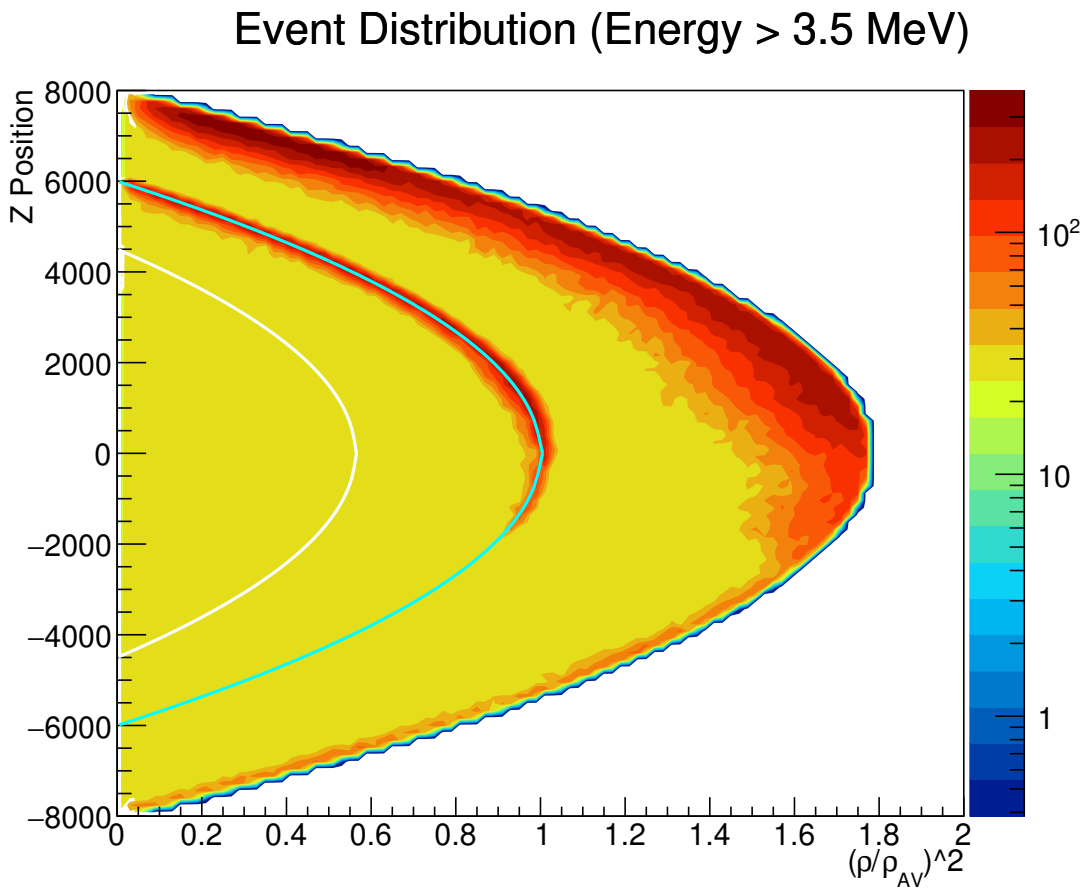

Figure 5.5: Distribution of events within the detector from data showing a large excess of events in the water in the top half of the detector between the acrylic vessel and the photomultiplier tubes. Many events also reconstruct directly to the acrylic vessel due to a bias in the fitter for events near the edge of the vessel. The cyan curve shows the location of the acrylic vessel, while the white curve shows a 4.8 m fiducial volume.

5.4 Event Selection

Prior to analysis, event selection is performed to optimize the sensitivity to the signal. Event selection for a counting experiment and a likelihood fit are not necessarily the same, especially when cuts involve parameters used in the likelihood fit. Examples of event selection cuts include energy range and fiducial volume, as well as cuts based on the direction of the sun and the figures of merit from reconstruction as discussed previously in section 3.4.1. Cuts are also required which remove events which may not be accounted for in the model, such as excess of events in any given region of the detector. As is shown in figure 5.5, there is an observed non-uniformity in background events in the water external

Energy	Radial Position	Solar Direction	In Time Ratio	β_{14}
$4.4 < E < 9.0$	$R < 4.8$ m	$\cos\theta_{\mathrm{SUN}} > -0.8$	$ITR > 0.55$	$-0.12 < \beta_{14} < 0.95$

Table 5.3: High level cuts used for event selection in the first 11 days of open physics data for the likelihood analysis.

to the AV in the upper half of the detector. This high rate of external background events forces the fiducial volume to decrease as compared to initial studies which assumed the nominal backgrounds. The radius of the fiducial volume was decreased from 5.5 m to 4.8 m. The energy range was selected to allow a accurate fit to the external and internal backgrounds in the likelihood fit with the lower bound set by uncertainties in the data cleaning contamination at low energy. The energy window was also chosen such that ^{16}N calibration data provides a good estimate of the energy fit parameters. Events where the energy, position, or direction fitter did not converge were removed for this analysis. Cuts made based on the in-time ratio and the β_{14} isotropy parameters are also included using values used during SNO and are confirmed to still perform well with new ^{16}N data. Cuts used for this analysis are summarized in table 5.3.

5.5 Simple Counting Experiment Analysis

The simplest method of analyzing the data is to perform a counting experiment. Simply put, from the probability distributions generated through detector simulation, a set of optimized cuts is determined for the observables and the number of events remaining is compared with the estimated background contribution. Such an analysis is simple to perform and understand, but neglects a significant amount of event information by treating all events within the box as equal. The probability of observing N events, where the expected number of events is a sum of signal and background $(S+B)$, is given by the Poisson distribution:

$$\mathcal{P}(N) = \frac{e^{-(S+B)}(S+B)^N}{N!}, \tag{5.4}$$

for a fixed $S+B$. Equation 5.4 is normalized for all possible values of the measured event number N. Since the expected signal (S) is the parameter of interest this distribution can be modified via Bayes' theorem (with a flat positive definite prior for S) to form the probability of measuring S signal events given N observed events:

$$\mathcal{G}(S) = A\frac{e^{-(S+B)}(S+B)^N}{N!}, \tag{5.5}$$

where A normalizes $\mathcal{G}(S)$ to unity for all $S > 0$. In this case, the background rate is assumed to be known well, in which case the best estimator for the expected signal is simply the difference in counted events N and the expected backgrounds. Since the signal is expected to be zero, a single sided confidence interval at confidence α is found by integrating the probability distribution from equation 5.5:

$$\alpha = \int_{-\infty}^{S_\alpha} \mathcal{G}(S)\,\mathrm{d}S\,. \tag{5.6}$$

The quoted upper limit on the measurement is the value of S_α which satisfies this condition [131, 132].

5.5.1 Feldman-Cousins Interval

A common problem when choosing confidence intervals is that the interval chosen is not unique. A few examples of common intervals to quote are upper limit, lower limit, mode centered, and central value. Upper limits at confidence α for a probability distribution

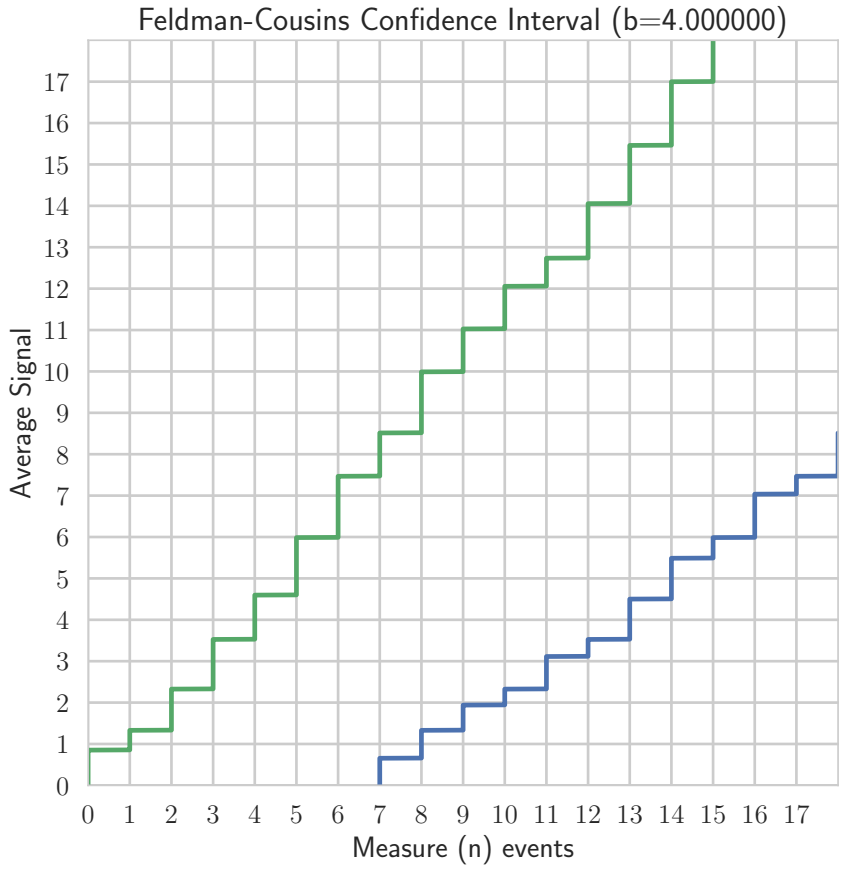

Figure 5.6: Example Feldman-Cousins confidence bands for an experiment with an expected background of 4 events at a confidence level $\alpha = 0.90$. For a given measurement of total events in a counting experiment n, confidence belt is between the blue curve (lower bound) and green curve (upper bound).

$\mathcal{P}(x)$ would cover the bounds $x = \infty$ to x_{upper} where $\alpha = \int_{-\infty}^{x_{\text{upper}}} \mathcal{P}(x)\,\mathrm{d}x$. Lower limits at confidence α would then be defined by integrating in the opposite direction as to only contain the higher values of x: $\alpha = \int_{x_{\text{lower}}}^{\infty} \mathcal{P}(x)\,\mathrm{d}x$. In general, any set of x_a and x_b such that $\alpha = \int_{x_a}^{x_b} \mathcal{P}(x)\,\mathrm{d}x$, would satisfy the condition that the confidence interval defines the set of experiments which contain the true value of x at confidence α. In fact, the confidence interval does not necessarily have to be continuous, though in practice breaking up a confidence interval is never done. For an experimental analysis, the method of selecting a confidence interval must be chosen a priori to avoid biasing the result and to make comparison with other experiments easier. If an experiment does not know whether a signal will be observed or not, a single sided confidence interval is often used which covers $-\infty$ to x_{upper}. However, if the measurement is made and a signal is observed which is statistically significant then it is desirable to choose a confidence interval (as suggested by Neyman [133]) which covers the central interval such that the probability on either side of the central values is equally covered. For a desired confidence level α, the Neyman two-sided confidence bands takes the form,

$$\alpha_R = \alpha_L = (1 - \alpha)/2, \tag{5.7}$$

where α_L is the coverage below the lower limit, and α_R is the coverage above the upper limit. In the case of setting an upper limit only at confidence level α, one would simply choose $\alpha_R = 1 - \alpha$ and $\alpha_L = 0$. An obvious problem occurs from such a treatment in that there is a discontinuity when switching from one treatment to the other, which Feldman and Cousins proposed to solve as follows [134]. Instead of integrating the probability distribution, calculate the likelihood ratio given by:

$$\lambda(s) = \mathcal{P}(D|s)/P(D|s^*), \tag{5.8}$$

where s^* is the best estimate of s, and $\mathcal{P}(D|s)$ is the probability of a particular outcome D given s. The values are then ordered in decreasing values of $\lambda(s)$ (rather than in increasing value of s) and then integrated to the desired confidence level, choosing the outermost points of s as the confidence interval. This construction provides a smooth continuation from limit setting to detection without biasing the interpretation after the measurement

is made. Figure 5.6 shows a sample Feldman-Cousins confidence grid for an expected background count of 4. For a measurement (along the bottom axis), the region bound by the blue (lower confidence) and green (upper confidence) defines the confidence of a particular measurement.

5.6 Likelihood Analysis

A more comprehensive approach to analyzing the data allows using the information lost by the counting experiment to set stronger constraints on the backgrounds based on the observed spectrum of selected observables. This is achieved by building a likelihood function of the model parameters (expected number of signal and background events)given the observables,

$$\boldsymbol{\theta} = [E, |\vec{r}|, \vec{u} \cdot \vec{r}, \vec{u} \cdot \vec{r}_{\odot}], \tag{5.9}$$

where E is the reconstructed energy, $\vec{r}$ is the reconstructed position, $\vec{u}$ is the unit vector in the reconstructed event direction, $\vec{r}_{\odot}$ is the unit vector in direction of the sun relative to the SNO+ detector. The model takes into account the expected background as well as the detector response. Each of the expected backgrounds is simulated with detector Monte Carlo simulation using RAT. The probability distributions are then extracted from the simulation, labeled here as $\mathcal{P}_b(\boldsymbol{\theta})$ for each background b. The same procedure is performed for the neutron decay signal separately to produce $\mathcal{P}_s(\boldsymbol{\theta})$. The full PDF takes the form,

$$\mathcal{P}(\boldsymbol{\theta} \mid N_s, \boldsymbol{N_b}) = [N_s \mathcal{P}_s(\boldsymbol{\theta}) + \sum_b N_b \mathcal{P}_b(\boldsymbol{\theta})]/(N_s + \sum_b N_b) \tag{5.10}$$

for signal count N_s and background count $\boldsymbol{N_b}$. From this probability distribution a likelihood function is built from the joint probabilities of n independent and identically distributed observations [135] [136].

$$\mathcal{L}(N_s, \boldsymbol{N}_b|\boldsymbol{\theta}) = \prod_{i=1}^{N} \mathcal{P}(\boldsymbol{\theta}|N_s, \boldsymbol{N_b}) \tag{5.11}$$

5.6.1 Extended Likelihood

The likelihood in equation 5.11 assumes a fixed number of total events N; however, due to the statistical nature of the experiment at hand, the likelihood should be extended to account for variation in the total event rate. The likelihood gains an additional multiplicative term based on a Poisson distribution due to the stochastic nature of the measurement.

$$N = N_s + \sum_b N_b \tag{5.12}$$

$$\mathcal{L}(N_s, \boldsymbol{N}_b|\boldsymbol{\theta}) = \frac{\nu^N}{N!}e^{-\nu}\prod_{i=1}^{N}\mathcal{P}(\boldsymbol{\theta}|N_s, \boldsymbol{N_b}) \tag{5.13}$$

Where ν is the expected number of events.

5.6.2 Constrained Backgrounds

It is possible to allow the normalizations on the backgrounds to float, and thus provide simultaneous fits to all of the background rates and the signal rate. This method ignores the fact that there is possible prior knowledge on the background rates through side-band analysis and auxiliary measurements. These prior measurements are incorporated by adding constraint terms into the likelihood function based on the expected backgrounds and the uncertainty on those expectations. This takes the form of a Poisson distribution for small background rates, which becomes Gaussian in the large asymptotic limit. The likelihood function thus takes the form,

$$\mathcal{L}(N_s, \boldsymbol{N}_b|\boldsymbol{\theta}) = \frac{\nu^N}{N!}e^{-\nu}\prod_{i=1}^{n}\mathcal{P}(\boldsymbol{\theta}|N_s, \boldsymbol{N_b})\prod_{b}\text{Gauss}(\hat{N}_b, N_b, \sigma_b) \tag{5.14}$$

where $\hat{N}_b$ is the expected number of background events, σ_b is the uncertainty on $\hat{N}_b$, and the Gaussian term is defined as:

$$\text{Gauss}(N_b, \hat{N}_b, \sigma_b) = \frac{1}{\sqrt{2\pi\sigma_b^2}}\exp\left\{\left(-\frac{(N_b - \hat{N}_b)^2}{2\sigma_b^2}\right)\right\} \tag{5.15}$$

The addition of constraint terms (as opposed to fixing the backgrounds) provides a means to propagate the systematic uncertainties associated with the measured backgrounds into the likelihood function, which through profiling (discussed next) propagates those uncertainties into the final result.

5.6.3 Likelihood Ratio

For a measured set of data, the likelihood function is minimized with respect to the model parameters, $\boldsymbol{N_b}$ and N_s; however, in many cases only a subset of these parameters are of interest with the remaining parameters considered "nuisance" parameters. The nuisance parameters can be marginalized through the use of a so-called profile likelihood function which integrates out the nuisance parameters resulting in a one-dimensional likelihood

distribution in N_s,

$$\mathcal{L}_p(N_s|\boldsymbol{\theta}) = \mathcal{L}(N_s, \hat{\hat{\boldsymbol{N}}}_{\boldsymbol{b}}(N_s)|\boldsymbol{\theta}) \tag{5.16}$$

where $\hat{\hat{\boldsymbol{N}}}_{\boldsymbol{b}}$ denotes the profiled values of the parameters $\boldsymbol{N_b}$, defined as the values that maximize $\mathcal{L}$ for the specified N_s [30]. The profile likelihood function is then used to construct a likelihood ratio comparing the neutron decay hypothesis with the null hypothesis (background only). Following the Neyman-Pearson lemma, the likelihood ratio is defined [137][138].

$$\Lambda_p(N_s) = \frac{\mathcal{L}(N_s, \hat{\hat{\boldsymbol{N}}}_{\boldsymbol{b}}(N_s)|\boldsymbol{\theta})}{\mathcal{L}(\hat{N}_s, \hat{\boldsymbol{N}}_{\boldsymbol{b}}|\boldsymbol{\theta})} \tag{5.17}$$

The numerator in equation 5.17 is the profile likelihood function 5.16, while the denominator is the likelihood function evaluated at the maximum likelihood estimates $\hat{N}_s$, and $\hat{\boldsymbol{N}}_{\boldsymbol{b}}$. For ease of computation, it is often best to deal with the minimization of the negative log-likelihood instead of maximizing the likelihood. The results of the negative log likelihood and the negative log likelihood ratio for a sample experiment are shown in figure 5.7.

5.6.4 Confidence Intervals

Maximization of the likelihood function 5.16 returns an estimation of the parameter $\hat{N}_s$, whose uncertainty can be estimated from the likelihood ratio 5.17. The interpretation of the result can be as a frequentist limit or used with a Bayesian prior. It should be pointed out that if the expectation for the signal truly is zero, as in the null hypothesis, then when one does an infinite ensemble of experiments, the population mean should also be zero. For this to be true in the case of a signal with a statistically fluctuating background, the maximum likelihood estimate for the number of counts will inevitably be negative. This is often a point of contention, but it is generally accepted that one's choice in the matter is of no consequence as long as the author carefully reports their method for defining confidence intervals, and preferably also publishes the likelihood distribution [30]. Shown in figure 5.8 are distributions using two techniques as discussed by Cowan [136]. Each of these assumes a desired 90% confidence interval α, and in this case, an upper limit interval S_{90}.

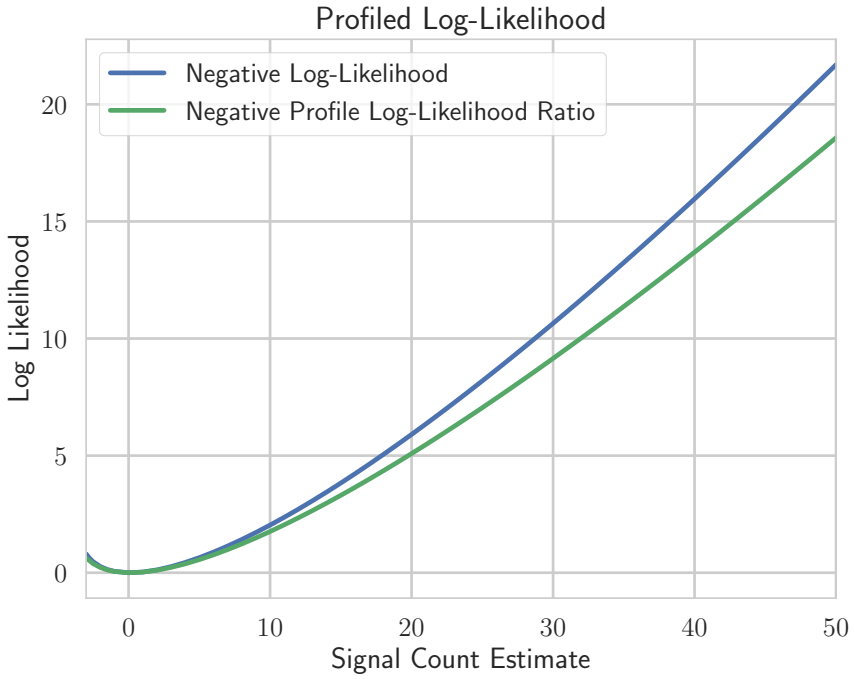

Figure 5.7: The negative log-likelihood, adjusted such that the minimum is moved to zero, is shown in blue. The profile negative log-likelihood ratio is shown in red. The broader distribution of the profiled likelihood is the result of the systematic uncertainties which were folded into the likelihood through the use of constraining probability distributions. The result is a wider confidence interval for the profiled likelihood distribution which correctly accounts for the systematic uncertainties associated with the background fits (nuisance parameters).

$$\alpha = \frac{\int_{-\infty}^{S_{90}} \Lambda_p(N_s) dN_s}{\int_{-\infty}^{\infty} \Lambda_p(N_s) dN_s} \tag{5.18}$$

For a frequentist interpretation, the interval α represents a window in which there is a 90% probability of containing the true value of N_s. This is a straight-forward interpretation, but has the side effect that for an expected value of $N_s = 0$, 10% of experiments will yield an unphysical (negative) confidence band. One could then obviously choose to expand their confidence window up to 95% or 99%, but this is bad practice and tuning of confidence intervals can result in a confidence limit that is more precise than the actual measurement [136]. A second option is to apply a so-called shifted frequentist limit, whereby one takes negative fit values and shifts them up to zero, but maintains the confidence interval set by the maximum likelihood estimate at that negative value. This

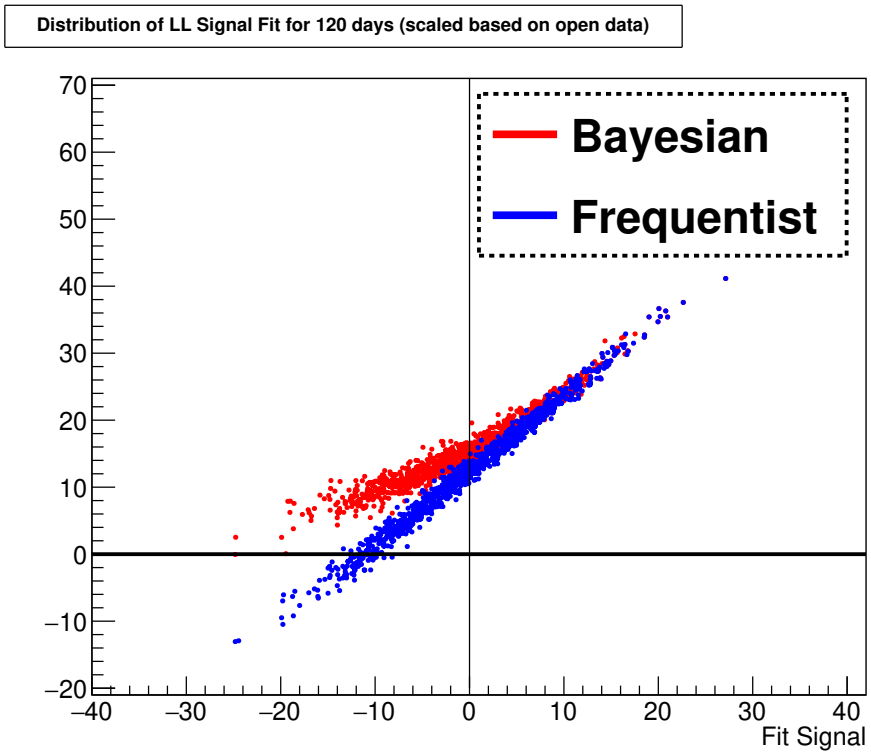

Figure 5.8: Comparison of a purely frequentist result allowing the signal count to float from $-\infty$ to ∞ with the limit set assuming a flat positive definite Bayesian prior.

produces a confidence interval that no longer can be interpreted as containing the true value 90% of the time, and thus should be avoided. Finally one can introduce a Bayesian prior, turning the likelihood ratio into a probability distribution via Bayes' theorem.

$$\alpha_{Bayes} = \frac{\int_{-\infty}^{S_{90}} \Lambda_p(N_s)\pi(N_s)dN_s}{\int_{-\infty}^{\infty} \Lambda_p(N_s)\pi(N_s)dN_s} \tag{5.19}$$

Many choices on a prior can be made, but for this analysis an appropriate choice is a flat positive definite prior.

$$\pi(N_s) = \begin{cases} 1 & N_s \geq 0 \\ 0 & N_s < 0 \end{cases} \tag{5.20}$$

The result from an ensemble of fake experiments can be used to compare the limits set by a likelihood fit and a counting experiment. The expectation is that the two will show some correlation from statistical uncertainties but will have variation due to the loss of information in the counting experiment (the result from a counting experiment does not

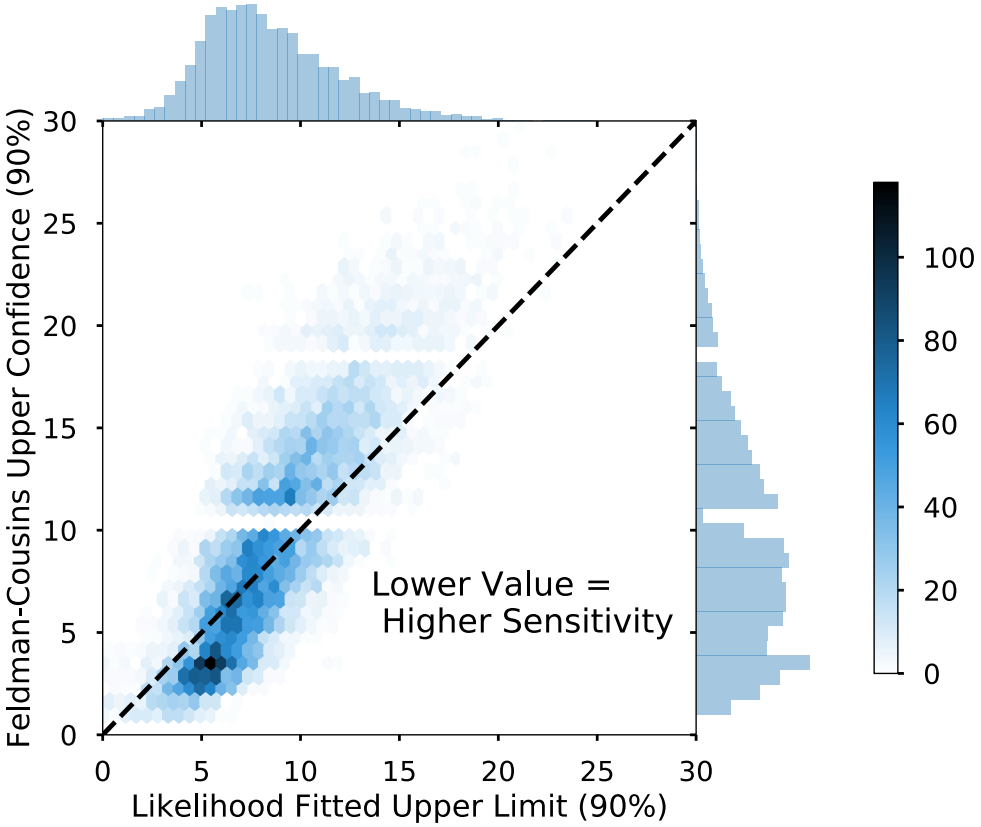

Figure 5.9: Comparison of a Poisson counting experiment along the vertical axis and a likelihood fit along the horizontal axis for a set of 10,000 fake experiments. The two techniques show good agreement for the population of experiments.

vary for a fixed number of events). Figure 5.9 shows the spread in results comparing the Feldman-Cousins upper confidence limit with the integrated likelihood limit for a flat positive definite prior distribution.

5.6.4.1 Bias

As a test of the statistical robustness of an analysis method, a useful quantity to calculate is the bias resulting from that method when applied to an ensemble of experiments. When applying the frequentist principle, confidence intervals are a measure of the relative frequency of which the true value of a parameter is within the stated interval. In principle when using Monte Carlo simulation the value put in as the true parameter will be the result given by a likelihood fit on average. This is only true in the asymptotic limit in the number of experiments and events. Any bias can be determined by comparing the fitted

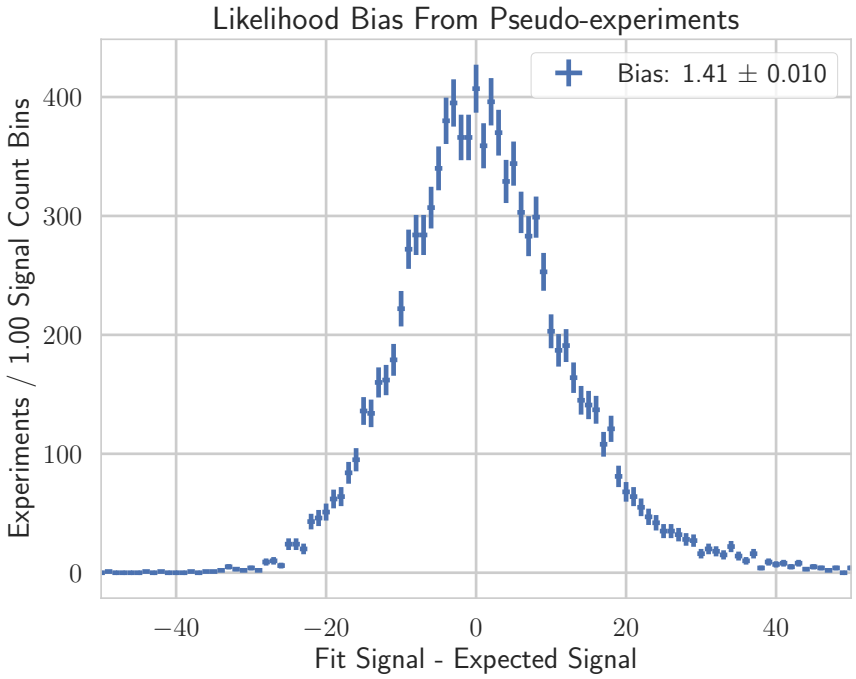

Figure 5.10: Bias in the fit result from an ensemble of fake experiments defined as $N_{sig} - \hat{N}_{sig}$ where N_{sig} is the fit to the number of signal events and $\hat{N}_{sig}$ is the expectation value.

value against the expectation,

$$\text{Bias}(\hat{n}) = E[\hat{n}] - n, \tag{5.21}$$

which is plotted in figure 5.10 for an ensemble of 10,000 fake experiments. The total bias is slightly positive but small with respect to the width.

5.6.4.2 Pull

To understand the size and effect of a statistical bias, the pull distribution can give a more meaningful number which can be compared more directly to varying sample sizes. Pull is similar to bias but each event is normalized by the width of the likelihood distribution for that event. Pull is defined as

$$\text{Pull}(\hat{n}) = \frac{E[\hat{n}] - n}{\sigma}. \tag{5.22}$$

For an asymmetric error in the likelihood distribution, σ can be split into positive and negative errors (σ^+, and σ^-), where the σ^+ is used for values of $n < E[\hat{n}]$ and σ^- is used for

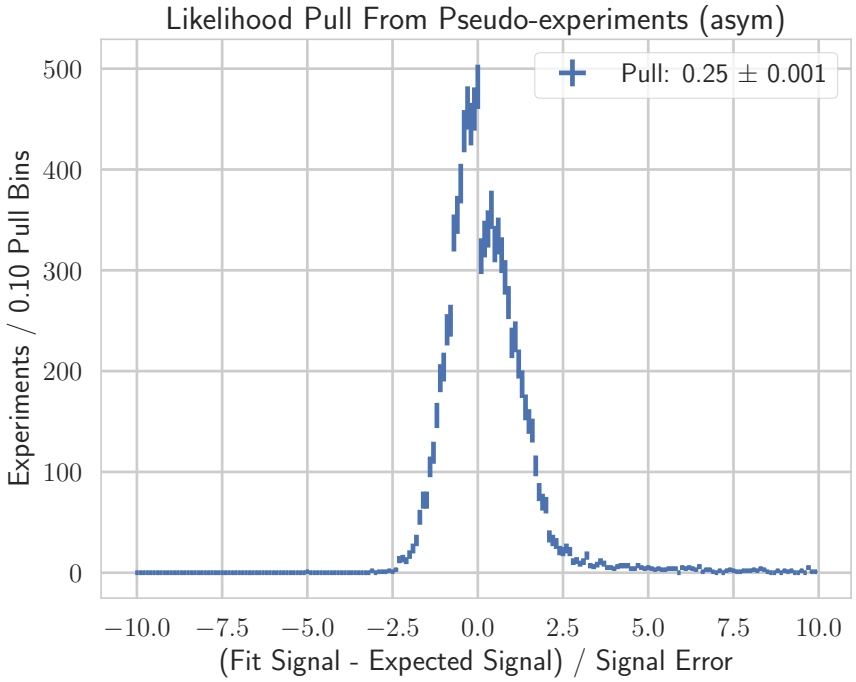

Figure 5.11: Pull in the fit result from an ensemble of fake experiments defined as $(N_{sig} - \hat{N}_{sig})/\sigma$ where N_{sig} is the fit to the number of signal events, $\hat{N}_{sig}$ is the expectation value, and σ is the error on the fit. To incorporate asymmetric errors, σ^+ is used when $N_{sig} < \hat{N}_{sig}$ and σ^- is used when $N_{sig} > \hat{N}_{sig}$, this causes a discontinuity in the distribution at $\hat{N}_{sig}$ but contains the correct coverage.

values of $n > E[\hat{n}]$ to ensure proper coverage. The pull distribution can be easily compared for various likelihoods with respect to a Gaussian distribution. For a Gaussian distributed random variable, the pull is itself a Gaussian distribution with $\sigma = 1$. Therefore the coverage of the confidence intervals can be determined through the integral of the pull distribution for interval $\pm\sigma$. Figure 5.11 shows the pull distribution for a sample of 10,000 fake experiments for this likelihood distribution with a discontinuity at the origin coming from the use of asymmetric errors. The coverage from integrating the range corresponding to 90% of a Gaussian distribution yields 90.25% implying that the likelihood has good coverage.

5.6.4.3 Coverage

Coverage can also be determined directly by counting the percentage of fake experiments with confidence intervals containing the true value of the parameter of interest. The result

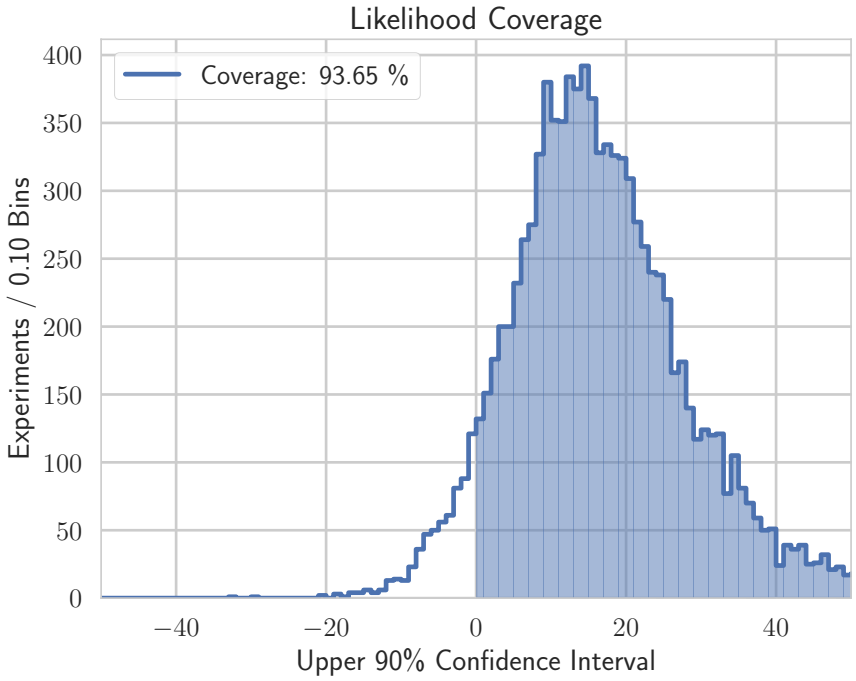

Figure 5.12: Plot of the upper limit on signal count determined by the likelihood fit to 10,000 fake experiments, with 93.65% of fake experiments containing the true value (implying over coverage).

of such an analysis is shown in figure 5.12, which shows a slight over coverage by the likelihood. Ideally the coverage would be exactly the stated confidence interval; however, an over coverage is often preferred to an under coverage since that would represent a more conservative estimate of the confidence interval.

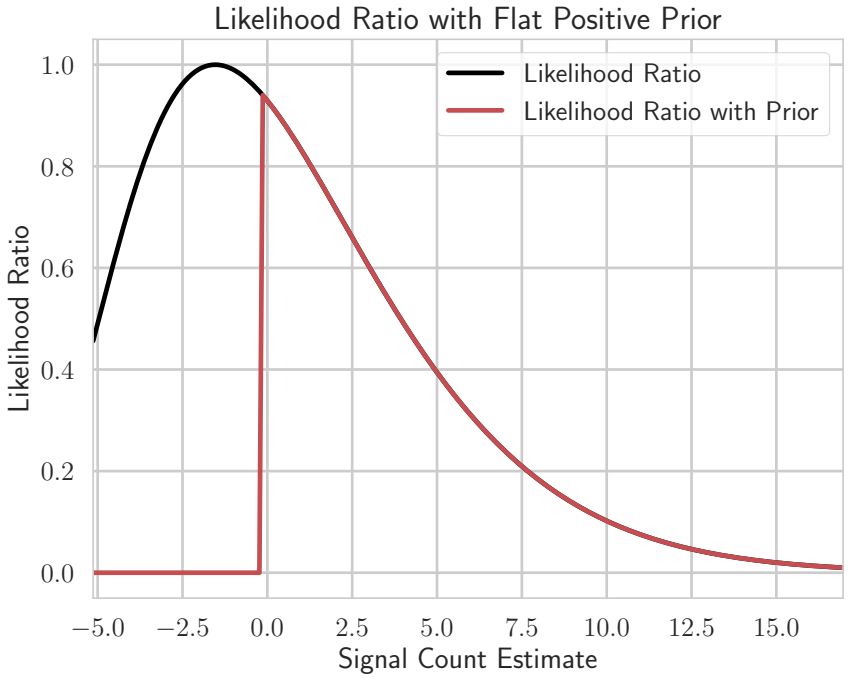

Figure 5.13: Sample profile likelihood distribution from Monte Carlo. Black is the full profile likelihood ratio, while red is with a flat positive definite prior.

5.7 Signal Extraction

The likelihood function described above was used to analyze the unblinded data at the beginning of physics data taking, as the decision to unblind the full data set has yet to be made. Due to the limited statistics, the decision was made to include the side-band into the likelihood fit (simultaneously fitting the internal and external backgrounds with the neutron decay signal). The likelihood ratio is shown in figure 5.13 for the fit to data after profiling the backgrounds. The results of the likelihood fit are shown in figure 5.14. Which corresponds to a neutron lifetime via invisible decay modes of

$$\tau_{ndk} > 1.05 \times 10^{29} \text{ years at } 90\% \text{ C.L.}. \tag{5.23}$$

Of particular note, due primarily to the observed excess of external radon events, the measured background events due to radioactivity is about a factor of 10 higher than the nominal levels. The result on the preliminary data set is within a factor of two of the original SNO result (2×10^{29} years) using heavy water, and is roughly a factor of 6 lower

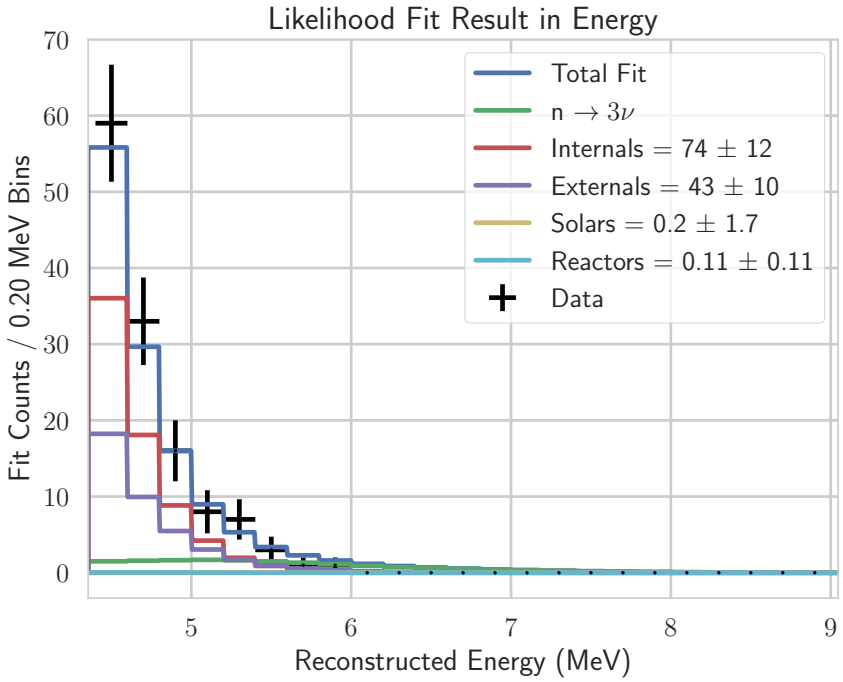

Figure 5.14: Profile likelihood fit to the energy spectrum of the SNO+ unblinded data set. Internal and External background constituents are grouped together assuming nominal ratios, and Solar neutrinos are grouped together.

than the world leading result set by KamLAND (5.8×10^{29} years).

Chapter 6

Scintillator Phase Preparation

The second and third phase of the SNO+ experiment replaces the water in the acrylic vessel with liquid scintillator that must be of high purity. Not only must the scintillator be optically pure and free of contaminants, it must also be radioactively clean. In order to achieve this goal, many steps in the manufacturing process are specifically designed for SNO+ in order to deliver a relatively clean initial product. This initial product is then processed in an on-site custom distillation plant which then delivers the cleanest possible product directly into the detector. A dedicated team of process engineers oversaw the construction and cleaning of the plant, and are currently commissioning the plant to be ready for distillation upon scintillator delivery.

6.1 Distillation Plant

The distillation plant is designed to handle the distillation of both linear alkylbenzene (LAB) and 2,5-diphenyloxazole (PPO), which are then proportionally mixed before being injected into the acrylic vessel—displacing the water through the bottom. LAB is an organic compound often used as an intermediate in the production of surfactants for use in detergents. The LAB acts as a bulk solvent for PPO—the SNO+ fluor of choice. SNO+ will combine these two at a ratio of 2 grams of PPO per liter of LAB to form the scintillator [139]. LAB was selected because of its long time stability, compatibility with acrylic, high purity levels directly from the manufacturer, long attenuation and scattering length, high light yield, and linear response in energy [103]. Additionally, the high flash point and low toxicity makes its transport and use underground safer.

6.1.1 Design Overview

The scintillator plant is designed to purify the LAB to at least the same purity as was done by the Borexino experiment of about 10^{-17}g/g_{LAB} for both ^{238}U and ^{232}Th. The scintillator plant is separated into three distinct operations: Distillation, Water Extraction, and Stripping. Each of these is designed to reduce the internal U, Th, and K contamination and improve overall optical properties. The design for the plant was custom made by Koch Modular Process Systems(KMPS)[140], the same company that designed a similar system for Borexino [141] to fit the unique requirements set by SNO+. The primary requirement was to construct the distillation plant underground near the detector so that clean product would not need to travel far before entering the detector, and LAB could also be extracted and re-purified directly from the detector. LAB arrives in 20-tonne batches at the surface where 3-tonne rail tankers are filled and used to transport it underground. This LAB is then stored in 60-tonne tanks underground prior to distillation. Flow from the 60-tonne tanks is expected to be continuous, so the distillation plant was designed operate in a continuous mode—as opposed to distilling in batches as is done in the alcohol industry. The designed flow rate allows continuous operation at a rate of 1000 kg/hour. Detector fill is limited by the rate at LAB can be delivered underground. With at most 6 rail tankers per day—each holding about 2.2 tonnes of LAB—the detector could fill in

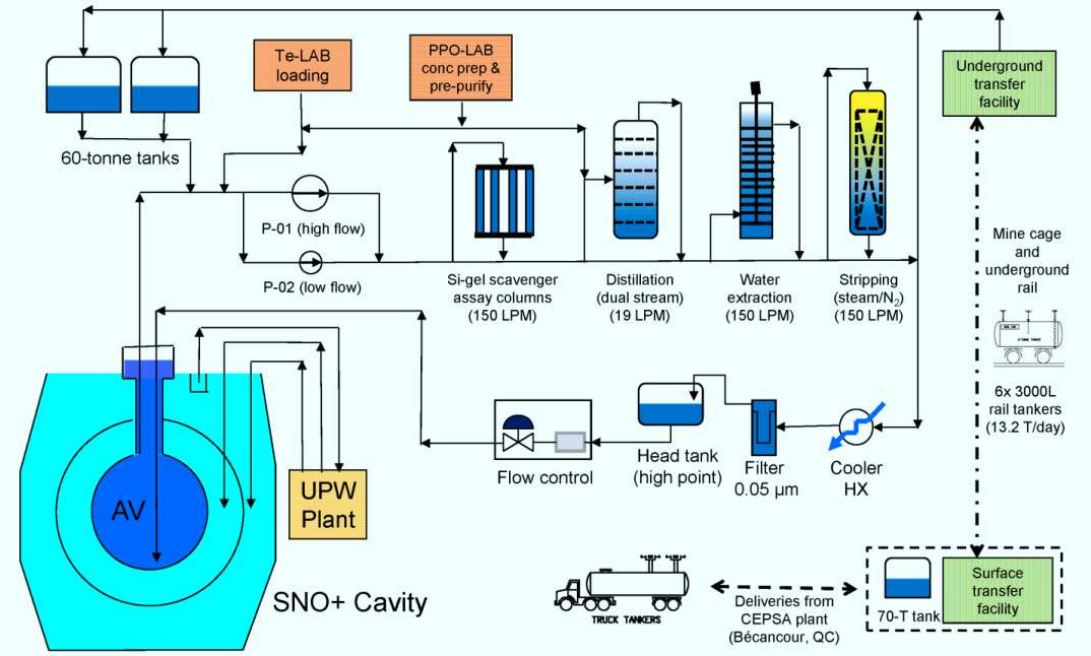

Figure 6.1: Process flow diagram of the main process components of the LAB distillation plant.

as little as 10 weeks [142]. Figure 6.1 shows a simplified process flow diagram for LAB deliveries.

6.1.2 Automation – Delta V

As a means to run in a consistent manner, all of the control systems are automated using an industry standard software, DeltaV [143], programmed by myself and Steven Back[1]. The program consists of a main overview screen which gives an operator an idea of the operation the plant is currently undergoing, this is shown in figure 6.2. Each component display of the plant is further broken into its own page where it can be individually selected, monitored, and controlled. All of the valves, pumps, and heaters required to process LAB are controlled electronically to allow for remote operation of the distillation plant. The software monitors input parameters from level sensors, temperature sensors, and flow meters to control distillation rates and flow rates through the plant through PID [2] controllers. Software interlocks are in place to make certain that the system does not

[1]SNOLAB Process Engineer in Training (EIT)

[2]A proportional-integral-derivative (PID) controller stably controls a device (such as a valve) to steadily change the readout of a process variable (such as a flow rate) until it reaches and is maintained

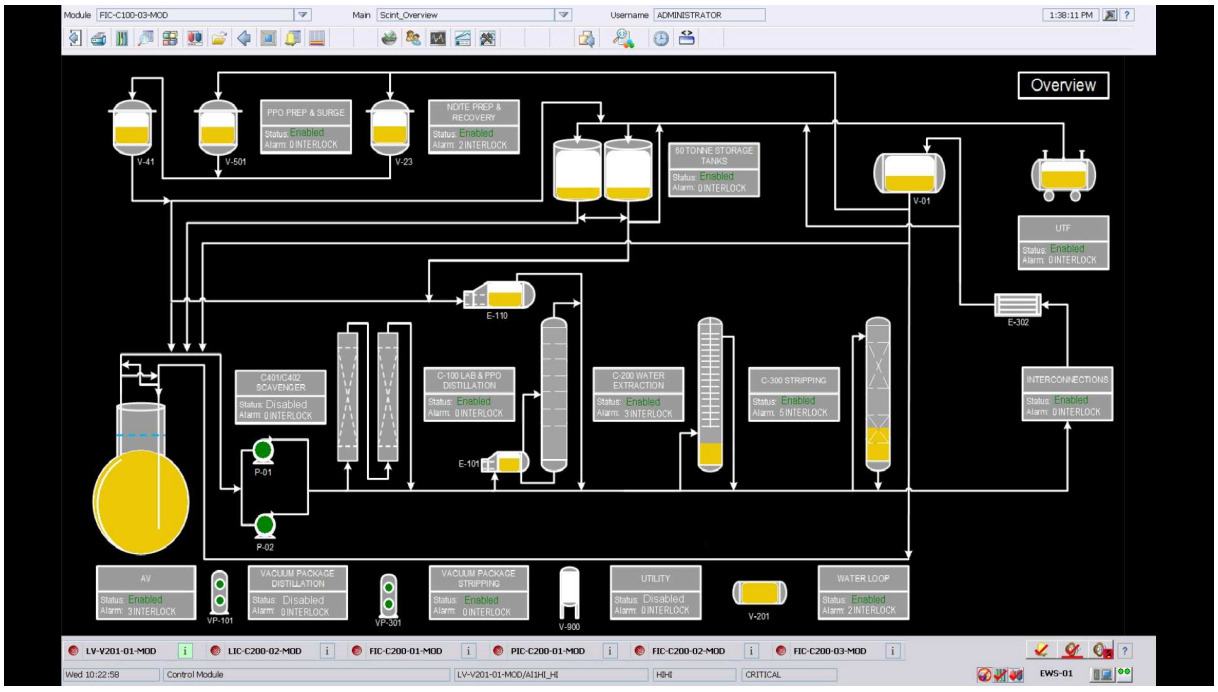

Figure 6.2: Sample of the Delta-V control screen showing the overview page of the entire scintillator distillation plant.

overpressurize, overheat, or overflow. To prepare for LAB distillation the entire system was commissioned with water to test the operation of all mechanical and electrical systems. LAB commissioning is ongoing with an expected completion date of fall 2018.

at some set point.

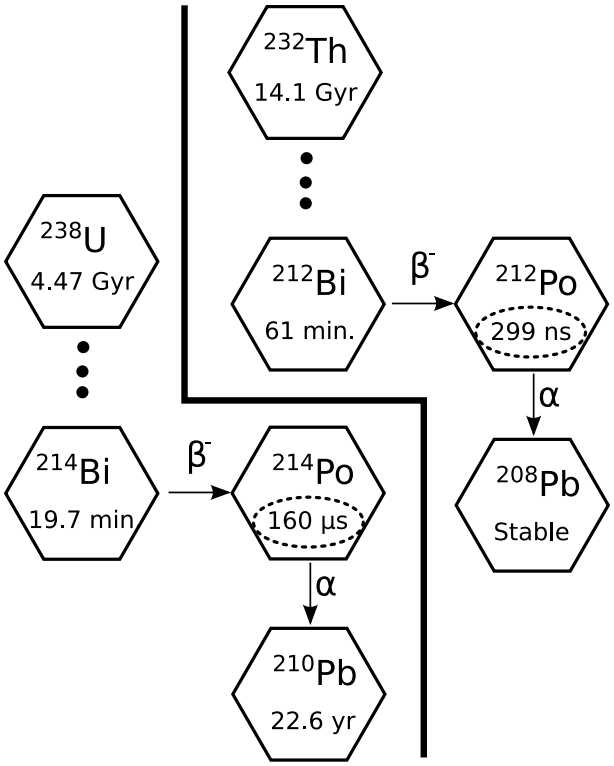

Figure 6.3: Simplified schematic of the Uranium and Thorium decay chains showing only the Bismuth Polonium decays relevant to Scout.

6.2 Scout – Quality Assurance

Scout[3] is an α/β coincidence counter designed to assess the radiopurity of the SNO+ liquid scintillator that arrives at the surface transfer facility at SNOLAB. Scout operates on the same principals as the actual SNO+ detector and is designed in a similar fashion. By filling with a mixture of LAB mixed with PPO at 2 g/L, Scout counts the decays of ^{214}Bi $\rightarrow$ ^{214}Po $\rightarrow$ ^{210}Pb in the Uranium decay chain and ^{212}Bi $\rightarrow$ ^{212}Po $\rightarrow$ ^{208}Pb in the Thorium decay chain, to determine the radiopurity in the delivered sample. Due to its size and acquisition time, Scout cannot detect purity levels required for the actual SNO+ detector, but rather will look for abnormalities in the delivered product—prior to delivery underground and distillation. The acquisition time will be 24-hours, which corresponds with the delivery schedule of LAB onsite by CEPSA. In the case of a discovered—higher than normal—contamination extra care can be taken when purifying the particular batch,

[3]Scout stands for **S**cintillator **C**ounter **o**f **U**ranium and **T**horium

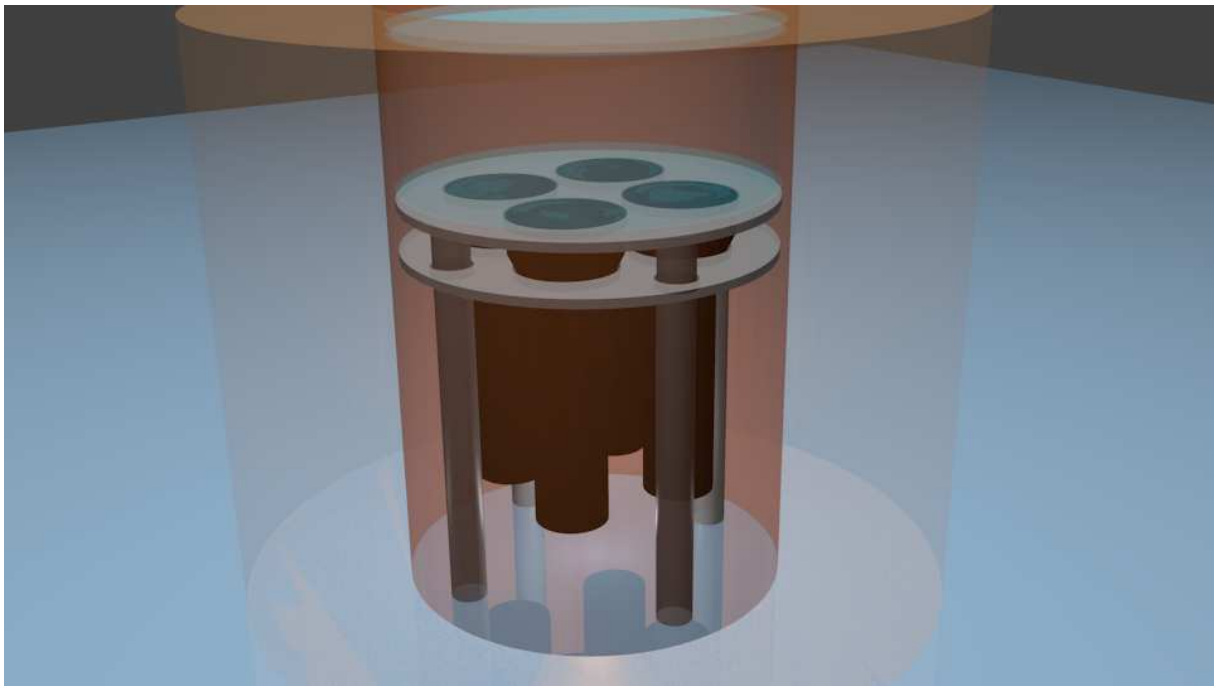

Figure 6.4: Blender rendering of Scout inside of its lead shield with four photomultipliers attached.

and in the case of serious contamination, take steps to discover the source and prevent further poor quality LAB.

6.2.1 Design

The Scout detector consists of an acrylic vessel which holds a 3 liter sample of LAB mixed with 2g/L PPO. The acrylic vessel itself is cylindrical in shape, measuring 9.75 inches inside diameter, and 5.75 inches tall. The acrylic is painted with titanium white acrylic paint which provides some reflectivity in order to increase the effective photo-coverage. The assembly is placed within a copper-plated lead shield to protect from background radiation and radioactivity. The lead provides a barrier between the detector and external radiation, while the copper further reduces radiation originating from the lead itself (such as the decay of ^{210}Pb). The shape and design of Scout was based upon a pre-existing lead shield from a Germanium counter and is shown in figure 6.4. The interior volume of the lead shield, and the size of the photomultiplier tubes used are the primary restriction on the total volume. The acrylic vessel was constructed by the machine shop staff at Davis [144] and shipped to SNOLAB for assembly with the principle design shown in figure 6.5.

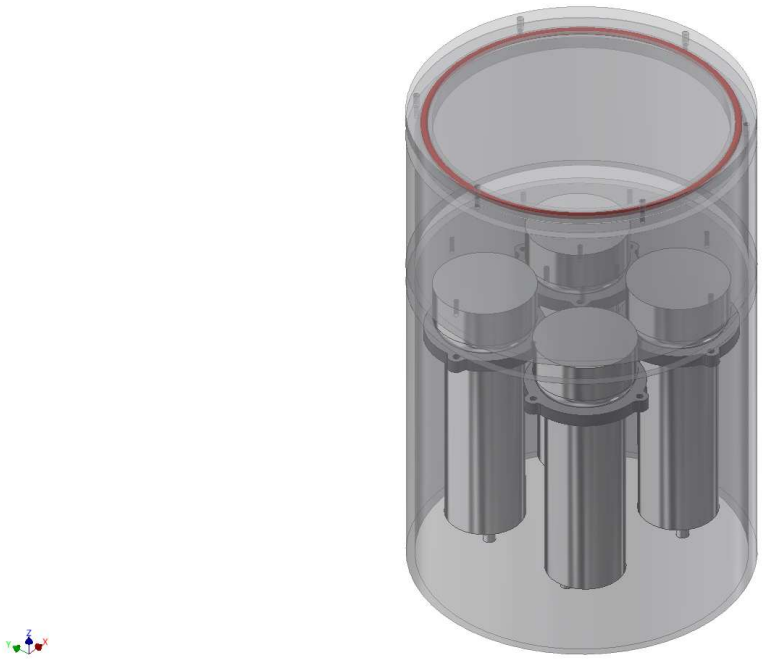

Figure 6.5: CAD drawing of the Scout detector with the PMT support rings shown compressing the PMTs into the bottom of the acrylic vessel.

The constructed inner vessel—prior to painting and installation—is shown in figure 6.6.

Four ADIT 3-inch photomultipliers are held in place on the bottom of the detector by acrylic support rings with self-tensioning screws to provide uniform pressure. Between the acrylic vessel and the photocathode is a compressible optical gel pad made by flashpoint crystals designed to optically couple the photocathode and the vessel [4]. Each of the four PMTs (figure 6.7) is powered independently by a CAEN DT5533P high-voltage power supply with channel by channel high-voltage settings. The ideal operating voltage is between 1000 and 1500 volts with a 60 $M\Omega$ base resistance. Each of the PMT bases has a separate pickoff for the signal which is transmitted via a BNC-LIMO cable to the Struck SIS3316 waveform digitizer. The data from the waveform digitizer is then uploaded to the DAQ computer via ethernet where it is read in through custom software designed to control and monitor Scout. The full data acquisition electronics and power supply are shown in figure 6.8.

[4]The optical gel pads were used to test the use of a reusable, mess free optical coupling technique. These would not be recommended for future use due to poor coupling as compared with optical grease.

Figure 6.6: Scout inner vessel and stand, constructed in the UC Davis machine shop.

Figure 6.7: ADIT 3-inch photomultiplier tube with connected base. Top shows the PMT dynodes through the glass, and bottom is the PMT wrapped in electrical tape to prevent light from entering and exiting the sides.

Figure 6.8: Scout data acquisition system with 4 channels with independent high voltage settings (red box) and a VME powered 16 channel waveform digitizer.

6.2.2 Data Acquisition (DAQ)

The data acquisition hardware consists of Struck SIS3316 waveform digitizer which is set to operate from 0 to -2V at 14-bits with a 250 MHz onboard clock. The board can be configured to write asynchronously from its 16 channels and can be setup to run in any trigger configuration including an external trigger. The digitizer is connected to an Intel NUC (the DAQ computer) via an ethernet cable to transmit recorded data buffers and receive commands. Custom software was written in a combination of C++ and Python to operate the digitizer and set the Scout settings for various run types (physics, calibration, and laser). Each channel has separate threshold settings and trigger delays to correct for cable length—in practice cables of equal length are used so no correction is required. Full waveforms are collected for every channel in every event out to 2048 ns (512 bytes) in order to do post-processing to remove spurious events. Figure 6.8 shows the DAQ setup with the waveform digitizer setup inside a Vector 4-slot VME crate with the CAEN high voltage supply sitting directly on top. The channels are spaced apart in order to minimize potential cross-talk between adjacent channels. Due to the asynchronous buffers on the digitizer, the DAQ computer must sort and build events based on individual channel timestamps prior to analysis.

Figure 6.9: Interior of Scout filled with LAB.

6.2.3 Filling Procedure

The purpose of Scout is to run for short periods of time (24 hours) on many batches of LAB as they are delivered to SNO+. During scintillator deliveries, all LAB must remain under nitrogen cover gas to avoid extra radon contamination. To accomplish this, a 10 liter polyethylene transfer vessel is purged with nitrogen gas from a liquid nitrogen boil-off system and then filled through a connection to a sample port on the surface transfer facility manifold. Prior to filling, PPO is measured out and placed within the transfer vessel such that the final product will have an approximate 2 g/liter ratio of PPO to LAB. This measurement will vary with each sample, so a γ source should be used to briefly calibrate Scout on each transfer. Figure 6.9 shows the acrylic vessel filled with a sample of LAB. In this picture the lid was removed to purposefully expose the LAB to radon in order to take a test measurement. Shown in figure 6.10 is the detector with the lid on showing the transfer ports to fill Scout from the transfer vessel. There is no plan to reuse the LAB once the Scout measurement is complete, so the lid is removed when emptying scout so that a hand pump can be used to siphon out the LAB into a waste drum.

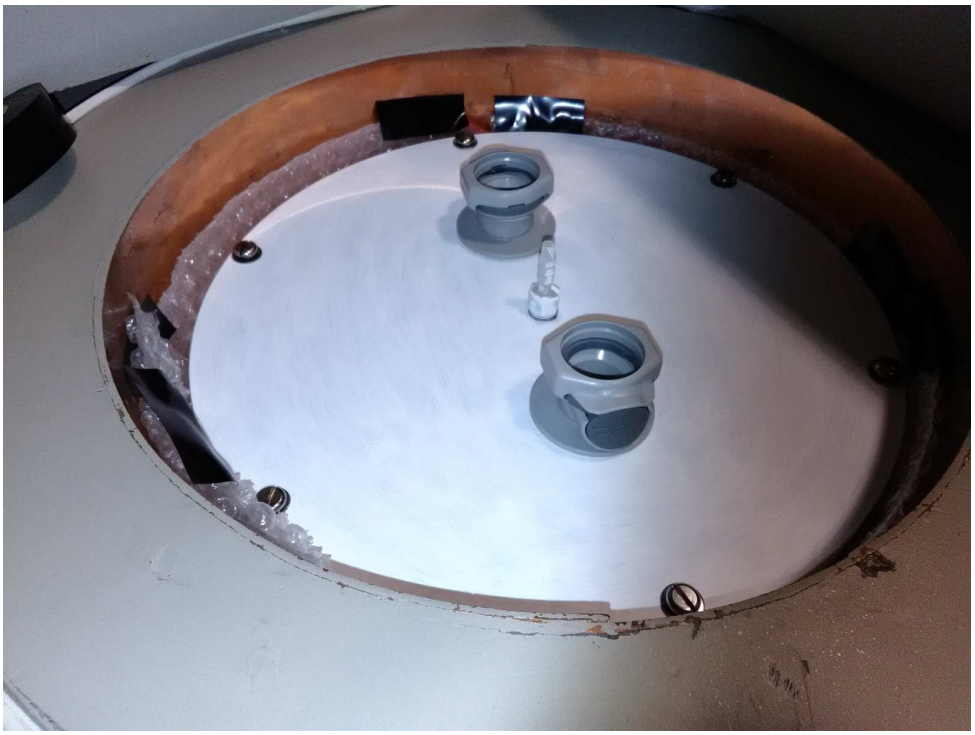

Figure 6.10: Scout viewed from the top showing the nitrogen purge connection and the fill connection (the two are interchangeable).

6.2.4 Calibration

A few methods of calibration are used for Scout in order to estimate the detection efficiency and energy scale. A laser diode is used to provide a single photo-electron triggered pulse to the photomultipliers, and both γ check sources and spiked samples are used to estimate the energy scale and coincidence timing. Due to the relatively high muon rate ($\sim$ 8 Hz), muon background runs are also used to assess the energy scale and expected backgrounds for Scout.

6.2.4.1 Laser Diode

During the first phase of commissioning, calibration runs were taken on Scout to test the uniformity of the PMTs as well as the response of the detector. An Arduino DUE microcontroller with an onboard 84 MHz clock was programmed to take advantage of the onboard master clock as an LED driver. A pulse-width modulated signal at twice the master clock frequency can be extracted without jitter which results in an exact pulse width of 24 ns, which is tunable in steps of 24 ns to provide wider pulse widths if

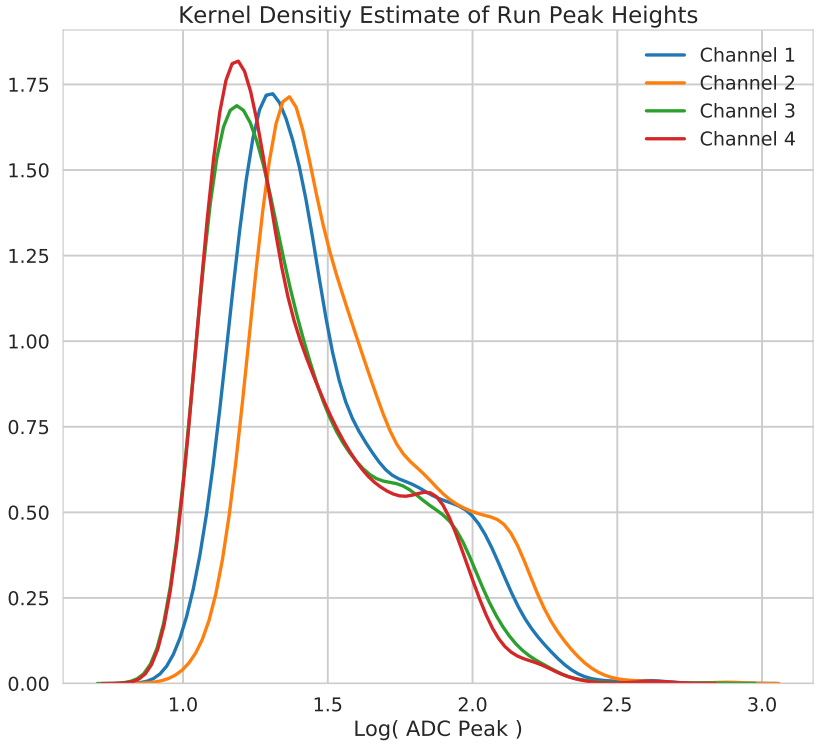

Figure 6.11: Kernel density estimate of peak heights for the four Scout channels over a single background run where the events are expected to be isotropic and homogeneous.

needed. Channel 1 on the Arduino sends a pulse to a laser diode through an adjustable resistor to moderate the voltage (and thus emitted photon count), while channel 13 sends a synchronized trigger pulse to the waveform digitizer. When running in this mode, the waveform digitizer is set to trigger only on the external trigger sent to it by the Arduino. Results from the laser diode pulser are compared to run average peak heights to estimate the relative gain of each PMT. Shown in figure 6.11 are the kernel density estimates of the peak heights over a single background run, where events are expected to be isotropic and homogeneous. The differences in the peak height distributions are used to correct for the differences in gain when calculating the total charge of an event.

6.2.4.2 Thoron

In order to estimate the potential sensitivity in using the coincidence rate of ^{212}Po a Thoron source was used to spike a sample of LAB. Thoron is the name for radon produced

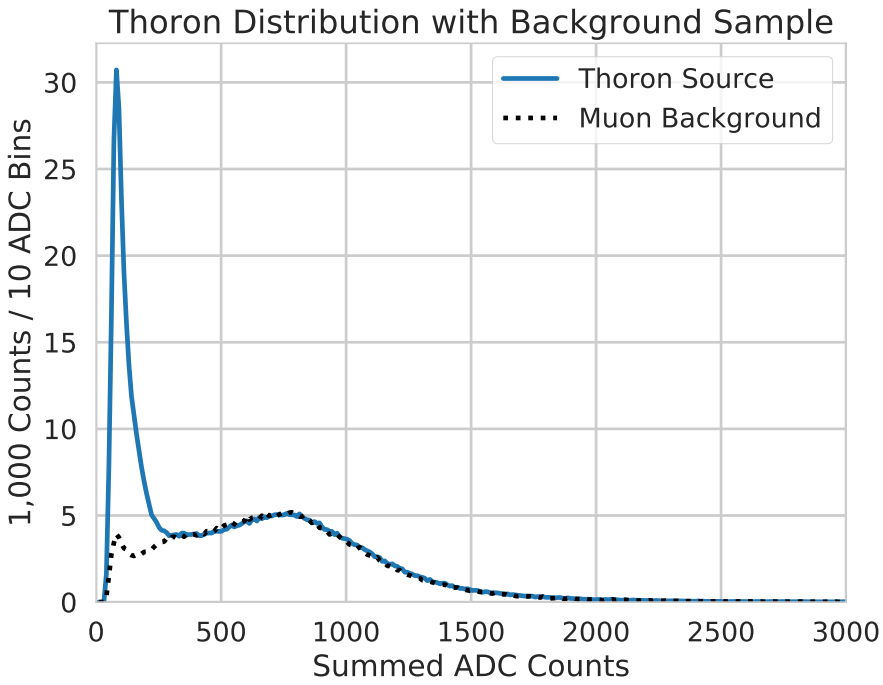

Figure 6.12: Distribution of Thoron events with a background run overlayed showing the relative muon contribution normalized by run time to match. From this comparison a cut at 300 ADC can be made to remove a large fraction of background events from a data set with a negligible impact on the Thoron signal.

in the thorium series decay chain, specifically ^{220}Rn. The source container holds ^{228}Th which decays to ^{224}Ra and finally to ^{220}Rn which is gaseous. Nitrogen gas flows through the source chamber collecting the ^{220}Rn and is then subsequently bubbled through a sample of LAB for 24 hours. This small sample of LAB was then added to a ∼3 liter sample of LAB in Scout. The Thoron spike was used to measure the energy scale and efficiency for tagging the α from the decay of ^{212}Po. Since the half-life of ^{212}Po is relatively short (299 ns), the coincidence signal falls within the same trigger window and is competing with noise from the primary trigger. These particular photomultipliers tend to have a high amount of ringing from the base which has a similar frequency to the pulse, making it very difficult to distinguish secondary pulses from the ringing. Figure 6.13 shows ringing after a large pulse in the PMT. This ringing is suppressed using a moving average window set to the width of these pulses to average out the ringing, but reducing the peak height. This does a good job at removing re-triggers from the data as well as suppress oscillations produced

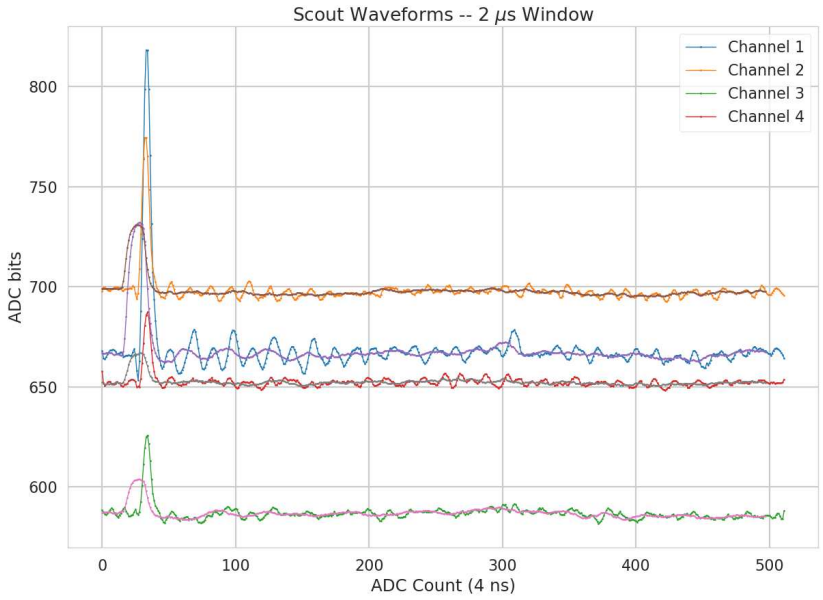

Figure 6.13: Scout waveforms for a random event during a background run. Ringing can be seen after the initial pulse with a smoothing function applied to reduce this ringing. The smoothing function is moving-average convolution with a width of 60 ns(approximate ringing period), which substantially reduces the ringing at the sacrifice of peak height resolution.

by the primary pulse—allowing the waveform to be analyzed to search for secondary pulses within a single trigger window. In practice the efficiency to find another peak in an event is very low due to the high level of noise in the channel after an event. To look for coincidence events, after applying a filter for the ringing, the time between the primary and secondary pulse is shown in figure 6.14. To suppress the effects of muons, a cut was made on the total ADC counts across all channels on the primary events at 250 ADC, which selects for primarily Thoron events as shown in figure 6.12. A prominent bump appears in the Thoron data at 60 ns after the primary trigger ; however, the bump does not have the characteristic exponential falloff expected from a Poissonian coincidence signal. At a maximum this provides a 4.9% tagging efficiency for this particular coincidence channel, suggesting that simply counting events within a background subtracted energy window would provide a more suitable measurement. When looking for single events in energy, ^{212}Bi has a branching ratio of 35.94% to α decay to ^{208}Tl. ^{208}Tl has a half-life of 3.053

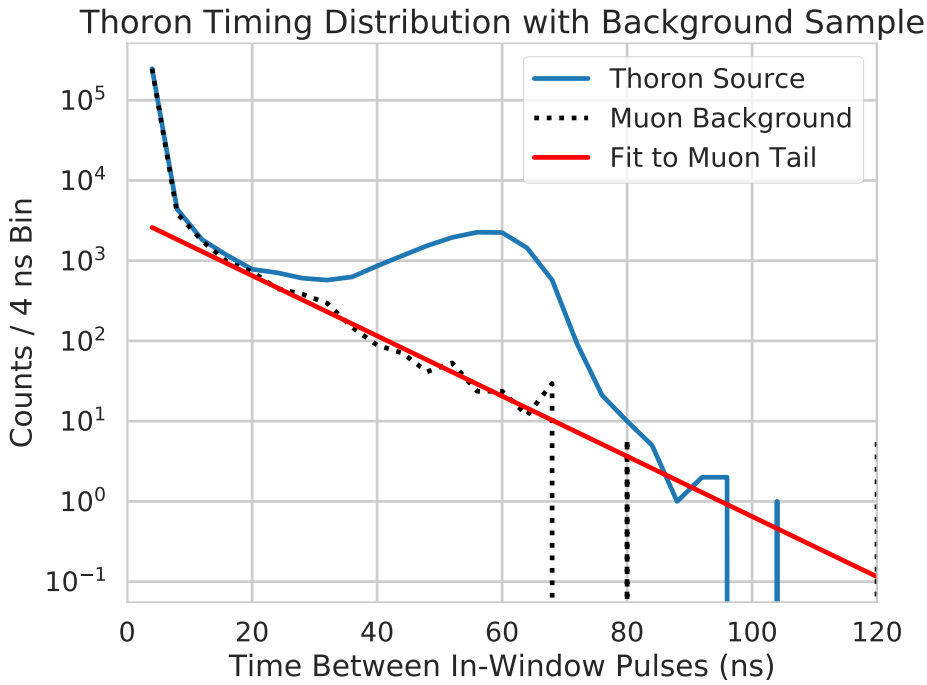

Figure 6.14: Timing between coincidence pulses within a single event window with an energy cut to remove high energy muons. An excess is seen in the Thoron data at 60 ns above the scaled background run, showing signs of tagging the ^{212}Po α with an efficiency of 4.90 $\pm$ 0.044%.

minutes with a β^- decay endpoint of 4.999 MeV, which provides a very strong energy signal to look for.

6.2.5 Sensitivity

The analysis is split into two regions corresponding to the Uranium series and Thorium series candidates. The Uranium series produces coincidence events with a characteristic lifetime of 230.8 μs [5] which is well outside the range of retriggers and correlated noise. Based on the results shown in figure 6.15, a cut at $\Delta t > 10$ μs will eliminate most of the retriggers and a requirement of $\Delta t < 300$ μs will eliminate a majority of the accidental coincidences. The upper bound was chosen to optimize the sensitivity given the random coincidence rate and loss of signal efficiency as shown in figure 6.16. Due to the PMT noise, coincidence signals from ^{212}Bi / ^{212}Po are unlikely to be observed without changes

[5] 160 μs / Ln(2)

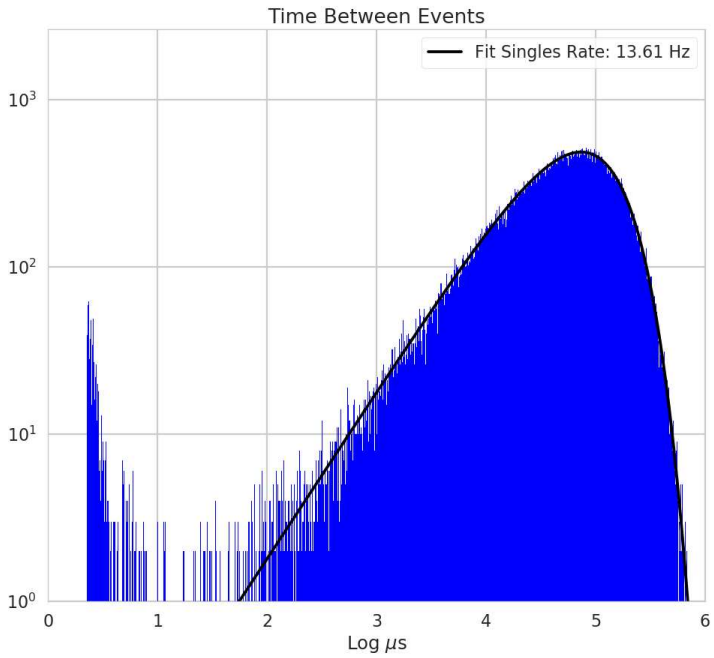

Figure 6.15: Scout inter-event timing spectrum on a log-log scale for a background run showing two distributions corresponding to retriggers which occur up to 10 μs after the primary trigger and single events (dominated by muons). The single event rate is fit with an exponential distribution.

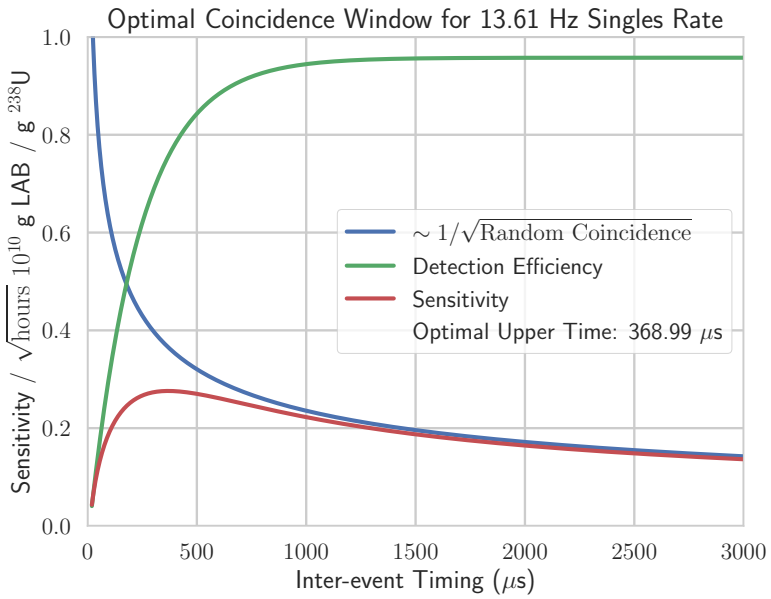

Figure 6.16: Plot of the relative detection sensitivity for ^{214}Bi - ^{214}Po coincidence signals used to optimize the upper bound on the coincidence window.

to the hardware which targets the PMT ringing. The branching ratio of ^{212}Bi to ^{208}Tl is 35.94% and would provide a strong single event rate in the case where the spectrum is well calibrated and can be resolved. As discussed in the next section, reducing the muon rate would greatly improve Scout's ability to set limits on the ^{232}Th contamination. Thus, consideration is currently being given to moving Scout underground.

6.2.5.1 Future Improvements

Based on the preliminary Scout results, there are a number of improvements which can be made in order to increase the sensitivity of the detector. Due to the high noise in the waveforms, detecting single ^{208}Tl decays will yield a strong result for the Thorium content of the LAB sample. This signal does not have a coincidence tag so to have a reasonable sensitivity the number of muons going through the detector must be reduced. One way to accomplish this would be to mount plastic scintillator paddles to the top of the detector in order to veto muons going through the detector. A better way would be to simply take the detector from the surface transfer facility underground to SNOLAB. The muon rate at such a depth through a small detector like Scout would reduce from $\sim$ 8 Hz to a few per century ($\sim 10^{-9}$ Hz). With no muons going through the detector, Scout would become very sensitive to any radiation coming from the liquid scintillator as well as detector components. The sensitivity as a function of single event rate is shown in figure 6.17 where the added depth would improve the sensitivity to ^{238}U by a factor of 6.

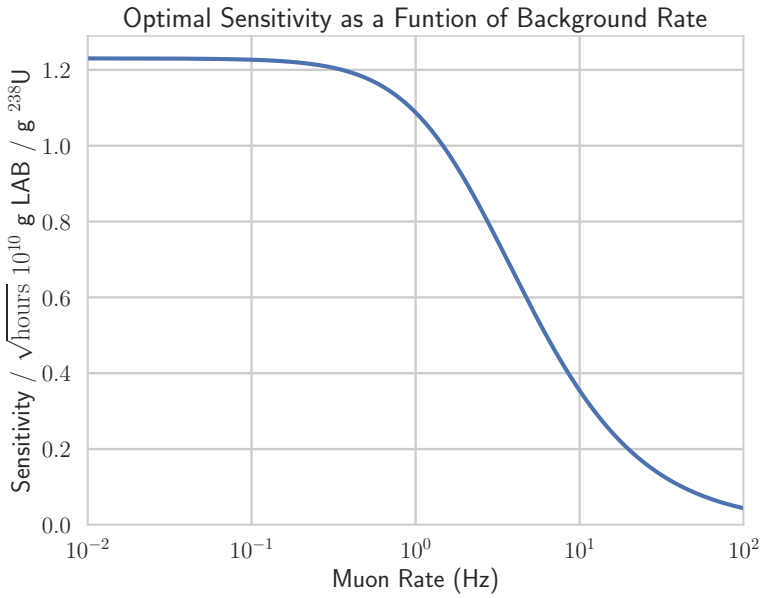

Figure 6.17: Plot of the change in sensitivity as a function of muon rate through the detector. The sensitivity approach the background free model around 0.1 Hz (and would be well below this limit at the depth of SNOLAB where the muon rate would be 10^{-9} Hz.

Chapter 7

Conclusions

The search for physics beyond the Standard Model encompasses a broad spectrum of physics topics and experiments. The decay of nucleons through non-standard modes would provide evidence that such physics exists and would also constrain theoretical models through the branching ratio of the various decay modes. This dissertation presents results on the search for neutron decay through invisible modes, motivated by extradimensional models which predict $n \rightarrow 3\nu$. The limits set here are based on the unblinded data set with the full data set to be published shortly after. This data set contains 11.068 days of live time and represents a period in time with particularly high external backgrounds. Based on this initial data set, a partial lifetime for the neutron through invisible modes is determined to be 1.05×10^{29} years at 90% C.L. The result takes into account the loss of data due to cuts used to remove instrumental backgrounds, as well as the estimated contamination of instrumental backgrounds. Systematic errors on the expected backgrounds are handled through the use of a profile likelihood ratio which broadens the likelihood distribution, while systematic errors on the event reconstruction are accounted for through smearing of the probability density functions used for the backgrounds and signal based on data taken using the ^{16}N calibration source. From the initial measurements, data cleaning is expected to sacrifice 1.2% of signal and physics background events (taken as an adjustment to the live time), while allowing a potential 0.037 events into the signal region at 90% C.L. The final result was found using the upper 90% confidence interval of the profile likelihood ratio found by fitting Monte Carlo predicted probability

density functions in reconstructed energy and the cube of the reconstructed position to the data. No excess of events above the expected background was observed.

The future of SNO+ is to eventually fill with liquid scintillator and then dope the scintillator with ^{130}Te to search for neutrinoless double beta decay. To achieve the sensitivity required to make a world leading result, SNO+ is required to distill the liquid scintillator underground to minimize the likelihood of contamination. The scintillator distillation plant, which is currently underground and being commissioned, will run on shipments LAB as it arrives to the detector over the course of 3-6 months, operating at a nearly continuous rate. Scout will be in place underground to assess the final product of the distillation plant prior to filling the detector to look for any possible contamination.

Appendix A

Example Instrumentals

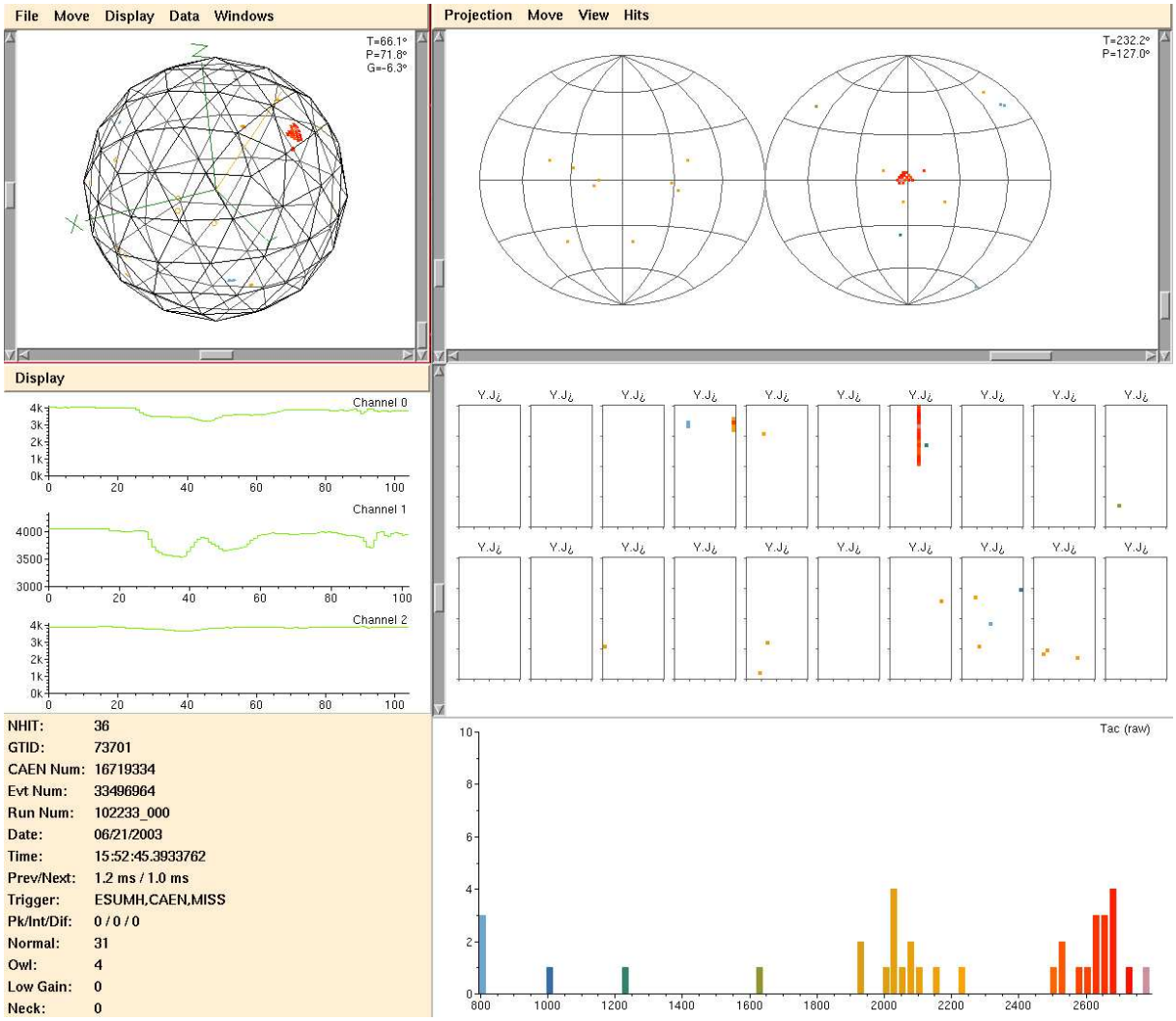

Figure A.1: Flasher found using the flashergeocut

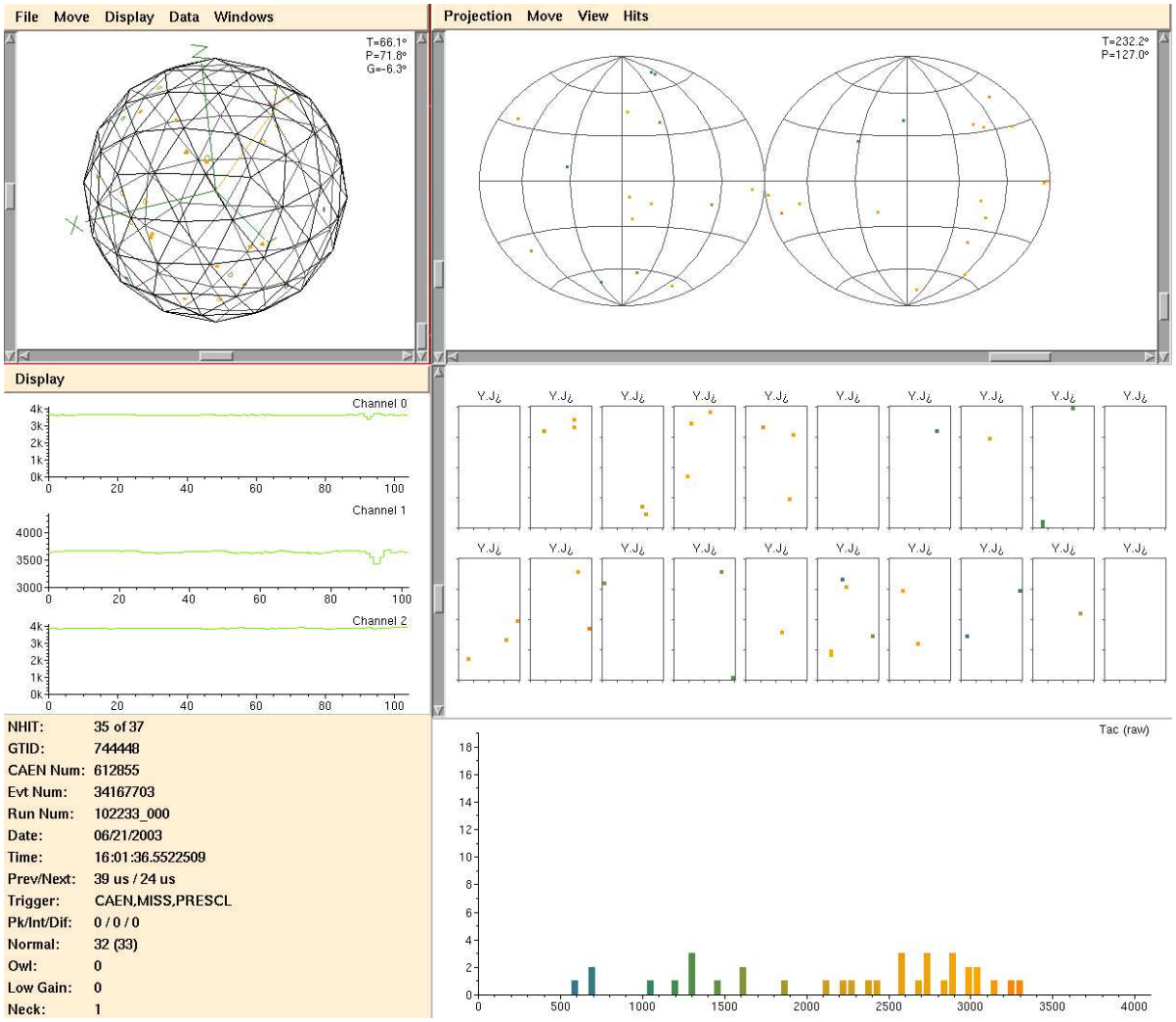

Figure A.2: Small flat-tac (low nhit)

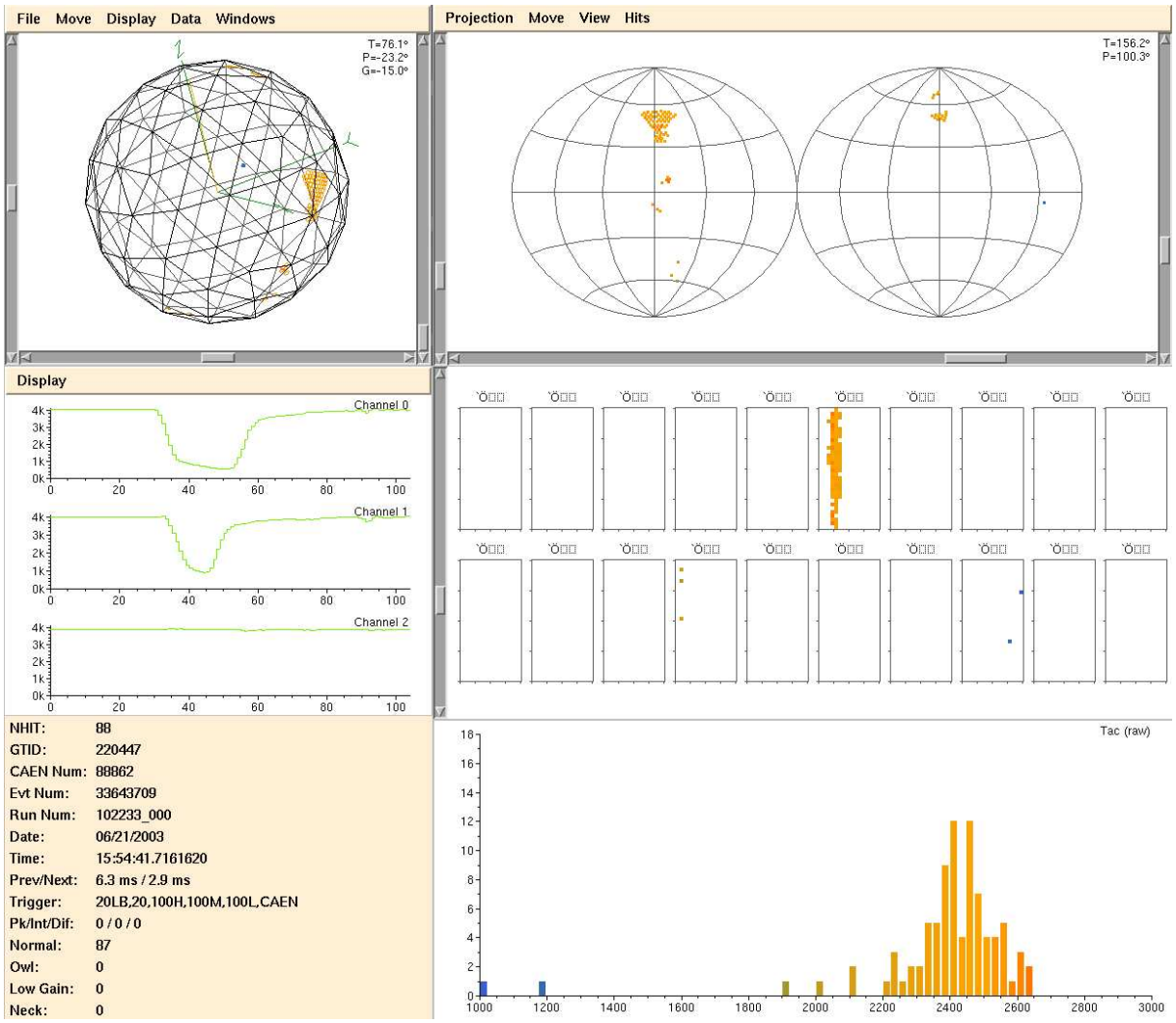

Figure A.3: Sharkfin event with a characteristic fin shape in Channel 2 of the CAEN digitized waveform.

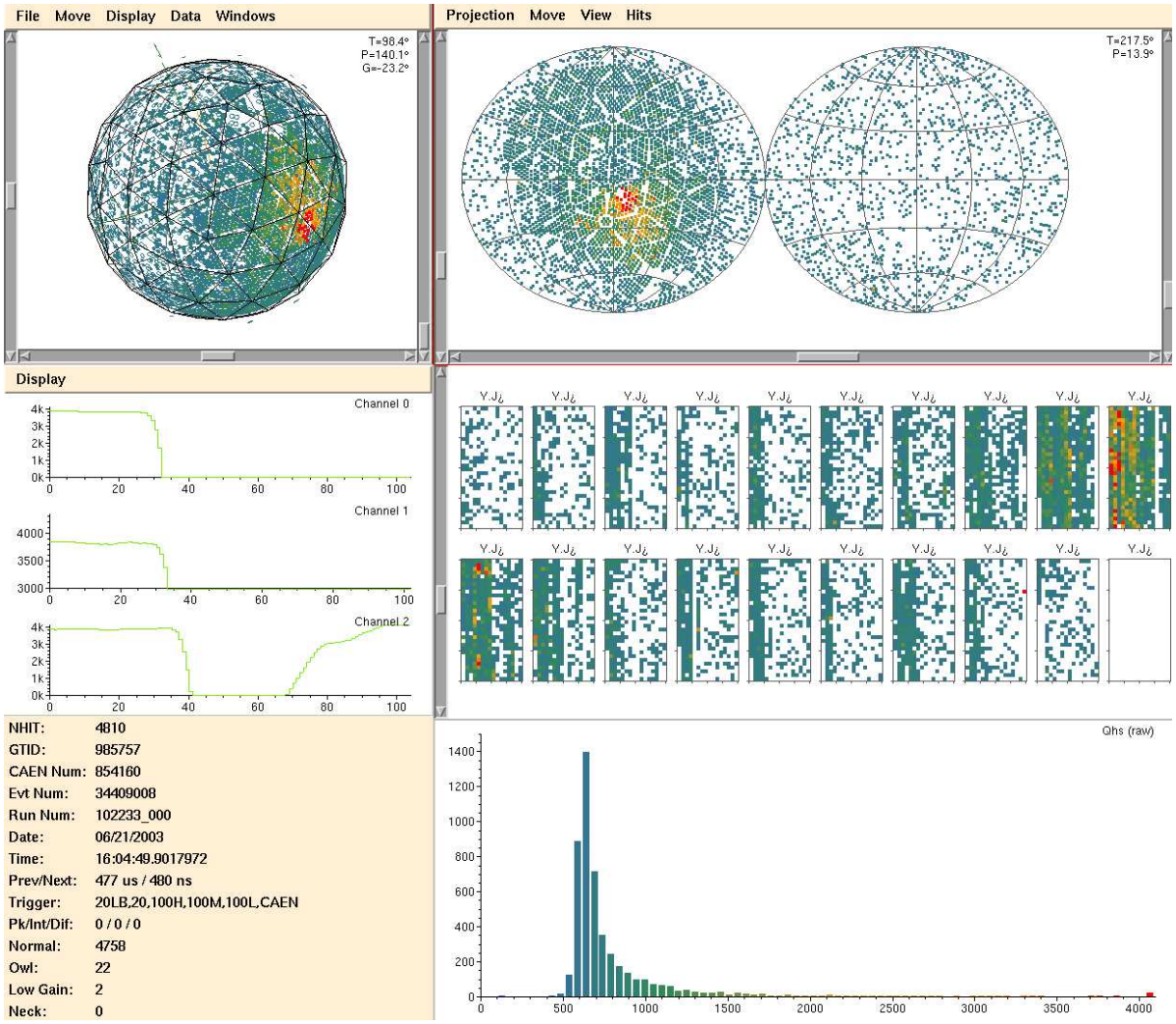

Figure A.4: Muon passing through the detector. Notice the hit OWL PMTs showing light on the outside of the PMT support structure.

References

[1] C. Burgard. 2016. http://www.texample.net/tikz/examples/model-physics/.

[2] K. Abe et al. Letter of Intent: The Hyper-Kamiokande Experiment — Detector Design and Physics Potential —. 2011.

[3] D. D'Angelo. Low Energy Neutrino Measurements. *Pramana*, 79:757–780, 2012.

[4] Th. A. Mueller et al. Improved Predictions of Reactor Antineutrino Spectra. *Phys. Rev.*, C83:054615, 2011.

[5] P. F. de Salas, D. V. Forero, C. A. Ternes, M. Tortola, and J. W. F. Valle. Status of neutrino oscillations 2017. 2017.

[6] E. Andreotti et al. Double-beta decay of ^{130}Te to the first 0^+ excited state of ^{130}Xe with CUORICINO. *Phys. Rev.*, C85:045503, 2012.

[7] B. Singh. Nuclear data sheets for a = 130. *Nuclear Data Sheets*, 93(1):33 – 242, 2001.

[8] S. Dell'Oro, S. Marcocci, M. Viel, and F. Vissani. Neutrinoless double beta decay: 2015 review. *Adv. High Energy Phys.*, 2016:2162659, 2016.

[9] S. Dell'Oro, S. Marcocci, and F. Vissani. New expectations and uncertainties on neutrinoless double beta decay. *Phys. Rev. D*, 90:033005, Aug 2014.

[10] J. Barea, J. Kotila, and F. Iachello. $0\nu\beta\beta$. *Phys. Rev. C*, 91:034304, Mar 2015.

[11] F. Šimkovic, V. Rodin, A. Faessler, and P. Vogel. $0\nu\beta\beta$. *Phys. Rev. C*, 87:045501, Apr 2013.

[12] J. Menéndez, A. Poves, E. Caurier, and F. Nowacki. Disassembling the nuclear matrix elements of the neutrinoless decay. *Nuclear Physics A*, 818(3):139 – 151, 2009.

[13] T. Akiri et al. The 2010 Interim Report of the Long-Baseline Neutrino Experiment Collaboration Physics Working Groups. 2011.

[14] J.D. Jackson. *Classical Electrodynamics*. 1999.

[15] J.B. Birks. *The Theory and Practice of Scintillation Counting*. International series of monographs on electronics and instrumentation. Pergamon Press, 1964.

[16] K. Singh. Detector picture. SNO+ DocDB 4331v1.

[17] SNO/SNO+ Electronics Experts. Sno+ detector operator manual. https://github.com/snoplus/operator-manual.

[18] N. Barros. *Precision Measurement of Neutrino Oscillation Parameters: Combined Three-phase Results of the Sudbury Neutrino Observatory*. PhD thesis, Universidade de Lisboa, 2011.

[19] J. Boger et al. The sudbury neutrino observatory. *Nuclear Instruments and Methods in Physics Research Section A: Accelerators, Spectrometers, Detectors and Associated Equipment*, 449(1):172 – 207, 2000.

[20] M. R. Dragowsky et al. The N-16 calibration source for the Sudbury Neutrino Observatory. *Nucl. Instrum. Meth.*, A481:284–296, 2002.

[21] M. C. Gonzalez-Garcia, Michele Maltoni, and Thomas Schwetz. Global Analyses of Neutrino Oscillation Experiments. *Nucl. Phys.*, B908:199–217, 2016.

[22] R. Saakyan. Two-neutrino double-beta decay. *Annual Review of Nuclear and Particle Science*, 63(1):503–529, 2013.

[23] H. Ejiri. Nuclear deexcitations of nucleon holes associated with nucleon decays in nuclei. *Phys. Rev. C*, 48:1442–1444, Sep 1993.

[24] H. M. O'Keeffe, E. O'Sullivan, and M. C. Chen. Scintillation decay time and pulse shape discrimination in oxygenated and deoxygenated solutions of linear alkylbenzene for the SNO+ experiment. *Nucl. Instrum. Meth.*, A640:119–122, 2011.

[25] S. Asahi. Reactor baseline calculations. SNO+ DocDB 2460v2.

[26] V. Lozza. Expected radioactive backgrounds in sno+. SNO+ DocDB 507v35.

[27] V. Lozza. Physics list for nd analysis. SNO+ DocDB 4820v7.

[28] B. Gripaios. Lectures on Physics Beyond the Standard Model. 2015.

[29] J. R. Ellis. Limits of the standard model. In *PSI Zuoz Summer School on Exploring the Limits of the Standard Model Zuoz, Engadin, Switzerland, August 18-24, 2002*, 2002.

[30] C. Patrignani et al. Review of Particle Physics. *Chin. Phys.*, C40(10):100001, 2016.

[31] A. Zee. *Quantum field theory in a nutshell*. 2003.

[32] C. Giunti and C. W. Kim. *Fundamentals of Neutrino Physics and Astrophysics*. 2007.

[33] M. Herrero. The Standard model. *NATO Sci. Ser. C*, 534:1–59, 1999.

[34] S. L. Glashow. Partial Symmetries of Weak Interactions. *Nucl. Phys.*, 22:579–588, 1961.

[35] S. Weinberg. A Model of Leptons. *Phys. Rev. Lett.*, 19:1264–1266, 1967.

[36] A. Salam and J.C. Ward. Electromagnetic and weak interactions. *Physics Letters*, 13(2):168 – 171, 1964.

[37] F. Englert and R. Brout. Broken Symmetry and the Mass of Gauge Vector Mesons. *Phys. Rev. Lett.*, 13:321–323, 1964.

[38] P. W. Higgs. Broken Symmetries and the Masses of Gauge Bosons. *Phys. Rev. Lett.*, 13:508–509, 1964.

[39] G. S. Guralnik, C. R. Hagen, and T. W. B. Kibble. Global Conservation Laws and Massless Particles. *Phys. Rev. Lett.*, 13:585–587, 1964.

[40] C. Patrignani et al. Review of Particle Physics. *Chin. Phys.*, C40(10):100001, 2016.

[41] Y. Fukuda et al. Evidence for oscillation of atmospheric neutrinos. *Phys. Rev. Lett.*, 81:1562–1567, Aug 1998.

[42] Q. R. et al. Ahmad. Measurement of the rate of $\nu_e + d \rightarrow p + p + e^-$ interactions produced by ^8b solar neutrinos at the sudbury neutrino observatory. *Phys. Rev. Lett.*, 87:071301, Jul 2001.

[43] M. E. Peskin and D. V. Schroeder. *An Introduction to quantum field theory*. Addison-Wesley, Reading, USA, 1995.

[44] E. Majorana. A symmetric theory of electrons and positrons. *Nuovo Cim.*, 14:171–184, 1937.

[45] P. Minkowski. $\rightarrow$e at a rate of one out of 109 muon decays? *Physics Letters B*, 67(4):421 – 428, 1977.

[46] Rabindra N. Mohapatra and Goran Senjanović. Neutrino mass and spontaneous parity nonconservation. *Phys. Rev. Lett.*, 44:912–915, Apr 1980.

[47] R. Adam et al. Planck 2015 results. I. Overview of products and scientific results. *Astron. Astrophys.*, 594:A1, 2016.

[48] J. Lesgourgues and S. Pastor. Neutrino cosmology and planck. *New Journal of Physics*, 16(6):065002, 2014.

[49] B. Pontecorvo. Inverse beta processes and nonconservation of lepton charge. *Zhurnal Éksperimental'noĭ i Teoreticheskoĭ Fiziki*, 34:247, 1957.

[50] Z. Maki, M. Nakagawa, and S. Sakata. Remarks on the unified model of elementary particles. *Progress of Theoretical Physics*, 28(5):870–880, 1962.

[51] V. Barger, D. Marfatia, and K. Whisnant. *The Physics of Neutrinos*. Princeton University Press, 2012.

[52] G. A. McGregor. First results from the Sudbury Neutrino Observatory. In *Proceedings, 37th Rencontres de Moriond on Electroweak Interactions and Unified Theories: Les Arcs, France, March 9-16, 2002*, pages 249–256, 2002.

[53] K. Abe et al. Solar Neutrino Measurements in Super-Kamiokande-IV. *Phys. Rev.*, D94(5):052010, 2016.

[54] Q. R. Ahmad et al. Direct evidence for neutrino flavor transformation from neutral-current interactions in the sudbury neutrino observatory. *Phys. Rev. Lett.*, 89:011301, Jun 2002.

[55] W. C. Haxton, R. G. Hamish Robertson, and Aldo M. Serenelli. Solar Neutrinos: Status and Prospects. *Ann. Rev. Astron. Astrophys.*, 51:21–61, 2013.

[56] T. Kajita. Atmospheric neutrino results from Super-Kamiokande and Kamiokande: Evidence for neutrino(mu) oscillations. *Nucl. Phys. Proc. Suppl.*, 77:123–132, 1999.

[57] A. Suzuki and KamLand Collaboration. Results from kamland reactor neutrino detection. *Physica Scripta*, 2005(T121):33, 2005.

[58] F.P. An et al. Independent measurement of the neutrino mixing angle θ_{13} via neutron capture on hydrogen at daya bay. *Phys. Rev. D*, 90:071101, Oct 2014.

[59] T. Nakaya and R. K. Plunkett. Neutrino Oscillations with the MINOS, MINOS+, T2K, and NOvA Experiments. *New J. Phys.*, 18(1):015009, 2016.

[60] A. B. Sousa. First MINOS+ Data and New Results from MINOS. *AIP Conf. Proc.*, 1666:110004, 2015.

[61] P. Adamson et al. Constraints on Oscillation Parameters from ν_e Appearance and ν_μ Disappearance in NOvA. *Phys. Rev. Lett.*, 118(23):231801, 2017.

[62] E. Kemp. The Deep Underground Neutrino Experiment: The precision era of neutrino physics. *Astron. Nachr.*, 338(9-10):993–999, 2017.

[63] R. G. Hamish Robertson. KATRIN: an experiment to determine the neutrino mass from the beta decay of tritium. In *Proceedings, 2013 Community Summer Study on the Future of U.S. Particle Physics: Snowmass on the Mississippi (CSS2013): Minneapolis, MN, USA, July 29-August 6, 2013*, 2013.

[64] J. Chadwick. The intensity distribution in the magnetic spectrum of beta particles from radium (B + C). *Verh. Phys. Gesell.*, 16:383–391, 1914.

[65] W. Pauli. letter of the 4th of december 1930.

[66] S. R. Elliott and P. Vogel. Double beta decay. *Ann. Rev. Nucl. Part. Sci.*, 52:115–151, 2002.

[67] H. Primakoff and S. P. Rosen. Double beta decay. *Reports on Progress in Physics*, 22(1):121, 1959.

[68] W.C. Haxton and G.J. Stephenson. Double beta decay. *Progress in Particle and Nuclear Physics*, 12:409 – 479, 1984.

[69] S. Stoica and M. Mirea. New calculations for phase space factors involved in double-β decay. *Phys. Rev. C*, 88:037303, Sep 2013.

[70] K.S. Krane. *Introductory Nuclear Physics*. Wiley, 1987.

[71] K. Alfonso et al. Search for Neutrinoless Double-Beta Decay of ^{130}Te with CUORE-0. *Phys. Rev. Lett.*, 115(10):102502, 2015.

[72] A. Gando et al. Search for Majorana Neutrinos near the Inverted Mass Hierarchy Region with KamLAND-Zen. *Phys. Rev. Lett.*, 117(8):082503, 2016. [Addendum: Phys. Rev. Lett.117,no.10,109903(2016)].

[73] J. C. Pati and A. Salam. Unified lepton-hadron symmetry and a gauge theory of the basic interactions. *Phys. Rev. D*, 8:1240–1251, Aug 1973.

[74] K. S. Babu et al. Working Group Report: Baryon Number Violation. In *Proceedings, 2013 Community Summer Study on the Future of U.S. Particle Physics: Snowmass on the Mississippi (CSS2013): Minneapolis, MN, USA, July 29-August 6, 2013*, 2013.

[75] H. Georgi, H. R. Quinn, and S. Weinberg. Hierarchy of interactions in unified gauge theories. *Phys. Rev. Lett.*, 33:451–454, Aug 1974.

[76] G. Senjanovic. Proton decay and grand unification. *AIP Conf. Proc.*, 1200:131–141, 2010.

[77] J. Ellis, D.V Nanopoulos, and J. Walker. Flipping su(5) out of trouble. *Physics Letters B*, 550(1):99 – 107, 2002.

[78] Schmidt-Hoberg. Phenomenology of physics beyond the standard model. 2015.

[79] J. Hisano, H. Murayama, and T. Yanagida. Nucleon decay in the minimal supersymmetric su(5) grand unification. *Nuclear Physics B*, 402(1):46 – 84, 1993.

[80] P. Nath and P. Fileviez Perez. Proton stability in grand unified theories, in strings and in branes. *Phys. Rept.*, 441:191–317, 2007.

[81] K. S. Babu and S. Khan. Minimal nonsupersymmetric $so(10)$ model: Gauge coupling unification, proton decay, and fermion masses. *Phys. Rev. D*, 92:075018, Oct 2015.

[82] B. Bajc, I. Dorsner, and M. Nemevsek. Minimal SO(10) splits supersymmetry. *JHEP*, 11:007, 2008.

[83] L. F. Abbott and Mark B. Wise. Effective hamiltonian for nucleon decay. *Phys. Rev. D*, 22:2208–2212, Nov 1980.

[84] T. Kaluza. On the problem of unity in physics. 1982.

[85] O. Klein. Quantentheorie und fünfdimensionale relativitätstheorie. *Zeitschrift für Physik*, 37(12):895–906, Dec 1926.

[86] N. Arkani-Hamed, S. Dimopoulos, and G. R. Dvali. The Hierarchy problem and new dimensions at a millimeter. *Phys. Lett.*, B429:263–272, 1998.

[87] L. Randall and R. Sundrum. An Alternative to compactification. *Phys. Rev. Lett.*, 83:4690–4693, 1999.

[88] J. Beringer et al. Review of Particle Physics. *Phys. Rev. D*, 86:100001, 2012.

[89] R. N. Mohapatra and A. Perez-Lorenzana. Neutrino mass, proton decay and dark matter in TeV scale universal extra dimension models. *Phys. Rev.*, D67:075015, 2003.

[90] T. Appelquist, H. Cheng, and B. A. Dobrescu. Bounds on universal extra dimensions. *Phys. Rev. D*, 64:035002, Jun 2001.

[91] R. N. Mohapatra and A. Pérez-Lorenzana. Neutrino mass, proton decay, and dark matter in tev scale universal extra dimension models. *Phys. Rev. D*, 67:075015, Apr 2003.

[92] V. Takhistov. Review of Nucleon Decay Searches at Super-Kamiokande. In *Proceedings, 51st Rencontres de Moriond on Electroweak Interactions and Unified Theories: La Thuile, Italy, March 12-19, 2016*, pages 437–444, 2016.

[93] V. Takhistov et al. Search for Trilepton Nucleon Decay via $p \to e^+\nu\nu$ and $p \to \mu^+\nu\nu$ in the Super-Kamiokande Experiment. *Phys. Rev. Lett.*, 113(10):101801, 2014.

[94] H. O. Back et al. New limits on nucleon decays into invisible channels with the BOREXINO counting test facility. *Phys. Lett.*, B563:23–34, 2003.

[95] S. N. Ahmed et al. Constraints on nucleon decay via 'invisible' modes from the Sudbury Neutrino Observatory. *Phys. Rev. Lett.*, 92:102004, 2004.

[96] T. Araki et al. Search for the invisible decay of neutrons with KamLAND. *Phys. Rev. Lett.*, 96:101802, 2006.

[97] SNOLAB. www.snolab.ca, 2017.

[98] SNOLAB. Snolab user's handbook, 2006.

[99] J. B. Birks. Scintillations from organic crystals: Specific fluorescence and relative response to different radiations. *Proceedings of the Physical Society. Section A*, 64(10):874, 1951.

[100] G.F. Knoll. *Radiation Detection and Measurement*. Wiley, 2000.

[101] P. Huang, P. Li, Z. Fu, C. He, Y. Ding, J. Li, and M. Qi. Study of attenuation length of linear alkyl benzene as ls solvent. *Journal of Instrumentation*, 5(08):P08007, 2010.

[102] R. Ford and D. Horne. Note on lab auto-ignition temperature and distillation. SNO+ DocDB 5022v1.

[103] S. Andringa et al. Current Status and Future Prospects of the SNO+ Experiment. *Adv. High Energy Phys.*, 2016:6194250, 2016.

[104] J. Boger et al. The Sudbury neutrino observatory. *Nucl. Instrum. Meth.*, A449:172–207, 2000.

[105] R. Knapik. Sno+ electronics. SNO+ DocDB 733v1.

[106] A. Mastbaum. Master trigger card/analog +. SNO+ DocDB 1976v2.

[107] R. Bonventre. Xl3 programmer's manual. SNO+ Internal Document.

[108] A. Mastbaum R. Bonventre. Everything a detector operator ever wanted to know about electronics. SNO+ DocDB 1316v1.

[109] B. von Krosigk et al. Measurement of α-particle quenching in LAB based scintillator in independent small-scale experiments. *Eur. Phys. J.*, C76(3):109, 2016.

[110] J. N. Bahcall, A. M. Serenelli, and S. Basu. New solar opacities, abundances, helioseismology, and neutrino fluxes. *Astrophys. J.*, 621:L85–L88, 2005.

[111] A. C. Hayes and Petr Vogel. Reactor Neutrino Spectra. *Ann. Rev. Nucl. Part. Sci.*, 66:219–244, 2016.

[112] SNO Data Cleaning Group. Sacrifice and contamination in sno data cleaning cuts. November 2000.

[113] N. McCauley. *Producing a Background Free Data Set for Measurement of the Charge Current Flux and Day-Night Asymmetry at the Sudbury Neutrino Observatory*. PhD thesis, The Queen's College, Oxford, 2001.

[114] E. Marzec. Caen cut fec update. SNO+ DocDB 4501v2.

[115] Y. Zhang et al. First measurement of radioactive isotope production through cosmic-ray muon spallation in Super-Kamiokande IV. *Phys. Rev.*, D93(1):012004, 2016.

[116] S. Dazeley, M. Askins, M. Bergevin, A. Bernstein, N. S. Bowden, T. M. Shokair, P. Jaffke, S. D. Rountree, and M. Sweany. A search for cosmogenic production of -neutron emitting radionuclides in water. *Nucl. Instrum. Meth.*, A821:151–159, 2016.

[117] E. Marzec. The poling and ped data cleaning cut. SNO+ DocDB 4849v2.

[118] A. Li. Sno+ water phase livetime document. SNO+ DocDB 4821v2.

[119] J. Walker. *Study of Invisible Mode Nucleon Decay in the SNO+ Detector*. PhD thesis, University of Liverpool, 2016.

[120] E. Beier. Isotropy classifier. SNO+ DocDB 2835v2.

[121] J. Dunmore. *The Separation of CC and NC Events in the Sudbury Neutrino Observatory*. PhD thesis, Hertford College, Oxford, 2004.

[122] T. Pershing. Contamination study open golden data. SNO+ DocDB 4709v1.

[123] I. Murata et al. Neutron and gamma-ray source-term characterization of ambe sources in osaka university. *Progress in Nuclear Science and Technology*, 4:345–348, 2014.

[124] J. Maneira, S. Peeters, and J. Sinclair. Optical calibration of sno+. *Journal of Physics: Conference Series*, 598(1):012030, 2015.

[125] E. Leming. Ellie overview. SNO+ DocDB 4615v1.

[126] J. R. Wilson. Smellie - a scattering module in the embedded led light injection entity. SNO+ DocDB 463v2.

[127] R. Alves et al. The calibration system for the photomultiplier array of the SNO+ experiment. *JINST*, 10(03):P03002, 2015.

[128] M. Dunford. *Measurement of the 8B Solar Neutrino Energy Spectrum at the Sudbury Neutrino Observatory*. PhD thesis, University of Pennsylvania, 2006.

[129] LETA Working Group. Low energy threshold analysis (leta). SNO+ DocDB 4322v1.

[130] A. Mastbaum and F. Descamps. Run selection. SNO+ DocDB 2966v1.

[131] O. Helene. Determination of the upper limit of a peak area. *Nuclear Instruments and Methods in Physics Research Section A: Accelerators, Spectrometers, Detectors and Associated Equipment*, 300(1):132 – 136, 1991.

[132] O. Helene. Upper limit of peak area. *Nuclear Instruments and Methods in Physics Research*, 212(1):319 – 322, 1983.

[133] J. Neyman. Outline of a theory of statistical estimation based on the classical theory of probability. *Philosophical Transactions of the Royal Society of London. Series A, Mathematical and Physical Sciences*, 236(767):333–380, 1937.

[134] G. J. Feldman and R. D. Cousins. A Unified approach to the classical statistical analysis of small signals. *Phys. Rev.*, D57:3873–3889, 1998.

[135] G. Bohm and G. Zech. *Introduction to Statistics and Data Analysis for Physicists*. Verlag Deutsches Elektronen-Synchrotron, 2010.

[136] G. Cowan. *Statistical data analysis*. Oxford University Press, USA, 1998.

[137] J. Neyman and E. S. Pearson. On the Problem of the Most Efficient Tests of Statistical Hypotheses. *Philosophical Transactions of the Royal Society of London Series A*, 231:289–337, 1933.

[138] J. S. Conway. Incorporating Nuisance Parameters in Likelihoods for Multisource Spectra. In *Proceedings, PHYSTAT 2011 Workshop on Statistical Issues Related to Discovery Claims in Search Experiments and Unfolding, CERN,Geneva, Switzerland 17-20 January 2011*, pages 115–120, 2011.

[139] X. Ye et al. Preliminary study of light yield dependence on LAB liquid scintillator composition. *Chin. Phys.*, C39(9):096003, 2015.

[140] LLC. Koch Modular Process Systems. https://kochmodular.com/, 2017.

[141] J. Benziger, L. Cadonati, F. Calaprice, M. Chen, A. Corsi, F. Dalnoki-Veress, R. Fernholz, R. Ford, C. Galbiati, A. Goretti, E. Harding, Aldo Ianni, Andrea Ianni, S. Kidner, M. Leung, F. Loeser, K. McCarty, D. McKinsey, A. Nelson, A. Pocar, C. Salvo, D. Schimizzi, T. Shutt, and A. Sonnenschein. A scintillator purification system for the borexino solar neutrino detector. *Nuclear Instruments and Methods in Physics Research Section A: Accelerators, Spectrometers, Detectors and Associated Equipment*, 587(2):277 – 291, 2008.

[142] R. J. Ford. A Scintillator Purification Plant and Fluid Handling System for SNO+. *AIP Conf. Proc.*, 1672:080003, 2015.

[143] Emerson. https://www.emerson.com/en-us/automation/deltav, 2017.

[144] D. Hemer and K. DeLong. UC Davis machine shop.